OCEAN SOUND FIELD CHARACTERIZATION USING PROCESSING TECHNIQUES BASED ON NOISE SPATIAL COHERENCE

by

Najeem Shajahan

Submitted in partial fulfillment of the requirements
for the degree of Doctor of Philosophy

at

Dalhousie University
Halifax, Nova Scotia
April 2022

DEDICATION

To my mother Naseema Beevi

CONTENTS

LIST OF TABLES

LIST OF FIGURES

ABSTRACT

The spatial coherence of ambient noise can be used for noise-based inversion studies using appropriate coherence models. Additionally, the spatial and temporal properties of ocean ambient noise are important factors to consider in the design of passive and active acoustic systems. The main findings of this thesis are presented in four chapters. In chapter 2, using a two-component noise coherence model (wind and shipping), an inversion scheme is developed to determine the relative and absolute contribution of frequency-dependent ship noise to the total sound field and demonstrated on a 29 day long ambient noise data set. A simple model of vertical coherence for a broadband acoustic source is developed in chapter 3 to understand the characteristics of the sound field produced by ships at close ranges. The measured coherence of a moving vessel near a submarine canyon is compared with simulated results to obtain the range of the vessel. A case-study where the bearing and range of the ship are obtained by exploiting the asymmetry of the regional bathymetry is shown. In the fourth chapter, a map of vertical noise coherence is generated to study the environmental dependence of vertical coherence at the mesoscale. These maps can be used to design the ideal spacing of multi-element vertical hydrophone arrays in the continental shelf and slope regions for signal detection optimization. Finally, in chapter 5, a three-component (wind, close-range shipping, and distant wind and shipping) depth-dependent noise coherence model is developed to identify and partition the noise field in deep water. Noise coherence profiles measured in Challenger Deep, located at the southern end of the Mariana Trench, were used to validate the applicability of the developed theory and identify two deep water noise scenarios. The methods introduced in this thesis encourage the use of vertical pairs of hydrophones in acoustic monitoring of the ocean for soundscape studies and remote sensing.

LIST OF ABBREVIATIONS USED

Abbreviation	Description
2-D	Two-Dimensional
3-D	Three-Dimensional
AG	Array Gain
AIS	Automatic Identification System
CPA	Closest Point of Approach
CSD	Cross Spectral Density
CTD	Conductivity-Temperature-Depth
DAL	Deep Acoustic Lander
dB	decibel
NG	Noise Gain
PAM	Passive Acoustic Monitoring
PE	Parabolic Equation
PSD	Power Spectral Density
RV	Research Vessel
SEL	Sound Exposure Level
SHRU	Several Hydrophone Receiving Unit
SNR	Signal to Noise Ratio
SONAR	Sound Navigation and Ranging
SOFAR	Sound Fixing and Ranging
SPL	Sound Pressure Level
TL	Transmission Loss
TOSST	Transatlantic Ocean System Science and Technology
VLA	Vertical Line Array
WHOI	Woods Hole Oceanographic Institute

ACKNOWLEDGEMENTS

I am thankful to many individuals for helping me finish this research work.

To start with, I am very grateful to my supervisor, David Barclay, for his encouragement, scientific insights, generous financial support, friendship and clarifying my endless doubts. Many thanks to the members of my thesis advisory committee, Eric Oliver, Mike Dowd and Chris Algar for their feedback and suggestions to improve the quality of this thesis. I would like to thank Ying-Tsing Lin, my WHOI collaborator, for his advice and for sharing the data used in this thesis. Thanks to Lori Lawton, Daniel Morrison, Jackie Hurst and Kirsten Laing for their professional support.

I would also like to thank the present and past members of the Noise Lab at Dalhousie for discussions, questions, knowledge sharing and time. I want to thank my football and softball playmates at Dalhousie for sharing some most memorable moments and helping to reduce the stress during these past years. I also want to acknowledge TOSST for my graduate fellowship. I sincerely thank Jenna Hare and Emmanuelle Cook for a careful proofreading and a review of the thesis.

I wish to express special thanks to my parents and siblings for their unconditional love and blessing. Finally, I would like to thank my wife Ameena for her boundless love and encouragement. Without her understanding and support, I couldn't have finished this work successfully.

CHAPTER 1

INTRODUCTION

1.1 Ambient Noise in the Ocean

Ambient noise is normally considered as an interference in signal detection for underwater acoustic applications such as transmission loss (TL) experiments, underwater communications, marine mammal monitoring, and passive and active sonar signal processing. Sources of ambient noise in the ocean can be broadly classified as natural or anthropogenic. Wind-induced breaking waves, rain, and biological sources are common sources of natural ambient noise. Ship traffic, active sonar operations, and offshore construction and exploration are prominent sources of anthropogenic noise in the ocean. Among these sources, wind-generated noise and distant shipping noise are omnipresent and the primary contributors to ambient noise in the ocean (Wenz, 1962). The sound produced by these sources is location specific and exhibits both spatial and temporal variations depending on the source strengths and propagation conditions.

The characteristics of ambient noise measured in shallow and deep water are different. Normally, shallow water ambient noise exceeds the noise level in deep water due to the proximity of the seabed and relatively constrained geometry of the environment. In shallow water, the characteristics of ambient noise generated by surface-distributed sources depend on the bathymetry, water column sound speed depth-profile, and sediment geo-acoustic properties. In deep water, both locally generated wind-wave and distantly-generated ship and wind-wave noise propagating through the SOund Fixing and Ranging (SOFAR) channel are the primary influences on the noise field with the effects of sediment type being relatively less. Thus, the prediction of

the noise field spatial properties requires knowledge about the properties of the propagation environment, the type of noise sources, and their spatial and temporal distributions.

Second-order statistics (power spectrum and cross-spectrum) are generally used to characterize ambient noise in the ocean due to the random nature of the signals generated at the ocean surface. The most used metric for noise field characterization is the power or pressure spectral density, which gives the frequency content of the received signal. The cross-correlation or cross-spectrum of ambient noise is determined by analyzing the space-time correlation properties of noise received by a pair of hydrophones and these metrics provide the similarity of signals in the time and frequency domain, respectively, and they are related through an inverse Fourier Transform. Moreover, the cross-spectrum also provides information about the direction of arrival and spatial extent of the acoustic source.

In the ocean, the normalized cross-spectrum or coherence of ambient noise due to surface-generated sources (e.g. wind-generated waves) is a stable quantity, independent of source level and depends only on the properties of the acoustic environment such as the sound speed profile and seabed sediment properties. However, in the presence of a second source (e.g. a passing vessel), the coherence may vary depending on the source spectrum and position of the other source (Deane *et al.*, 1997; Shajahan *et al.*, 2020). The earliest model of noise spatial coherence was developed by Cron and Sherman (1962) and comprised of a near-surface sheet of sources in a semi-infinite, homogenous, and azimuthally uniform ocean, predicting the properties of a strictly downward propagating wind-wave generated noise field. An isotropic noise model was also proposed, where it was assumed that the noise field had equal intensity at all arrival angles, or a uniform directionality. Even though the Cron-Sherman model neglected reflection from the

seabed, the simulation results agreed well with deep water field measurements (Barclay and Buckingham, 2013a; Barclay and Buckingham, 2013b).

A similarly formulated model of surface generated noise correlations in shallow water was developed by Kuperman and Ingenito (1980), and included the source characteristics, water column sound speed, and seabed sediment acoustic properties. The modelled field relies on the deriviation of normal modes in the waveguide. Buckingham (1980) derived a closed form expression for spatial correlation in shallow water assuming uniform sound speed and low loss in the seabed. Another analytical solution for ambient noise vertical coherence based on ray theory was developed by Harrison (1996) for a range independent environment, which was later extended for a range-dependent environment with a non-uniform source distribution (Harrison, 1997).

Carey (1990) estimated the noise spatial coherence for a vertical array in a range-dependent ocean using a Parabolic Equation (PE) model with randomly distributed surface noise sources. As opposed to the previously described models that predict the expectation value of the second-order statistics of the noise field, the output of the fully computational PE model provides a noise snapshot. Such snapshots are useful for simulating the performance of coherent processing algorithms, such as matched field processing. On the other hand, predictions of expectation values are straight-forward to compare with ensemble averaged values from real measurements and have been widely used as a tool for determining ocean environmental parameters using passive acoustics (Carbone *et al*, 1998; Barclay *et al*, 2019).

Ambient noise data contains information about the environment since the sound interacts with the ocean boundaries and the water column before reaching the hydrophones. The spectral characteristics of long-term ambient noise data from a single hydrophone can be used to determine the wind speed and rainfall rate (Vagle *et al.*, 1990; Nystuen *et al.*, 1993). Buckingham (1987)

developed a technique to estimate the compressional sound speed of sediment using ambient noise spatial coherence. Noise can also provide information on the geoacoustic properties of a layered seabed in shallow water (Carbone *et al.*, 1998). The technique developed by Harrison and Simons (2002) used noise measured on a vertical hydrophone array to obtain the sub-bottom profile. Extraction of time-domain Green's function using cross-correlation of ambient noise is a major finding in noise-based inversions with many applications, including passive time-reversal (Sabra *et al.*, 2005). Temperature and current speed can be inverted using noise measured on horizontally separated sensors (Godin *et al.*, 2014; Woolfe *et al.*, 2015). Passive fathometer processing is a technique developed to get the water column depth and sub-bottom profile by extracting the Green's function from a vertical array (Siderius *et al.*, 2006). Recently, matched field processing techniques have been developed to obtain seabed reflection loss from ambient noise data (Muzi *et al.*, 2018). All these applications use either the direct measurement of noise coherence or matched field processing techniques to study the ocean environment.

Apart from environmental information extraction and sonar performance analysis, ambient noise data have been widely used to monitor marine animals and determine their acoustic habitat. In addition, identifying the human-generated sound sources and quantifying the impact of these sources on the acoustic habitat is currently a major area of study and application of passive acoustic monitoring (PAM). Anthropogenic noise, especially ship traffic in the ocean, causes the risk of masking, distraction, change in behaviour, physiological stress, and injury to aquatic animals (Merchant *et al*, 2014).

The ambient soundscape is the combination of all sources present in the environment, and the existence of multiple sources complicates the interpretation of soundscape using sound pressure level (SPL) or power spectral density (PSD). Extraction, detection, and classification of

sound sources present in the environment is possible using advanced processing methods such as Machine Learning (ML) and Empirical Mode Decomposition (EMD) (Bermant *et al*, 2019; Caruso *et al*, 2020; Seger *et al*, 2018). ML techniques use self-learning algorithms to identify sources from acoustic measurement, but the main limitation is the requirement of an excessive amount of training datasets (Bianco *et al*, 2019). EMD clearly identifies the sound sources present in the environment by decomposing the time series into a set of modal functions (Seger *et al*, 2018). However, the method is sensitive to ambient noise conditions and the performance of EMD degrades when the signal contains extreme amplitude such as close-range shipping. Because of the dynamic nature of the ocean environment and the widely varying structure of ship noise source signatures, the use of PSD is not adequate for precisely quantifying the anthropogenic contribution to the noise field above the natural background noise (Gibb *et al*, 2019). Incorporating source identification and source features is important in comparing the soundscapes of various locations. Thus, it is essential to use multiple sensors and develop new physics-based processing methods for soundscape interpretation and source identification which can help to frame mitigation strategies.

Other than soundscape studies, PAM systems can also be used for the detection and tracking of marine mammals and ships. Most of the PAM systems use single acoustic recorders to identify vessel activity and the presence of aquatic animals (Kline *et al*, 2020; Sanguineti *et al*, 2021). The limiting challenges for source localization with a single sensor are multipath interference and low signal-to-noise ratio (SNR). Growing computational power and enhanced storage capacity facilitates the use of multiple sensors and advanced processing tools for target classification and localization. Coherence-based detection and tracking is convenient and reliable since it enhances the signal and reduces the background noise. This can help in the sustainable

management of the marine environment by implementing real-time detection of vessels and marine mammals.

Vertical coherence of ambient noise and its horizontal variation play a crucial role in the design and positioning of hydrophone arrays in acoustic experiments due to its relationship with the array gain (Urick, 1967). In most of the studies, hydrophone arrays are designed to reduce the spatial coherence of ambient noise by keeping the elements at half-wavelength spacing based on the isotropic noise model (Yang *et al*, 2018). However, the propagation condition of the measurement location influences the noise coherence function and the array performance. Moreover, accurate fine-scale spatial measurements (resolution 10's of km2) of noise coherence over a large area are difficult to obtain due to high experimental cost motivating a need for predictive models of noise coherence. Modelling the spatial properties of noise, both the spatial variability and spatial correlations, is a useful prerequisite for the successful execution of active and passive acoustic experiments and operations. Predictions of noise correlation may be used to inform sonar array design (e.g. receive element spacing and operating frequency) while knowledge of spatial variability may be used to optimally choose the array location.

Long-range acoustic propagation experiments use multi-element hydrophone arrays to better understand the basic physics of low-frequency, broadband sound transmission (Munk *et al*, 1995; Worcester *et al*, 1999; Colosi *et al*, 1999). The main limitation of these experiments is the signal processing difficulty caused by mesoscale ocean processes and background ambient noise. The types of noise sources, spatial distribution, and environmental characteristics are important factors in signal processing at long ranges. A prerequisite for such experiments is a model of spatial coherence which can incorporate the source types, propagation conditions and frequency dependence of background noise. The main drawback of available models of deep-water noise

coherence is the exclusion of sound sources other than surface agitation and sound refraction due to the environment (Buckingham, 2012; Buckingham, 2013). Thus, the development of a spatial coherence model for deep water which can distinguish major sound sources and their spatiotemporal variation is crucial. The model can be used in the signal processing of multi-element receivers to improve the efficiency of acoustic tomography.

The above limitations in ocean acoustics can be addressed by using coherence as a metric in the acoustic data processing. Coherence can serve as a tool in source localization, environmental inversion, hydrophone array design, long-range acoustic propagation, and source identification and classification. Coherence-based analysis, discussed in this thesis, is capable of separating source components and identifying the variation of each source with respect to space, time, and frequency, providing a new tool for PAM analysis with relevance to bioacoustics and acoustic ecology. Another advantage of noise-based inversion techniques is that they only exploit the existing sound in the ocean, without introducing additional sound which may harm marine mammals and soniferous fishes. Hydrophone pairs can be easily attached to moorings, drifting buoys, and profiling floats for large scale ocean monitoring. The scope of two sensor measurements in ocean monitoring opens new practices for passive acoustic data analysis.

The overall objective of this thesis is to develop coherence-based processing techniques for partitioning the noise field using the relationship between noise directionality and vertical coherence. The partitioned field can then be analyzed to better quantify the impact of individual contributors to the noise field and to improve models of physical processes contributing to underwater noise. These models may further be used to estimate ocean and seabed properties. Thus, noise coherence also provides an effective tool for monitoring oceanographic and geoacoustic properties. The relationship between vertical coherence and the noise field

directionality as well as simple analytical models of vertical noise coherence are described in the next section.

1.2 Vertical Coherence and Directionality

Let $x(t)$ be the time series of acoustic data measured using a hydrophone. The frequency content is then given by the Fourier Transform,

$$X(\omega) = \int_{-\infty}^{\infty} x(t) e^{i\omega t} dt, \tag{1.1}$$

where $X(\omega)$ is the Fourier Transform of $x(t)$, ω is the angular frequency, and $i = \sqrt{-1}$. The PSD of the time series is computed as

$$\langle S(\omega) \rangle = \frac{|\langle X(\omega) \rangle|^2}{T}, \tag{1.2}$$

where the angle brackets $\langle\ \rangle$ indicate an ensemble average and T is the observation duration. In the case of two separated sensors, the time series of received noise can be represented as $x_1(t)$ and $x_2(t)$, respectively. Applying Eq. (1.1), the cross spectral density can then be calculated as

$$\langle S_{12}(\omega) \rangle = \frac{\langle X_1(\omega) \cdot X_2^*(\omega) \rangle}{T}, \tag{1.3}$$

where $X_1(\omega)$ and $X_2(\omega)$ are the Fourier transforms of time series received at the two sensors, and * denotes the complex conjugate. The cross spectrum is a complex quantity where the real part and imaginary part are the co-spectrum and quadrature spectrum, respectively. The real part represents the in-phase signal and imaginary part is the out-of-phase signal. Using Eqs. (1.1) and (1.3), the spatial coherence of noise fluctuations received at two sensors is determined by normalizing the cross spectral density (CSD) with the individual PSD of each sensor and is given by

$$\Gamma_{12}(\omega) = \frac{\langle S_{12} \rangle}{\sqrt{\langle S_{11} \rangle \cdot \langle S_{22} \rangle}}. \tag{1.4}$$

The spatial coherence provides the similarity of signals received at two sensors in the frequency domain. In a plane wave noise field, the PSD is independent of its measurement position in the water column (Buckingham, 1980). Under this assumption of a spatially homogeneous environment, Cox (1973) derived an expression for coherence in terms of the vertical directionality of noise field

$$\Gamma_{12}(\omega) = \frac{1}{2}\int_0^{\pi} F(\theta)\, e^{-i\omega\tau_d \cos\theta} \sin\theta \, d\theta, \tag{1.5}$$

under the normalization condition

$$\frac{1}{2}\int_0^{\pi} F(\theta) \sin\theta \, d\theta = 1, \tag{1.6}$$

where $F(\theta)$ is the two-dimensional (vertical) directional density function of the total noise field, θ is the polar angle measured from the zenith, and $\tau_d = \frac{d}{c}$, is the time delay where d is the spacing between the vertically-separated sensors and c is the local sound speed. The linear relationship between vertical coherence and directionality is evident in Eq. (1.5). The right-hand side of Eq. (1.5) can be expanded into real and imaginary components using Euler's identity, corresponding to the real and imaginary parts of the noise coherence. Since the noise directionality is necessarily real, the real part of coherence is then an even function about the horizontal ($\theta = \frac{\pi}{2}$), which indicates a symmetry of the noise directionality about the horizontal. In contrast, the imaginary component is an odd function about the horizontal and describes the asymmetric component of the noise directionality.

With the aid of Cox's equation (Eq. (1.5)), simple analytical models of noise spatial coherence can be derived. First, consider the simple case of a plane wave striking two vertically-oriented sensors separated by a distance d along the z-axis (Jensen *et al.*, 2011). The impinging sound at these two sensors can be represented as

$$n_z = Ae^{ikz} \text{ and } n_{z+d} = Ae^{ik(z+d)}, \tag{1.7}$$

where A is the amplitude and $k = 2\pi/\lambda$ is the wavenumber, and λ is the wavelength. The normalized cross spectrum of the sound wave is

$$\Gamma_{12}(d) = \frac{\langle n_z n_{z+d}^* \rangle}{\sqrt{|n_z|^2 |n_{z+d}|^2}} = e^{-ikd\cos\theta} . \tag{1.8}$$

If the noise is coming from the horizontal direction ($\theta = \pi/2$), the spatial correlation is 1 for all values of d. If the noise is directly coming from above ($\theta = 0$), the real coherence is a cosine curve with the first zero-crossing located at $d = \lambda/4$. As θ increases from zero, the first zero-crossing appears at values of d$= \lambda/(4 + l)$, where $0 < l < \lambda - 4$. Thus, a positive value for coherence for a vertically oriented sensor can be interpreted as signal coming from horizontal or near-horizontal direction.

In the case of an isotropic noise model, the noise field is assumed to be made up of a superposition of plane waves distributed uniformly over all directions. The spatial correlation for such a noise field is determined by computing the coherence for a single plane wave between two points and then averaging over the polar, θ, and azimuthal angles, φ, respectively

$$\Gamma_{12}(d) = \int_0^{2\pi} d\varphi \int_0^{\pi} e^{-ikd\cos\theta} \sin\theta \, d\theta,$$

$$\Gamma_{12}(d) = \frac{\sin kd}{kd} . \tag{1.9}$$

Since the noise field directionality is symmetric about the horizontal for the isotropic model, only the real part of coherence exists, and the imaginary component is zero. This simplified model is often the basis for sensor spacing selection in array design. Eq. 1.9 has a zero-crossing at $d = \lambda/2$, implying that the noise correlation between sensors is zero at the design frequency corresponding to an element spacing of a half-wavelength. Such an element spacing allows noise gain to be minimized across the array under this specific noise condition.

A more realistic model of spatial coherence is the surface noise model of Cron and Sherman (1962) where the noise sources are uniformly distributed in a horizontal plane immediately below the ocean surface. The ocean is assumed to be a semi-infinite homogeneous half-space with a pressure release boundary. Azimuthal uniformity of the noise field with only downward propagating noise is considered. Each noise source at the surface has a corresponding image source placed across the boundary, and the pair act as a dipole. Integrating over all ranges, the directional density function for such a noise field can be given as (Buckingham, 2011)

$$F(\theta) = 4\cos\theta \qquad 0 \le \theta \le \pi/2 \tag{1.10}$$
$$= 0 \qquad\qquad \pi/2 \le \theta \le \pi$$

The vertical coherence in terms of wavenumber can be derived by substituting Eq. (1.10) into Eq. (1.5), giving

$$\Gamma_{12}(\omega) = 2\int_0^{\pi/2} e^{-ikd\cos\theta}\cos\theta\sin\theta\, d\theta$$
$$= 2\left[\frac{\sin kd}{kd} + \frac{\cos kd - 1}{(kd)^2}\right] + 2i\left[\frac{\cos kd}{kd} - \frac{\sin kd}{(kd)^2}\right]. \tag{1.11}$$

This function is the Cron-Sherman formula for ambient noise coherence in deep water. Eq. (1.9) is a real valued function and Eq. (1.11) is a complex function. Since the noise field has only a downward traveling component, the noise directionality is anisotropic, and the result is a complex coherence function. Thus, the anisotropic nature of noise field can be studied using ambient noise coherence measurements.

1.3 Research Objectives and Thesis Outline

The purpose of this thesis is to combine signal processing and noise modelling methods to better understand the composition, time variability, and spatial structure of the ocean noise field. Ambient noise measurements and appropriate noise coherence models are used for the

implementation of each method. The objective, approach and application of each technique developed in this thesis are listed below.

1. Quantify the contribution of ship noise to the underwater noise field.

A two-component noise model of vertical coherence consisting of wind-driven wave noise and distant or close ship noise is developed for a shallow water environment (Chap. 2). An inversion scheme is established to determine the relative and absolute contribution of frequency-dependent ship noise to the total noise field and applied to a month-long dataset collected on the New England shelf. This processing technique has the advantage of quantifying the impact of anthropogenic noise in the ocean without prior knowledge of environmental information such as wind speed and ship distribution.

2. Determine the range and bearing of a broadband acoustic source using vertical coherence.

In Chap. 3, a simple model of vertical coherence for a broadband acoustic source is developed. This model can be used to understand the characteristics of the sound field produced by ships at close range (< 10 km). The measured coherence of a moving vessel near a submarine canyon is compared to simulated results to obtain the range of the ship while the bearing of the ship can be determined using a 3-D sound propagation model by exploiting the canyon bathymetry. Coherence-based range estimation shows high reliability because of its wideband nature and insensitivity to signal-to-noise ratio (SNR) effects.

3. Noise coherence mapping

A map of wind-generated noise coherence is developed to study the environmental dependence of coherence over large (mesoscale) areas. A PE sound propagation model based on reciprocity theory is used for the simulation of noise field and spatial coherence (Barclay and Lin., 2019). Sound speed profile, sediment type and spatial variation in the bathymetry are the

environmental parameters used for the simulation of the noise coherence map. The results of this analysis can be used as a reference in planning TL, sonar, PAM and other passive acoustic experiments in regions with insufficient environmental information available for array design.

4. Depth-dependent noise coherence model for deep water.

In Chap. 5, a three-component noise coherence model comprised of locally generated wind-wave noise, close-range vessels, and combined distant wind and shipping as the major sources is developed. The model is used as the basis for an inversion tool on two noise coherence profiles from the Challenger Deep, Mariana Trench. This method is used to partition and extract the depth-dependent contribution of natural and anthropogenic sources as well as local and SOFAR channel propagating sources in deep water.

The rest of this thesis is organized as follows:

Chapter 2 presents the theory, numerical results, and experimental validation of the noise partitioning technique. The source localization method using vertical coherence is described in chapter 3. The analysis to study the spatial variation in noise coherence is presented in chapter 4. The theory and experimental verification of the three-component noise coherence model for deep water applications are shown in chapter 5. Finally, a summary of the thesis, major contributions and future work prospects are discussed in chapter 6.

Four manuscripts are prepared based on the research results of this thesis. Chapter 2 was published in the *Journal of Acoustical Society of America* under the title “Quantifying the contribution of ship noise to the underwater sound field” (Shajahan et al, 2020).

CHAPTER 2

QUANTIFYING THE CONTRIBUTION OF SHIP NOISE TO THE UNDERWATER NOISE FIELD

2.1 Introduction

The noise of surface distributed sources such as breaking waves and rainfall is ubiquitous in the world's oceans and noise generated by ships is detectable in nearly every ocean basin (Wenz, 1962). The increase in commercial ship traffic is responsible for an increase of low frequency (0.1-1 kHz) noise by about 3 dB/decade since 1960 due to the global economic growth, with a flattening in recent years (McDonald *et al.*, 2006; Chapman and Price, 2011; Frisk, 2012; Miksis-Olds and Nichols, 2016; Harris *et al.*, 2019). Noise produced by vessel traffic dominates the typical deep ocean spectrum below 1 kHz, while above that value the noise of wind-generated breaking waves prevails. The resultant ambient noise field at low frequencies depends on ship traffic density and ship source spectrum level and can be as much as 40 dB higher than the typical wind noise levels in the same band (Wales and Heitmeyer, 2002). Increases in anthropogenic noise due to shipping can mask the effective communication range, alter habitat use, impact behavior, and increase stress among marine species and are a growing concern for researchers working in marine ecology (e.g. Rolland *et al.*, 2012; Popper and Hawkins, 2016; Putland *et al.*, 2018). As a result, Passive Acoustic Monitoring (PAM) has become widely used in ocean monitoring and long-term ambient sound recordings have been used with Automatic Identification System (AIS) data and sound propagation models to study and map the impact of ship traffic on the marine habitat (Erbe *et al.*, 2012; Merchant *et al.*, 2012; Gervaise *et al.*, 2015; Aulanier *et al.*, 2017). These approaches use metrics derived from power or pressure spectral density to study the

marine soundscape and the potential impacts of anthropogenic noise sources on the overall noise field and marine animals. However, because of the dynamic nature of natural ambient noise driven by wind speed and direction, sea-surface roughness, bathymetry, fetch (Vagle *et al.*, 1990), surface current speed and direction, and rainfall (Nystuen *et al.*, 1993), quantifying the contribution of anthropogenic sources above the changing background level is challenging. In this Chapter, a method of source separation based on the linear relationship of the directionality and vertical coherence of surface-generated and distant and close-range vessel-generated noise is used to quantify the time series of the relative and absolute contribution of shipping activity to the undersea soundscape in a month-long data set.

In shallow water, the spatial properties of the ambient noise generated by surface distributed sources, including the directionality, depend on the bathymetry, water column sound speed, and sediment geo-acoustic properties. In the case of the seabed with a sound speed faster than that in the water, the critical angle can be measured and used to estimate the value of the compressional sound speed in the sediment (Buckingham and Jones, 1987). The normalized cross-spectral density, or the vertical noise coherence is directly related to the directionality (Cox, 1973) and can be used to infer the geoacoustic properties in a Pekeris (fluid) wave guide (Deane *et al.*, 1997), a shallow water elastic wave-guide (Carbone *et al.*, 1998), and a multilayered seabed (Barclay *et al.*, 2019). Direct measurements of noise directionality, coherence, and cross-correlation using beamformed vertical line arrays and model-based matched field processing techniques have been used to invert high-resolution bottom reflection loss coefficients (Siderius *et al.*, 2013; Muzi *et al.*, 2015; Muzi *et al.*, 2016; Muzi *et al.*, 2018) and to passively detect the sea-floor depth and sub-bottom layering (Siderius *et al.*, 2006). It has been shown that the water

column sound speed profile and attenuation in the deep ocean can be inverted using the vertical coherence of ambient noise (Barclay and Buckingham, 2013a; Buckingham, 2013).

The noise coherence is a normalized quantity, independent of the time-varying frequency-dependent power spectral density typically observed in ocean noise. It is insensitive to source strength and the slope and spectral shape of the background noise which can vary from site to site in shallow water (Ingenito and Wolf, 1989). In inversion applications, the stability and wideband nature of the vertical noise coherence function allows estimates of seabed bottom loss and sub-bottom structure (Siderius *et al.*, 2006).

In general, the vertical directional density function changes depending on the distribution of sources and their relative dominance. When surface noise sources are non-uniform, for instance during a finite-size rain storm, the noise coherence will reflect the location and size of the storm, and rate of the rainfall (Barclay and Buckingham, 2013b). For an individual source, such as a ship, conventional propagation modelling methods can be used to predict the phase interference, or cross-spectral density, across an array. Broadband matched field processing on a vertical line array has been proven an effective technique for source ranging with many applications (Baggeroer *et al.*, 1988; Brienzo and Hodgkiss, 1993). Though the majority of matched field processing studies rely on coherent processing across large aperture arrays, these modelling techniques are also well suited for predicting the coherence of ship noise on a two-element vertical array. In the case of distantly generated ship noise, which may originate from a number of vessels, the addition of the first few normal modes to the noise field has been shown as an accurate model of the vertical coherence in a shallow water waveguide (Deane *et al.*, 1997). In this chapter, by treating the pressure time series on a pair of vertical receivers as a linear combination of two processes, wind-driven wave noise and distant or close ship noise, the relative and absolute contribution of each

field to the overall noise field are computed. This is particularly useful in the context of PAM, where metrics include the sound pressure level (SPL) and sound exposure level (SEL) computed over various time intervals and frequency bands (Martin *et al.*, 2019). By first carrying out the source separation described here, then computing these metrics, the contribution of ship noise to SPL and SEL, in absence of any contribution from the natural background noise, may be uniquely determined and exactly quantified.

The rest of the chapter is organized as follows: Section 2.2 describes measurement details and auxiliary data used for the analysis. Section 2.3 shows the linear relationship of vertical coherence and directionality and describes the method to determine the relative and absolute contributions of separate sources to the total field. Vertical noise coherence models of wind-driven ambient noise and ship generated noise are presented in Section 2.3. In Section 2.4, the experimental results are described and the implementation of the analysis technique using the coherence models is shown. Section 2.5 discusses the application of coherence-based ambient noise data analysis for quantifying the contribution of anthropogenic noise.

2.2 Data Collection

The acoustic data used in this analysis were collected on a vertical array deployed near the head of Alvin Canyon, located south of Martha's Vineyard, Massachusetts, as part of a sound propagation and ambient sound monitoring experiment. The array was deployed from the R/V Neil Armstrong on the final leg of the scientific verification cruise from Fairfax, Virginia to its home port, Woods Hole, Massachusetts. The location of the measurement site was at 39° 58.32' N, 70° 32.94' W, and is shown in Figure 2.1. The water column depth at the mooring location is 350 m. 29 days of continuous sound pressure time series data were recorded from April 6th to May 4th, 2016 using Woods Hole Oceanographic Institute's (WHOI) Several Hydrophone Receiving Unit

(SHRU) configured as a Vertical Line Array (VLA) on a sub-surface mooring. The SHRU VLA consisted of four hydrophones with the top-most sensor (channel 0) positioned at 211.05 m below the surface, and the remaining sensors at depths of 219.03 m (channel 1), 219.87 m (channel 2), and 220.55 m (channel 3). The hydrophones used in this study were channels 1 and 3, corresponding to an interelement spacing of 1.52 m. All four channels were simultaneously sampled at 9765.625 Hz and subjected to a high-pass filter giving an acoustic bandwidth from 10 - 4880 Hz. The receive sensitivity of the omnidirectional hydrophones was reported by the manufacturer as -170dB re 1 $V/\mu Pa$.

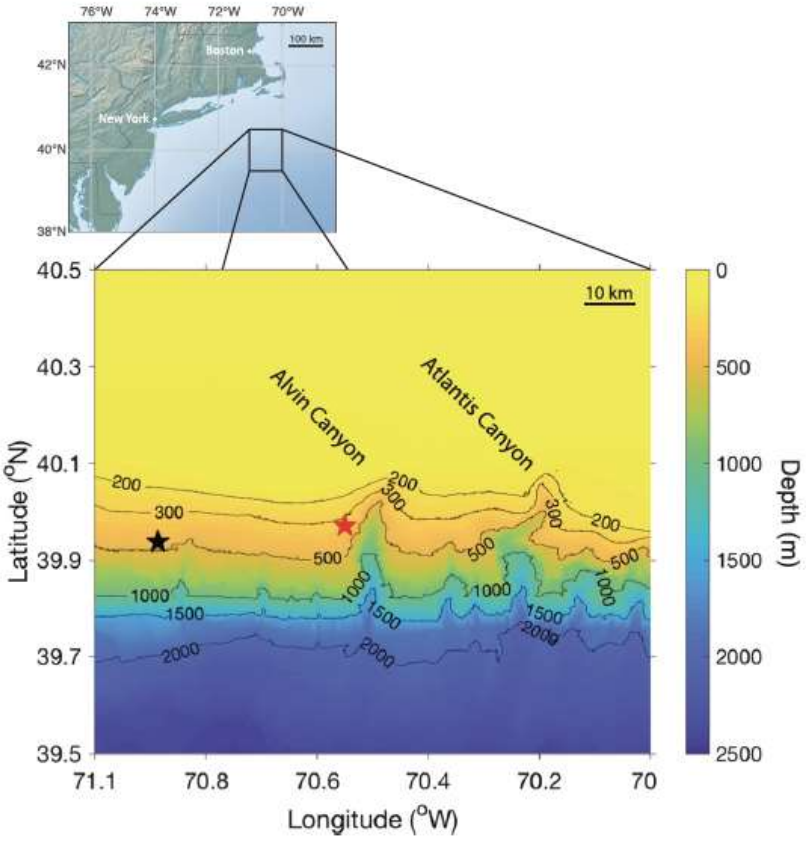

Figure 2.1: The location of the ambient noise measurement site near Alvin Canyon (red star) and the offshore surface mooring of Pioneer Array Network (black star).

Temperature and pressure sensors were attached along the mooring and recorded the water column temperature and mooring tilt and sampled every 30 seconds. Wind speed data were collected from the Central Surface Mooring (CP01CNSM), part of WHOI's coastal observatory network known as the Ocean Observatories Initiative Pioneer Array. The surface mooring, carrying a full meteorology sensor package, provides wind speed adjusted to a height of 10 m above the sea-surface and is located approximately 30 km from the acoustic receiver, at 39° 56.22' N, 70° 52.62 W, shown in Figure 1. The data were accessed via the Ocean Observatories Initiative data portal (NSF Ocean Observatories Initiative Data Portal). Geoacoustic seabed properties at the experiment site were determined using US Geological Survey data which reported a compressional sound speed of 1620 m/s (Reid *et al.*, 2005).

2.3 Theory

2.3.1 Vertical Coherence and Directional Density Function

The underwater ambient sound field may be comprised of a linear superposition of two or more noise generating processes provided they are uncorrelated. In the case presented here, noise produced by wind-generated waves breaking at the ocean's surface and noise due to one or more vessels are considered as the primary contributions to the ambient noise field measured on two vertically-separated receivers. The acoustic pressure time series at the two vertically-separated receivers are given by

$$x_1(t) = w_1(t) + v_1(t) \tag{2.1}$$

and

$$x_2(t) = w_2(t) + v_2(t), \tag{2.2}$$

where $w_i(t)$ is due to breaking surface waves and $v_i(t)$ is due to vessels on the i-th hydrophone. The two terms on the right-hand side in each equation are uncorrelated, while both $w_i(t)$ and $v_i(t)$

have some spatial correlation across the two hydrophones. The cross-spectral density between two sensors, S_{ij} is given by

$$\langle S_{ij}(\omega)\rangle = \frac{\langle X_i \cdot X_j^*\rangle}{T}, \tag{2.3}$$

where X_i is the Fourier transform of x_i, ω is the angular frequency, * denotes the complex conjugate, the angle brackets $\langle\ \rangle$ indicate an ensemble average, and T is the observation duration. When $i=j$, Eq. (2.3) describes the power spectral density. Combining Equations (2.1) – (2.3) and noting that the ensemble averages of uncorrelated terms go to zero, the cross-spectral density becomes

$$\langle S_{ij}(\omega)\rangle = \frac{\langle W_i \cdot W_j^*\rangle + \langle V_i \cdot V_j^*\rangle}{T}, \tag{2.4}$$

where W_i and V_i are the Fourier transforms of w_i and v_i respectively and their dependence on the angular frequency, ω, is implied.

Assuming that both the wave and vessel generated fields are spatially homogenous away from the ocean boundaries and for small receiver separations (Buckingham, 1980), the power spectral density of the total received signal, as well as its components, are independent of receiver position, thus

$$\langle S_{11}\rangle = \langle S_{22}\rangle, \tag{2.5}$$

$$\langle W_1 \cdot W_1^*\rangle = \langle W_2 \cdot W_2^*\rangle, \tag{2.6}$$

and

$$\langle V_1 \cdot V_1^*\rangle = \langle V_2 \cdot V_2^*\rangle. \tag{2.7}$$

The normalized cross-spectral density, or coherence, given by

$$\Gamma_{12}(\omega) = \frac{\langle S_{12}\rangle}{\sqrt{\langle S_{11}\rangle \cdot \langle S_{22}\rangle}}, \tag{2.8}$$

can then be found by inserting Eq. (2.4) into (2.8) and exploiting Eqs. (2.5) – (2.7), giving

$$\Gamma_{12}(\omega) = \frac{\langle W_1 \cdot W_2^* \rangle}{\langle W_1 \cdot W_1^* \rangle + \langle V_1 \cdot V_1^* \rangle} + \frac{\langle V_1 \cdot V_2^* \rangle}{\langle W_1 \cdot W_1^* \rangle + \langle V_1 \cdot V_1^* \rangle}. \tag{2.9}$$

The denominator in both terms on the right-hand side is the total received power on either sensor, while the numerators are the cross-spectral densities of the wave-generated noise in the first term and vessel-generated noise in the second.

To further simplify Eq. (2.9), we define the frequency dependent fraction of total noise power due to vessels as

$$\beta(\omega) = \frac{\langle V_1 \cdot V_1^* \rangle}{\langle S_{11} \rangle}, \tag{2.10}$$

while the fraction of the noise field due to wave-generated sound is then be given by 1- $\beta(\omega)$. With a few algebraic manipulations Eqs. (2.9) and (2.10) can be combined to give the vertical noise coherence of the total noise field as

$$\Gamma_{12}(\omega) = (1-\beta)\frac{\langle W_1 \cdot W_2^* \rangle}{\langle W_1 \cdot W_1^* \rangle} + \beta \frac{\langle V_1 \cdot V_2^* \rangle}{\langle V_1 \cdot V_1^* \rangle}, \tag{2.11}$$

or

$$\Gamma_{12}(\omega) = (1-\beta)\Gamma_{12}^{w}(\omega) + \beta\Gamma_{12}^{v}(\omega). \tag{2.12}$$

The form shown in Eq. (2.12) is particularly convenient, as it shows that the second order statistics of the total ambient noise field are indeed a weighted linear combination of the two independent fields. In the case of a normalized statistic, such as the coherence, the weights must sum to unity.

This same property is true for the directional noise density function provided that the noise field may be represented by a summation of plane waves and that it is azimuthally symmetric. In this case, the directional noise density is related to the vertical coherence by Cox's equation (Cox, 1973),

$$\Gamma_{12}(\omega) = \frac{1}{2}\int_0^{\pi} F(\theta)\, e^{-i\omega\tau_d \cos\theta} \sin\theta \, d\theta, \tag{2.13}$$

under the normalization condition

$$\frac{1}{2}\int_0^{\pi} F(\theta)\sin\theta\, d\theta = 1, \tag{2.14}$$

where $F(\theta)$ is the two-dimensional (vertical) directional density function of the total noise field, θ is the polar angle measured from zenith, $i = \sqrt{-1}$, and τ_d is the time delay where d is the spacing between the vertically-separated sensors and c is the local sound speed. The directional density function of the total noise field with vertical coherence given by Eq. (2.12) may be expressed as a weighted sum of the uncorrelated noise fields directionalities (Cox, 1973),

$$F(\theta) = (1-\beta)F_w(\theta) + \beta F_v(\theta), \tag{2.15}$$

where $F_w(\theta)$ and $F_v(\theta)$ are the directionalities of the breaking wave-generated and vessel-generated noise fields respectively. The form of Eqs. (2.12) and (2.15) are particularly convenient, as experimentally validated analytical models of wind-wave driven vertical coherence and directionality are available and straightforward to analytically compute in the deep ocean (Cron and Sherman, 1962; Barclay and Buckingham, 2013a) and in a shallow-water Pekeris waveguide (Buckingham, 1980; Kuperman and Ingenito, 1980; Harrison, 1996; Deane *et al.*, 1997), including those with a multi-layered seabed (Carbone *et al.*, 1998; Barclay *et al.*, 2019). In more complex bathymetries, including those where horizontal seabed reflection and refraction are important to include, computational models may be used to determine the spatial coherence (Barclay and Lin, 2019).

When β=0, the noise field coherence and directionality can be determined by the noise generated by surface-breaking waves in the absence of all other sources such as rain and biological sources. It should be noted that since the coherence is a normalized quantity, it does not depend on any factor related to the spectral density, such as the effective source level (sea-state and wind speed) or the frequency dependence of the wind-wave generated surface noise, provided there is some acoustic energy in the band of interest. To first order, only the local sound speed, the

bathymetry, and the effective (bulk) geoacoustic properties of the seabed must be known. The water column sound speed profile may play a second order effect, apparent in the precise location of the zero-crossings in the real part of the coherence curve (Barclay and Buckingham, 2013a). Wind-generated ambient noise coherence in shallow waters is a stable, time-independent noise property provided sufficient time averaging to include enough sources (Farmer and Vagle, 1988; Deane *et al.*, 1997; Carbone *et al.*, 1998).

When a contribution to the ambient noise field from distant shipping is apparent (β >0), the resultant change in coherence can also be seen in the directionality. The component of vessel-generated noise which propagates long distances (> 10 km) is characterized as low-frequency (< 1 kHz) and containing low-order modes (Jensen, 1994), and can be modeled accordingly. A careful examination of Cox's equation, Eq. (2.13), shows that the real part of the coherence is related to the symmetrical component of the noise directionality about the horizontal, while the imaginary part is related only to the asymmetrical component. Since distant vessel noise is best modeled as a summation of low-order modes, $F_v(\theta)$ is predominantly symmetrical about the horizontal and ship noise will contribute primarily to the real part of the vertical coherence.

From Eqs. (2.12) and (2.15), it is clear that to partition the energy in the measured spectral power density between wave-generated noise and vessel noise, the coefficient β(ω) must be estimated. In general, $\Gamma_{12}(\omega)$ is computed from the measured data, $\Gamma_{12}^{w}(\omega)$ is modelled and held constant over the observation period as wind-generated ambient noise coherence can be considered as time-independent (Deane et al., 1997; Carbone et al., 1998). $\Gamma_{12}^{v}(\omega)$ can be modelled taking into account the sound propagation environment and the effective range to the ship. Solving for $\beta(\omega)$ then allows the spectral power due to vessel noise to be determined from Eq. (2.10). The absolute power of received ship noise (RL) in dB re 1 $\mu Pa^2/Hz$ can be found by computing

$$RL(\omega) = 10 * log\{\langle S_{11}(\omega)\rangle \cdot \beta(\omega)\}, \quad (2.16)$$

while the relative contribution of the vessel noise (VN) in dB above the natural background noise can simply be expressed as

$$VN(\omega) = 10 * log\left\{\frac{\beta(\omega)}{1-\beta(\omega)}\right\}. \quad (2.17)$$

The estimation of the time-dependent parameters RL and VN in long-duration passive acoustic monitoring data sets allows the sound exposure of the receiver to vessel-generated noise to be quantified and compared against the same metric from the natural ambient soundscape. The method does not include other types of noise sources such as pile driving, dredging and soniferous aquatic animals. The theoretical formulas describing the analytical models of wind-wave generated noise and vessel noise used in this study are described in the following sub-sections.

2.3.2 Wind Driven Ambient Noise Model

The analytical model of the vertical noise coherence function in an isovelocity fluid layer over an elastic bottom half-space is developed in this section with monopole sources randomly distributed on a plane just below the pressure release surface at depth z_s. Assuming azimuthal symmetry in a cylindrical coordinate system (r,z,φ), the cross spectral density for a single source can be expressed in terms of the depth-dependent Green's function

$$S_{12}(\omega) = 2Q^2 G(r, z_s, z_1, \omega) G^*(r, z_s, z_2, \omega), \quad (2.18)$$

where Q is the source strength, the source depth is z_s, r is the horizontal range between the source and the receiver, and $G(.)$ are Green's functions between the source and each of the receivers at depths z_1 and z_2. Eq. (2.18) can then be integrated for the distribution of sources over all azimuth and range to find the cross-spectral density, giving

$$S_{12}(\omega) = 4\pi v Q^2 \int_0^\infty G(r, z_s, z_1, \omega)\, G^*(r, z_s, z_2, \omega) r dr, \quad (2.19)$$

where v is the mean rate of wave breaking events per unit area, and azimuthal symmetry has been assumed. The Green's function solution for the noise field can be expressed as a sum of normal modes (Worzel *et al.*, 1948). For an isovelocity profile, the normal mode decomposition of the Green's functions for a fluid waveguide over a lossy, elastic half-space with a sufficiently slow shear speed can be computed using the complex effective depth approach (Zhang and Tindle, 1993), where the mode functions become trigonometric functions and the modal eigenvalues can be efficiently and exactly computed (Chapman *et al.*, 1989). The Green's function is then the modal sum

$$G(r, \omega, z_i) = i\pi \sum_{n=1}^{\infty} N_n^2 \sin(\gamma_n z_s) \sin(\gamma_n z_1) H_0^1(k_n r), \tag{2.20}$$

where γ_n is the vertical wavenumber, n is the mode number, and $H_0^1(.)$ is the zeroth order Hankel function of the first kind which depends on the modal eigenvalue k_n and the range. The mode amplitude, N_n, which depends on seabed reflection loss and a practical upper limit to the sum in Eq. (2.20) for long distance propagating modes can be obtained by following the complex effective depth approach (Zhang and Tindle, 1993). By substituting the modal expansion of the Green's functions into Eq. (2.18) and exploiting the orthogonality of the Hankel functions to compute the integral over range, the cross-spectral density for the entire surface area can be simplified to the double modal sum:

$$S_{12}(\omega) = 16\pi v Q^2 \sum_{n=1}^{\infty} N_n^2 \sin(\gamma_n z_s) \sin(\gamma_n z_1) \sum_{m=1}^{\infty} N^{*2}{}_m \sin(\gamma_m z_s) \sin(\gamma_m z_2) \frac{\ln(k_n/k_m^*) - i\pi}{k^{*2}{}_m - k_n^2}, \tag{2.21}$$

where n indexes over the first Green's function, and m the second. The cross-spectral density reduces to the power spectral density when $z_1 = z_2$, so Eq. (2.21) can be combined with Eq. (2.8) to give the vertical noise coherence in a shallow water, isovelocity waveguide with an elastic seabed.

2.3.3 Ship Noise Model

To model shipping, the pressure field generated by a single source is computed using the same normal mode solution for a shallow water waveguide. The Green's function to describe the acoustic pressure due to a single source in the wave guide is given by Eq. (2.20), where z_s is now the source depth of the vessel. The power spectrum and cross-spectrum can be computed by directly substituting Eq. (2.20) into Eq. (2.18), providing all the necessary terms for the vertical coherence shown in Eq. (2.8). In this case, the received sound level, coherence, and directionality depend on the range between the receiver and vessel. Thus, the resultant coherence due to ship noise can be expressed as a function of range and frequency.

2.4 Data and Results

2.4.1 Acoustic Data Analysis

Time-series ambient noise data from the top-most hydrophone (channel 0) in SHRU were used to calculate the Power Spectral Density (PSD). 120 estimates of the PSD were made every minute using a 9765-point Fast Fourier Transform (FFT), corresponding to an interval time of 1 second, each with a 50% overlap and tapered with a Hann window. These estimates were averaged every 60 seconds to produce a single PSD for each one-minute recording and a long-term spectrogram was produced by concatenating the results over the entire period of observation, shown in Figure 2.2(a). At low frequencies (below 500 Hz), non-radiating pressure fluctuations caused by flow over the surface of hydrophone as well as mooring motion dominate the PSD. The daily modulation in the PSD in this band occurs with the frequencies of the local tidal cycles.

The noise generated by ship traffic is present in this band and extends up to 1.5 kHz when vessels are present. Though the presence of vessels can be identified in the spectrogram, quantifying their contribution to the total ambient noise field using the PSD with dynamic

environment conditions is cumbersome. When there is no vessel near (< 10 km) the receiver, the band 0.5 - 4.8 kHz is dominated by sea-surface agitation related to wind generated waves. The qualitative relationship between sea-state and noise level in the frequency band 1.95-2.05 kHz is shown in Figure 2.2(b) where the five-minute averaged wind speed is plotted along with the PSD.

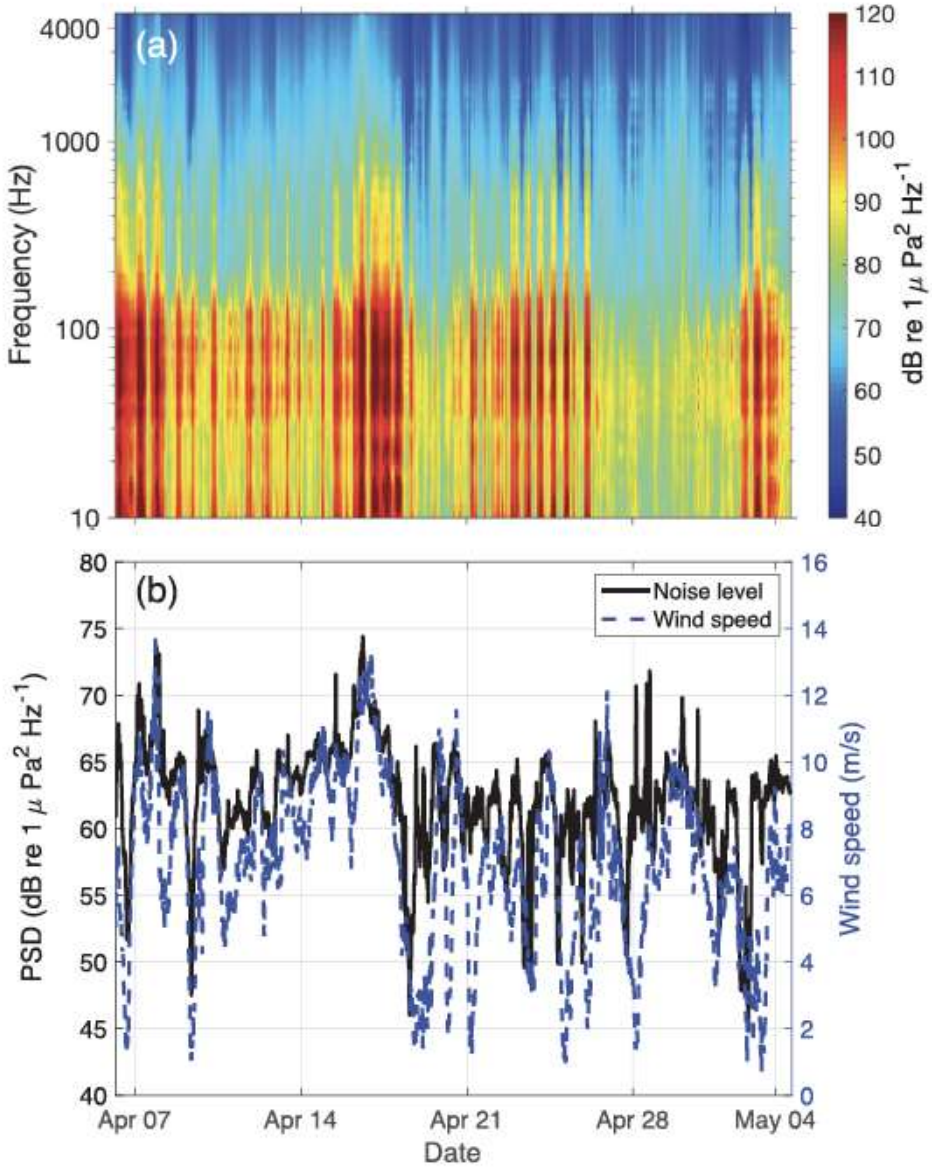

Figure 2.2: (a) Spectrogram of the entire period of observation from the top hydrophone (channel 0) and (b) the comparison between the five-minute averaged wind speed and the power spectral density in the frequency band 1.95-2.05 kHz.

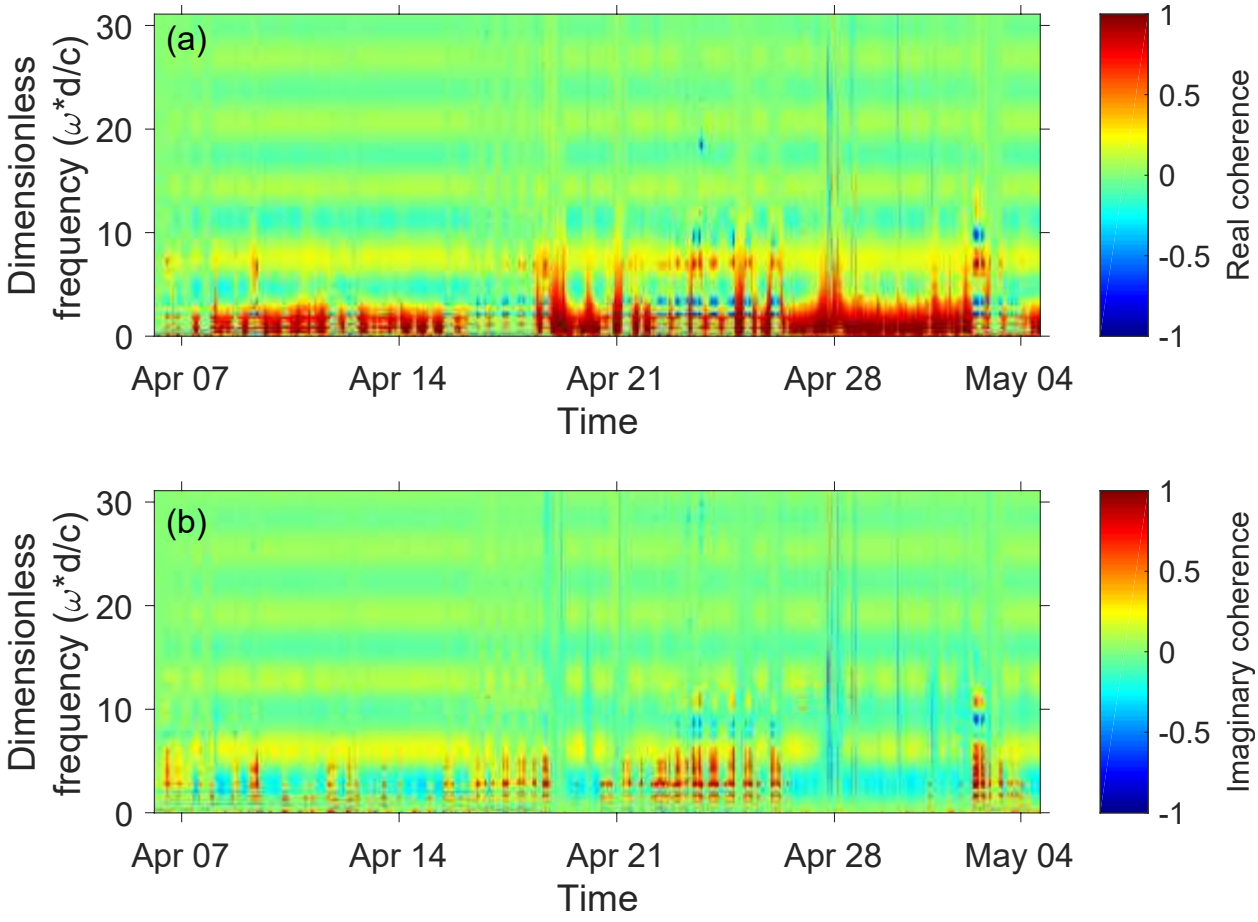

Figure 2.3: The (a) real and (b) imaginary components of the coherence as a function of frequency for the entire period of observation.

The cross-spectrum was calculated using the same parameters as the PSD and normalized by the respective PSD from each sensor to retrieve the vertical noise coherence as described by Eq. (2.8). The real and imaginary part of the coherence over the entire data collection period are shown as a coherogram (analogous to a spectrogram) in Figure 2.3. Degradation in the coherence at low frequencies (below 500 Hz, or 3.2 in dimensionless frequency) is visible in both real and imaginary components of the coherogram caused by non-radiated (spatially uncorrelated) pressure fluctuations, or flow noise, on the individual sensors. The oscillatory nature of wind-generated ambient noise coherence is evident in the coherogram (above 500 Hz, or 3.2 in dimensionless

frequency), with stable zero-crossings in frequency for the entire period of observation. The coherogram shows deviation from normal wind-coherence at certain periods due to local and distant ship traffic. Close inspection of the vertical noise coherence reveals the presence of distant shipping in the dataset below 1.5 kHz, or 9.5 in dimensionless frequency, which can be identified as a broadband increase in real coherence, while several close-range ships can be identified by short-duration spikes over the entire acoustic bandwidth in both the real and imaginary components.

Each one-minute sample that makes up the coherogram can be categorized into three main source classes: wind-generated, close-range ship, or distant shipping. Examples of the real and imaginary coherence components of these distinct sources are shown in Figure 2.4. The most dominant and stable coherence pattern observed in the dataset is caused by wind-generated ambient noise alone, showing oscillating curves with several zero-crossings, with decreasing coherence with increasing dimensionless frequency. The presence of the imaginary component indicates an asymmetry in the noise field, while the amplitude suggests energy is propagating downward with weaker reflection from the seabed.

The second class of coherence present in the data is that of an individual close range (< 10 km) ship, where the wind-generated noise is masked. The real and imaginary components show a high coherence over the entire frequency range with several zero crossings that depend on the distance between the source and the receivers. As the ship passes by the receiver, a parabolic shaped phase interference pattern is formed in the coherogram due to the interaction between direct waves and their reflection from the waveguide boundaries.

The third class of coherence observed is due to distant shipping in the frequency band 0.1 - 1.5 kHz. At frequencies above 1.5 kHz, the coherence follows that of the wind-generated curve,

since the typical vessel source spectrum which decreases in power with increasing frequency and the attenuation of propagating sound caused by bottom interaction increases with frequency and falls below the background noise. At frequencies below 1.5 kHz, low order modes (near horizontally propagating sound) arrive at the sensors very nearly in phase and raise the real part of the coherence, while pushing the imaginary component towards zero due to the increased symmetry in the noise field. The alteration in the coherence pattern due to distant shipping depends on both the range and relative power of the ship noise level compared to the background wind-generated noise.

The three classes of coherence shown in Figure 2.4 were simulated using the analytical models described in Section III. The modelled vertical coherence of ambient noise computed using Eq. (2.21), is compared with data in Figure 2.4(a) and 2.4(b). The water column sound speed ($c_w = 1494\ m/s$) and density ($\rho_w = 1024\ kg/m^3$) were obtained from CTD data at the receiver position. The compressional sound speed of sediment was taken from US geological survey data ($c_b = 1620\ m/s$) close to the noise measurement location. For the remaining geoacoustic properties such as shear speed ($c_s = 45\ m/s$), density ($\rho_b = 1900\ kg/m^3$), compressional attenuation ($\alpha_b = 0.9\ dB/\lambda$), and shear attenuation ($\alpha_s = 2\ dB/\lambda$), Hamilton's geoacoustic model for the continental slope environment was used (Baggeroer *et al.*, 1988; Brienzo and Hodgkiss, 1993).

The coherence for noise from an individual ship at close range was computed by substituting Eq. (2.20) with the source depth as 7 m (z_s) into Eq. (2.19), using the same geoacoustic parameters listed above, and by brute force searching over the unknown horizontal range parameter (Wales and Heitmeyer, 2002; Gassmann et al,2017). The best fit between model output and data occurred at 380 m, which is the closest point of approach for this particular contact, shown

in Figure 2.4(c) and (d). The figure shows the comparison of real and imaginary coherence between data and model. Model data comparisons of vertical coherence are an effective method for ranging ships in shallow water waveguides (Shajahan and Barclay, 2019).

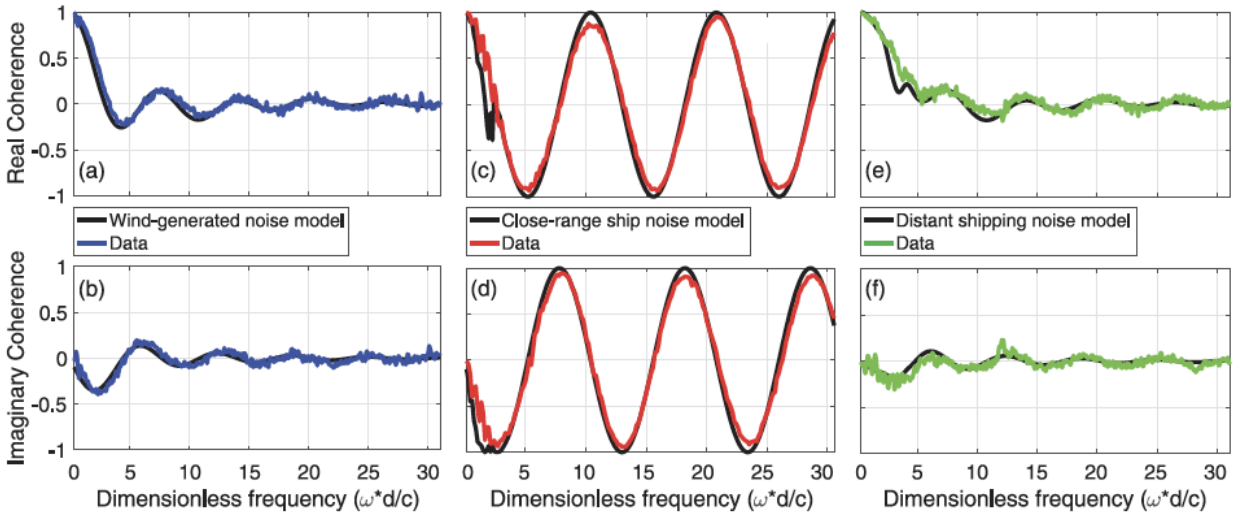

Figure 2.4: The real and imaginary components of the three classes of observed coherence, (a) – (b) wind generated data (blue) and model (black), (c) – (d) individual close-range ship data (red) and model (black), and (e) – (f) distant shipping data (green) and model (black).

The vertical coherence of distant shipping was simulated using both the ambient noise model given by Eq.'s (2.21) and (2.8) and the normal mode sound propagation model given by combining Equations (2.18), (2.20) and (2.8). Note that the details of the source spectrum (e.g. the wave breaking rate per unit area, ν), cancel in Eq. (2.8). The CSD and PSD were also calculated by the incoherent sum of the first 10 modes computed using Eq. (2.20) where the ship was assumed to be stationary at 10 km. The comparison between data and model with the same geoacoustic parameters as described above is shown in Figure 2.4(e) and 2.4(f), where the best-fit relative power between the distant ship noise and wind-generated noise was determined by brute force search over $\beta(\omega)$.

2.4.2 Quantifying Ship Noise

To determine the relative contribution of ship noise to the total power spectrum, β(ω) must be estimated by inverting Eq. (2.12). A combination of the wind-driven ambient noise and ship noise models derived from Eqs. (2.18) – (2.21) can be used to compute $\Gamma_{12}^{w}(\omega)$ and $\Gamma_{12}^{v}(\omega)$, where the latter depends on the range between the ship and receiver. In general, the frequency dependence of β(ω) should reflect frequency dependence of a typical vessel. A closed-form model adapted from Deane (Deane *et al.*, 1997) is used to obtain the frequency dependence for $\beta(\omega)$,

$$\beta(\omega) = \frac{2\tilde{\beta}}{(\omega/\omega_1)^n + (\omega_1/\omega)^n}, \tag{2.22}$$

where *n* determines the roll-off in dB per octave and ω_1 is the peak frequency of the source, chosen to be 350 Hz. The inversion in Eq. (2.12) now depends on three free parameters: range $(R = 0.1 - 15\ km)$, roll-off $(n = 2 - 6\ dB/octave)$, representing a broad description of the ship's source spectrum, and relative weighting $(\tilde{\beta} = 0 - 1)$, where the values in the parentheses are the search domains for each variable. The inversion method is a brute force search over the three parameters aiming to minimize the error between simulated coherence (the right-hand side of Eq. (2.12)) and measured coherence (the left-hand side of Eq. (2.12)) at each time step. The inversion was carried out at each 5-minute interval of acoustic data over the entire period of observation. The best fit between model and data was determined by minimizing the value of root mean square (RMS) error computed as

$$\xi(R, \tilde{\beta}, n) = \frac{1}{N}\sqrt{\sum_{i=1}^{N}\left[\Gamma_{12}^{data}(\omega_i) - \Gamma_{12}^{model}(\omega_i, R, \tilde{\beta}, n)\right]^2}, \tag{2.23}$$

where N is the total number of frequency points in the band 350 Hz - 4.8 kHz, and Γ_{12}^{model} and Γ_{12}^{data} are the simulated and measured coherence respectively. The band-limited computation of

the RMS error was chosen to avoid misfit caused by flow noise and motivated the choice of the peak source frequency, though large sea-going vessels typically have a source spectrum with a peak below this low-frequency limit. The absolute coherogram of the measurement, the corresponding best fit after inversion, and the fit residual are shown in Figures 2.5(a), 2.5(b) and 2.5(c) respectively.

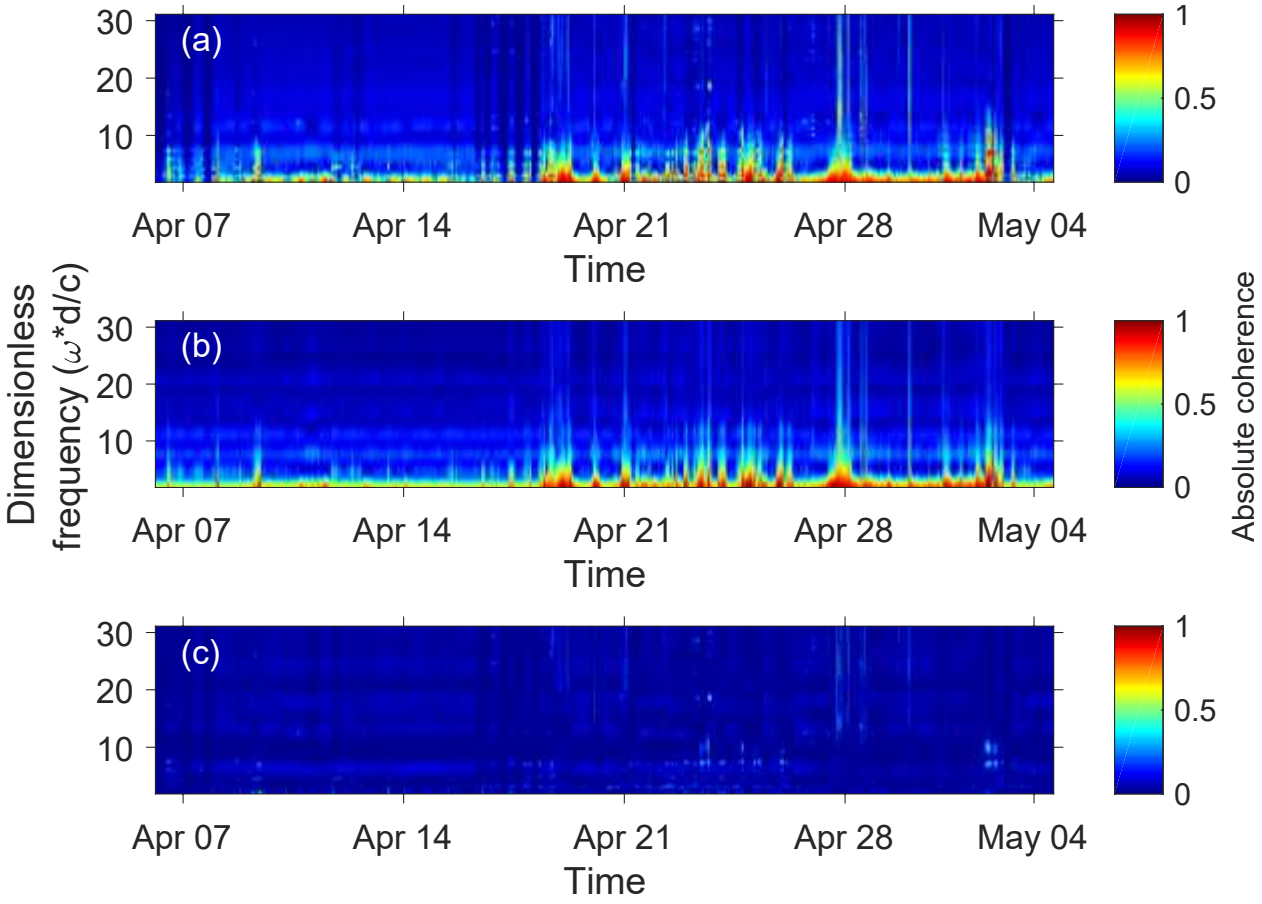

Figure 2.5: The (a) measured and (b) best-fit modeled absolute vertical noise coherence over the observations period, and (c) the fit residuals

The time series of the coherogram from the inversion results compared very well with the measured coherogram. The two-component noise coherence model given by Eq. (2.12) distinctly reproduces the observed effects of both distant and close-range shipping. Some features of the data not reproduced by the model may be due to biological sources in the vicinity of the receivers or by

strong tones present in the ship noise spectra which cannot be captured by the model presented in Eq. (2.22).

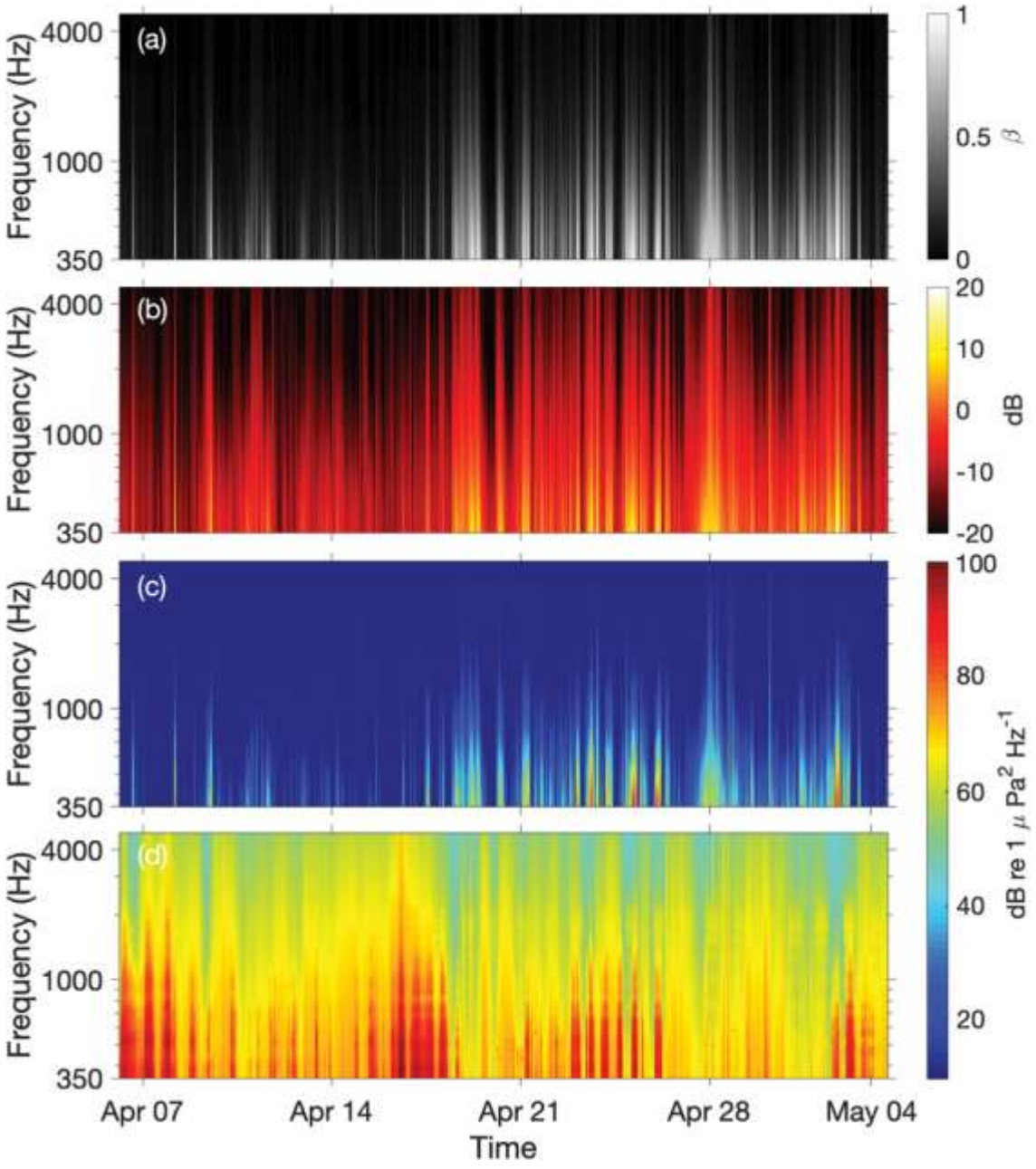

Figure 2.6: The (a) best-fit of $\beta(\omega)$ after inversion, (b) relative contribution of shipping to the overall noise field, (c) absolute contribution of shipping to the overall noise field and (d) total received noise level.

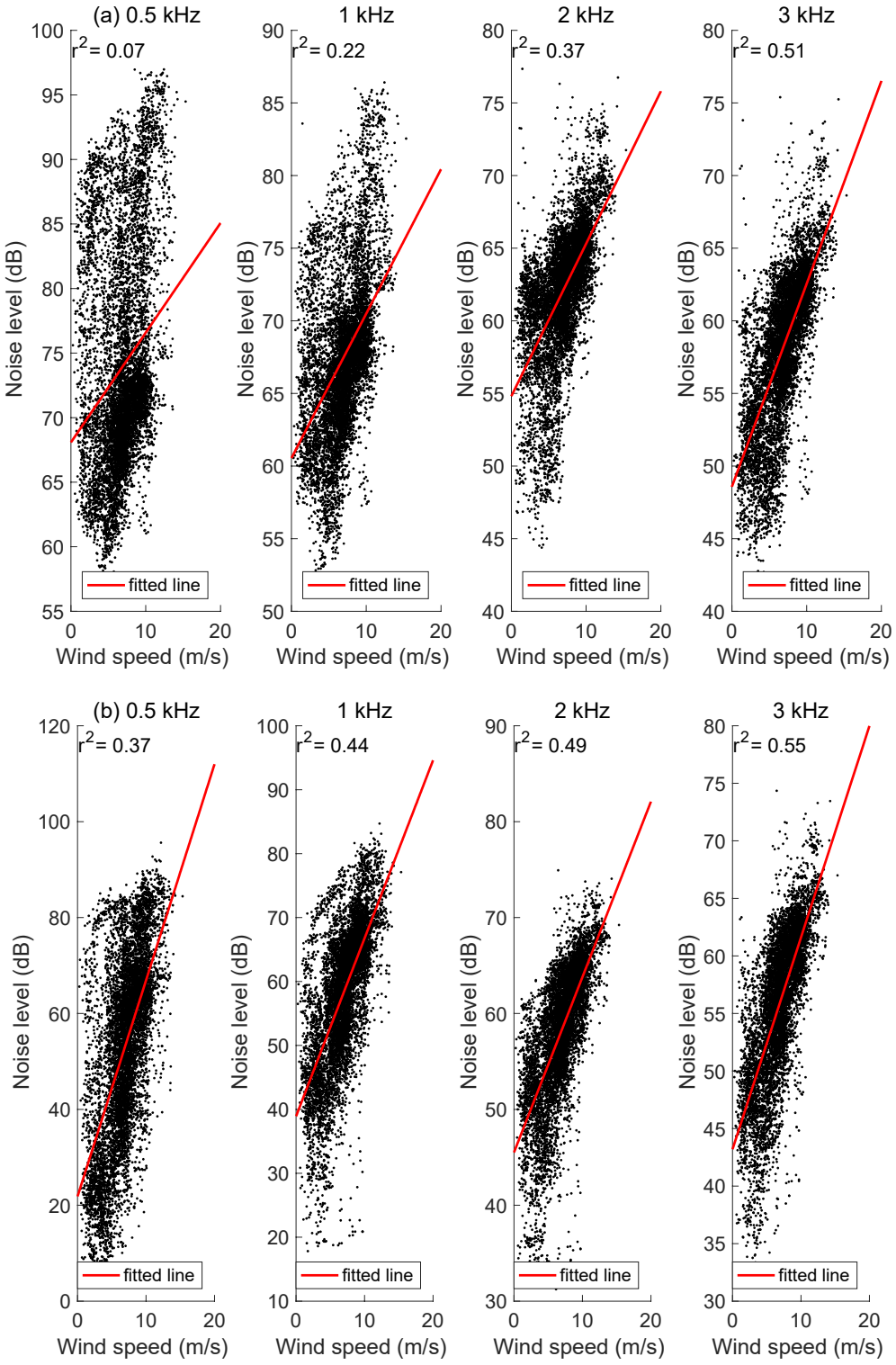

Figure 2.7: Correlation coefficient analysis between wind speed and (a) total received noise level and (b) best-fit wind-generated noise level at 500 Hz, 1 kHz, 2 kHz, and 3 kHz.

The estimated relative contribution of ship noise to the total noise field is shown in terms of the fraction of total power, or $\beta(\omega)$, in Figure 2.6(a) and in terms of relative power measured in dB in Figure 2.6(b). During the first half of observation the influence of shipping is limited to distant passing ships while in the second half, distant and close-range shipping is present, shown by the high values of $\beta(\omega)$ across the entire band. During the second half of the recording, ship noise dominates the noise field below 1 kHz with β~1. When individual ships approach the receiver, the relative ship noise contribution is as much as 40 dB above the wind-generated background sound at low frequencies, which is consistent with previously reported studies (Wales and Heitmeyer, 2002). The received level solely due to ship noise can be estimated from the inversion result of $\beta(\omega)$ and total received noise by Eq. (2.16). The power of received ship noise at the sensor in dB re 1 mPa^2/Hz and total noise power are shown in Figures 2.6(c) and 2.6(d) respectively.

In order to demonstrate the effectiveness of this method in partitioning the total noise field into shipping and wind noise components, the correlation coefficients between the noise power and wind speed at 10 m above the sea surface, shown in Figure 2.2, were computed and compared using either the total received noise or the inversion-derived wind-generated noise. The coefficient of determination ($\boldsymbol{r^2}$) between a five-minute averaged total received noise level and wind speed at 500 Hz, 1 kHz, 2 kHz and 3 kHz were computed and shown along with the data in Figure 2.7(a). At 0.5 kHz the noise level shows a very weak correlation ($\boldsymbol{r^2} = 0.07$) with wind speed due to the masking by ship noise. As the frequency increases from 0.5 to 3 kHz, $\boldsymbol{r^2}$ also improves from a low to moderate positive correlation due to the frequency dependent nature of ship noise.

The inverted noise contribution due to shipping was subtracted from the total received level to produce an estimate of the purely wind-generated noise field, which was then plotted against

wind speed and used to compute the r^2 values, shown in Figure 2.7(b). At the lowest frequency (500 Hz) a greater than fivefold increase in the value of correlation coefficient ($r^2 = 0.37$) is seen. As the frequency increases, the ship noise contribution diminishes and the improvements in r^2 decrease to 8% at 3 kHz. By considering the vertical coherence as a linear combination of wind and ship noise, this method demonstrates the effectiveness of noise field separation in quantifying the contribution of anthropogenic activity on the marine habitat.

2.5 Conclusions

A processing technique for time-series ambient noise data based on spatial coherence has been described in this chapter. The coherence function is widely used in signal processing to extract environmental information which is eventually used for transmission loss estimation in sonar performance modeling. In the present study, a coherogram has been used for classifying major sound sources present in the environment. The analysis involves the use of data in association with noise models to understand the impact of different sources on noise spatial characteristics. The surface distributed noise as well as distant and close-range shipping were identified as the major sources of sound present in the measurement. Analytical models of ambient noise and sound propagation were used to simulate vertical coherence and compared with experimental data. The agreement between data and model for wind and shipping provided the motivation to use the model in association with the data to invert the influence of ship noise level. The data-model fitting of the coherence provided both the relative and absolute contribution of shipping in the overall noise field.

In recent years, the ambient noise level in the ocean has increased due to increased commercial ship traffic. Thus, continuous long-term monitoring is required to understand the effect of anthropogenic noise on marine species. The present work demonstrates the capability of

using a hydrophone VLA in long term PAM systems for an effective estimation of the anthropogenic contribution. The coherence-based analysis presented here has the advantage of quantifying ship noise impact without prior knowledge of environmental information such as wind speed and ship distribution. In addition to that, data model fitting of the coherogram from close-range shipping can be used for source localization and range-dependent geo-acoustic inversion.

CHAPTER 3

THREE-DIMENSIONAL VESSEL LOCALIZATION WITH A PAIR OF VERTICALLY SPACED, OMNI-DIRECTIONAL HYDROPHONES

3.1 Introduction

Sound propagation in the ocean depends on the three-dimensional sound speed profile, bathymetry, sediment composition, sea surface roughness, and on the frequency of the signal (Jensen *et al*, 2011). When seas are calm, sound generated by a broadband source is totally internally reflected at the sea surface, resulting in the formation of a frequency-dependent interference pattern which depends on the source-receiver separation distance and the source depth. In the spectrogram, a shallow (relative to the wavelength) sound source moving past a fixed receiver at a constant speed and heading creates a parabolic shaped fringing pattern commonly known as Lloyd's Mirror or the Image Interference-Effect (Young, 1947; Urick, 1967; Carey, 2009). The pattern arises from the coherent interaction of the direct wave and the surface reflected wave, forming regions of high (constructive interference) and low (destructive interference) intensity. Ships are generators of both narrow and broadband signals due to rotating machinery: generators, diesel engines, drive trains and propellers, spanning a bandwidth from 50 Hz to 10 kHz (McKenna et al, 2012), which often give rise to the Llyod's Mirror pattern. Thus, the time-dependent ranging of vessels can be done using data collected from a single hydrophone, returning a ship's speed, closest point of approach (CPA), and some sense of its route, be it a straight line, holding station, or more complex maneuvers. When the single receiver is replaced by two vertically-spaced hydrophones, a similar phenomenon can be exploited, where the fringing pattern

now appears in the normalized cross-spectrum, or coherence, and is generated by the interference between two direct source-receiver paths. This coherence fringing pattern can be reliably modelled (Shajahan *et al.*, 2020) and depends on the vertical spacing of the phones and horizontal range of the acoustic source. In this chapter, it is shown that in a three-dimensional environment, the time-dependent vertical coherence can be used to estimate vessel range, CPA, speed, and, in regions with asymmetric bathymetry, bearing.

Matched field processing techniques have been widely used for localizing acoustic sources based on measured auto-spectra and cross-spectra (Westwood, 1992; Michalopoulou and Porter, 1996). Amplitude and phase data on an array are simulated using a numerical propagation code over a domain of possible source positions and compared to the received signal, searching for the best match between the model and data. Efforts to replace the simulated fields with real measurements have been made (Fialkowski *et al.*, 2000), including the use of opportunistic data labeled with Automatic Identification System (AIS) position data. In this case, measurements from the same horizontally-separated vertical line arrays were able to provide the location of ships based on comparisons between the time-domain cross-correlation outputs (Verlinden *et al.*, 2015).

In many studies, simple analytical models of sound propagation have been effectively used for source localization. The time delay between direct and surface reflected (D-SR) arrivals measured on a single hydrophone in deep waters can be successfully used for localizing a moving source (Duan et al, 2014). The source location can be determined from the changing D-SR time delays obtained from the autocorrelation function. Lloyd's Mirror Effect observed in Ocean-bottom seismometers (OBS) has been used to estimate the depth of fin whale vocalization with a prior knowledge of horizontal range (Pereira *et al.*, 2016). This technique has been used to obtain the range and depth of sperm whales using a towed hydrophone array at short ranges (< 2km) assuming

uniform water column sound speed (Thode, 2004). The same method can be expanded for tracking whales in three dimensions in a refracting water column (Thode, 2005). Source depths have been estimated using the broadband interference structure in array data in the time-frequency domain based on matched field processing (Duan *et al*, 2017; Yang *et al*, 2018). Cross-correlation function matching of broadband signals received on two vertically-oriented hydrophones has been used for tracking acoustics sources, again exploiting the interference between direct and surface reflected arrivals (Lie et al, 2016).

In a more complex ocean, the spatial variation in sound speed and bathymetry causes horizontal refraction, which demands the use of three-dimensional models for the accurate representation of the pressure field instead of assuming azimuthal symmetry. As sound propagates along a sloping bathymetry, multiple interactions with the boundaries will initiate out of plane propagation (Ballard *et al.*, 2012), which can lead to received acoustic power and arrival times not predicted by conventional two dimensional models (Heaney and Murray, 2009; Sagers et al, 2014; Lin et al, 2019; Stephen et al, 2019). Topographic features such as a submarine canyon or seafloor scours cause horizontal refraction and 3-D models were used to confirm the experimental data evidence (Chiu et al, 2011; Ballard et al, 2012; Lin et al, 2015). Internal waves can also induce horizontal refraction which results in signal fluctuation in shallow waters (Badiey et al, 2005; Lynch et al, 2010; Lin *et al*, 2013.

The prospect of exploiting the three-dimensional nature of the ocean for passive acoustic localization using matched field processing has been proposed and demonstrated in simulations (Perkins and Kuperman, 1990; Zala and Ozard, 1990). For the case of impulsive sources, simulated and observed time of arrival data were compared to effectively track beaked whales in three-dimensions on a single hydrophone (Tiemann *et al.*, 2006).

This chapter shows the three-dimensional localization of a moving ship near a submarine canyon using normalized cross-spectrum (coherence) between two vertically-positioned omni-directional hydrophones. As the vertical coherence is a normalized quantity, the method emphasizes the matching of predicted phase data to the observations, as opposed to the complete complex acoustic field. First, a model-data comparison of vertical coherence for a Pekeris waveguide is used to estimate the range of a passing ship at each time step. Horizontal refraction of sound caused by the bathymetry of the canyon causes a 3-D effect apparent in the coherogram, which is exploited to obtain the bearing using a 3-D sound propagation model. This method is suitable for continuous broadband sources in shallow water environments, where conventional image interference effect methods become difficult due to multipath arrivals. Thus, the use of coherence in source localization is a suitable method in shallow water regions

The remaining sections of this chapter are arranged as follows. Section 3.2 outlines the details of noise measurement and auxiliary data used in the analysis. In section 3.3, the basic theory of image interference effect in an isovelocity and Pekeris waveguide is presented, along with a brief description of the 3-D PE model and BELLHOP3D models used in this study. Observations of vertical coherence of sound from a moving vessel are compared to simulation results and the results of source localization are presented in section 3.4. Section 3.5 summarizes the results and discusses the advantages and limitations of the coherence-based source localization technique presented in this Chapter.

3.2 Vertical Noise Coherence in Alvin Canyon

3.2.1 Study Area

The passive acoustic data used in this study were measured near the head of Alvin Canyon, located south of Martha's Vineyard, Massachusetts. The acoustic data were recorded using Woods

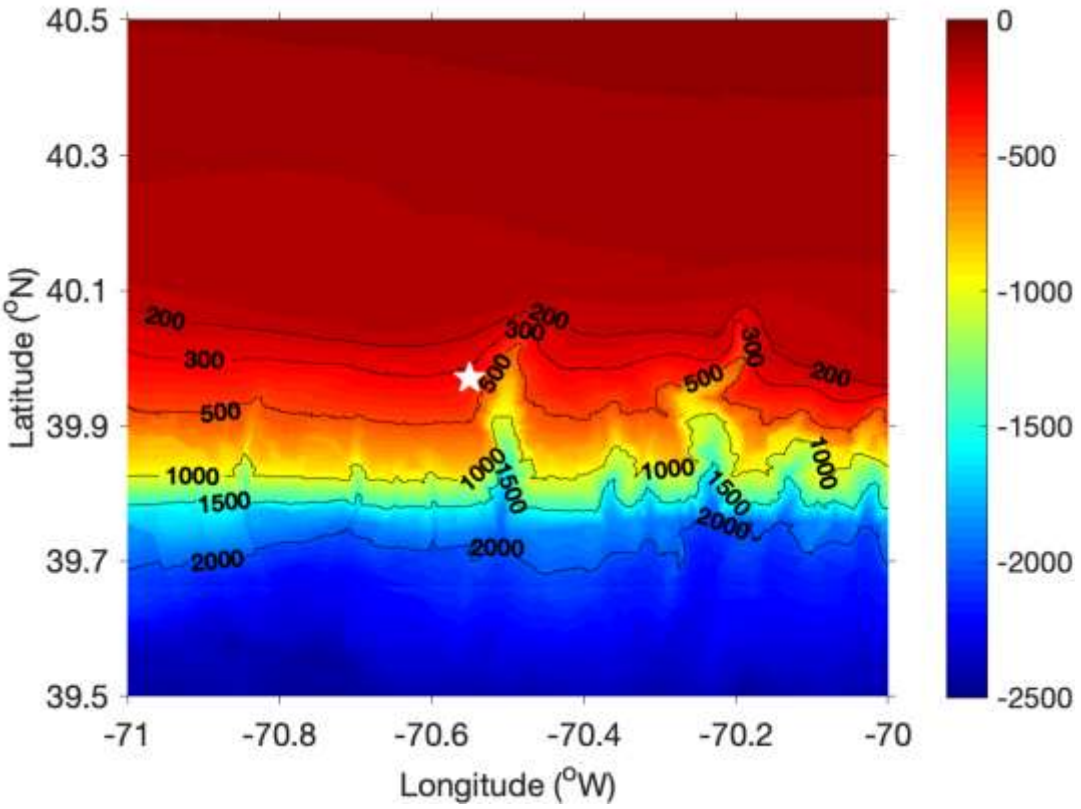

Figure 3.1: The bathymetry and location of the ambient noise measurement site near Alvin Canyon (white star).

Hole Oceanographic Institute's (WHOI) Several Hydrophone Receiving Unit (SHRU) configured as a Vertical Line Array (VLA) on a sub-surface mooring. The measurement system was used to collect 29 days of continuous ambient sound pressure time-series data from April 6th to May 4th in 2016. The SHRU VLA consisted of four hydrophones with a total length of 9.5 m. The sampling rate of acoustic data was 9765.625 Hz with a usable acoustic bandwidth from 10-4880 Hz. The receive sensitivity of the omnidirectional hydrophones was reported by the manufacturer as -170 dB $\mu Pa/V$. Temperature and pressure sensors attached along the mooring recorded the water column temperature and mooring tilt, sampling continuously at every 30 seconds. The location of

the mooring site was at 39° 58.32' N, 70° 32.94' W. The bathymetry of the region marked with the location of the mooring is given in Figure 3.1. The water column depth at the mooring location was approximately 350 m.

The inputs required for the 2-D and 3-D computational sound propagation models used in this study are the water column sound speed, sediment geoacoustic properties, and the bathymetry of the region. The temperature sensors attached to SHRU were used to obtain the sound speed in the water column by assuming a standard seawater salinity of 35 PSU. US geological survey data from the location were used to determine the bulk sediment geoacoustic properties (compressional sound speed, c_b, attenuation, α_b, and density, ρ_b) over the study area, by consulting Hamilton's geoacoustic model for the continental slope environment (Hamilton, 1980; Reid *et al.*, 2005; Jensen *et al.*, 2011). Bathymetric data were drawn from the Global multi Resolution Topography (GMRT) database with ~45 m resolution in latitude and ~70 m in longitude (Ryan *et al.*, 2009).

3.2.2 Acoustic Data Processing

Time-series ambient noise data from the vertical array were used to calculate the PSD and CSD for different sensor combinations using

$$\langle S_{ij}(\omega)\rangle = \langle \frac{X_i \cdot X_j^*}{T} \rangle, \tag{3.1}$$

where X_i is the Fourier transformed pressure time series on the i-th sensor, T is the observing duration, * denotes the complex conjugate and the angle brackets indicate an ensemble average. When $i = j$, the PSD is computed, otherwise the CSD is given. Both were computed over 1 s segments using a 9765-point FFT and Hann window with 50 % overlap. These estimates were averaged over every 60-s to produce a single PSD and CSD for each one-minute recording. The vertical coherence, or normalized CSD for each sensor spacing (combination) was computed using

$$\Gamma_{ij}(\omega) = \frac{\langle S_{ij} \rangle}{\sqrt{\langle S_{ii} \rangle \cdot \langle S_{jj} \rangle}}. \tag{3.2}$$

and a long-term spectrogram and coherogram (time-frequency plot of the real and imaginary components of the vertical coherence) were generated by concatenating the results over the entire period of observation. The long-term spectrogram was used to identify the presence of sound generated by wind, distant shipping, close-range vessel activity, and flow noise and a method to partition the PSD into ship generated and wind generated noise components using the modeled coherence was developed, described in previous work (Shajahan *et al.*, 2020) and in chapter 2. Close-range shipping datasets were identified by the presence of the Lloyd's Mirror Effect in the spectrogram and thirteen such incidents were observed in the entire month-long dataset. These instances were extracted from the data set and are the focus of the analysis presented in this chapter.

3.3 Modelling the Image Interference Effect

3.3.1 Homogeneous Half-space

The analytical theory presented below considers the ocean environment as an isovelocity half-space with an infinite depth bounded above by a flat, pressure release sea surface. At any point, the sound field produced by a broadband acoustic source positioned near the surface consists of a superposition of the direct and surface reflected waves. The reflected field may be reproduced by placing an equivalent strength source with opposite polarity equidistant to the surface thus satisfying the pressure release boundary condition (Carey, 2009). By this method of images, when a broadband source with the frequency dependent strength $Q(\omega)$ is positioned at a distance z_S below the sea surface, the total field *P* at any point in the waveguide may be expressed as

$$P(\omega, r, z_r) = Q\left(\frac{e^{ikr_S}}{r_S} - \frac{e^{ikr_I}}{r_I}\right), \tag{3.3}$$

where r_S and r_I are the slant ranges to the real and image sources respectively, $k = 2\pi/\lambda$ is the wavenumber, and $i = \sqrt{-1}$. If z_r is the receiver depth and r is the horizontal range between source and receiver, the slant ranges can be expressed as

$$r_S = \sqrt{r^2 + (z_r - z_S)^2} \quad \text{and} \quad r_I = \sqrt{r^2 + (z_r + z_S)^2}. \tag{3.4}$$

Assuming the slant ranges are large compared to the source depth, Eq. (3.3) can be expressed in a simplified form as a function of declination angle θ and the distance from the mid-point between the real and image sources to the receiver, R,

$$P(\omega, r, z_r) = \frac{-2Qi}{R} \sin(kz_S \sin\theta)\, e^{ikR}, \tag{3.5}$$

Considering two vertically-oriented receivers positioned at z_1 and z_2 separated by a distance *d*, the cross-spectrum of the signals received at these points are the product of field $P_1(\omega, r, z_1)$ and the complex conjugate of field $P_2(\omega, r, z_2)$. The cross-spectrum in the waveguide can be expressed using Eq. (3.5) as

$$S_{12}(\omega, r) = \frac{-4Q^2}{R_1 R_2} \sin(kz_S \sin\theta_2) \sin(kz_S \sin\theta_2) \;\; e^{ik(R_1 - R_2)}\,. \tag{3.6}$$

The cross-spectrum is a complex quantity which provides the phase relationship between signals at the two receivers. When $R \gg z_S$, the real part and imaginary parts of S_{12} represent the in-phase and out of phase signal components, respectively. From Eq. (3.6), the maxima for the real and imaginary component of the cross-spectrum can be found when

$$k(R_1 - R_2) = 2n\pi \tag{3.7a}$$

and

$$k(R_1 - R_2) = \left(2n + \tfrac{1}{2}\right)\pi \qquad n = 0,1,2,3 \ldots \tag{3.7b}$$

From Eq. (3.7), it is clear that the maxima in the cross-spectrum depend on frequency, sensor separation and range to the source. For a broadband source such as ship-generated noise, a

harmonic series of striations will appear in a plot of the time-varying cross-spectrum, where the slope of the striations gives the vessel's radial speed. The normalized cross-spectral density, or coherence, is given by

$$\Gamma_{12}(\omega, r) = \frac{S_{12}(r,\omega)}{\sqrt{|P_1(r,\omega)|^2\ |P_2(r,\omega)|^2}}. \tag{3.8}$$

where the power spectra, P_1 and P_2, are given by Eq. (3.5). Since the coherence is a normalized quantity, the details of the frequency dependent source level do not affect the striations in the coherogram. Thus, the striations present in the coherogram can be used for localizing the source by applying striation tracking techniques (Duan *et al*, 2014; Duan *et al*, 2017).

3.3.2 Pekeris Waveguide

The Pekeris waveguide is a canonical environment, assuming a constant sound speed water column above a fluid half-space, where the pressure field of a broadband acoustic source in such an environment can be represented as a sum of normal modes (Jensen *et al*, 2011). The closed form solution for the pressure as a function of frequency, depth, and range is given by

$$P(\omega, z, r) = \frac{i}{4\,\rho(z_s)} \sum_{m=1}^{M} \varphi_m(z_S)\varphi_m(z)\, H_0^1(k_m r), \tag{3.9}$$

where ρ is the density of water, k_m and $\varphi_m(.)$ are the horizontal wave number and mode function, respectively, associated with the m-th mode, and $H_0^1(.)$ is the zeroth order Hankel function of the first kind. *M* is the minimum number of modes required to represent the field between the source and the receiver. Applying the asymptotic expansion of the Hankel function, the cross-spectrum of signals received at z_1 and z_2, two vertically-separated points in the waveguide, can be derived using Eq. (3.8), as

$$S_{12}(\omega, r) = \frac{1}{\rho^2(z_s) 8\pi r} \sum_{m=n} \varphi_m^2(z_S)\, \varphi_m(z_1)\varphi_m^*(z_2) \frac{e^{-2\delta_n r}}{k_m} +$$

$$\sum_{m \neq n} \varphi_m(z_S)\varphi_n^*(z_S)\, \varphi_m(z_1)\varphi_n^*(z_2) \frac{e^{-[(\delta_m+\delta_n)+i(k_m-k_n)\times r]}}{\sqrt{k_m k_n}} \tag{3.10}$$

where δ_m is the attenuation factor in the complex wavenumber. The first term in Eq. (3.10) describes the average pattern of the cross-spectrum and the second term indicates the small-scale fluctuations due to intermodal interference (Zhou *et al.*, 2004). Once the mode shapes and corresponding wavenumbers have been determined, either computationally or analytically by a simplifying method such as the effective depth approximation (Chapman *et al.*, 1989), the vertical coherence for the Pekeris waveguide can be calculated by inserting Eqs. (3.9) and (3.10) into (3.8).

3.3.3 3-D Computational Propagation Modelling

Computational models of sound propagation may also be used to compute the vertical coherence. In this study, a cylindrical 3-D PE code and a 3-D ray tracing code are used to compute the field. Sound propagation models employing the PE method have been widely used to compute transmission loss in environments with spatial variation in sound speed and bathymetry (Lin et al., 2015; Heaney and Campbell,2016). Provided the range step and depth grid resolution of the model are fine enough, the 3-D PE model can resolve the frequency-dependent phase differences on closely spaced vertical receivers to accurately compute the vertical coherence for individual and distributed sources (Barclay and Lin, 2019). A 3-D PE model using the split-step Fourier algorithm with a wide-angle PE approximation was used for the simulation (Lin *et al.*, 2013). The model solves the reduced form of the Helmholtz wave equation and returns the complex pressure field, in a cylindrical coordinate system, from which the vertical coherence may be directly computed using Eq. (3.8).

Additionally a 3-D ray tracing model (BELLHOP3D), which is an extension of the standard BELLHOP ray-based sound propagation model, was used for simulation in this study (Porter, 2011; Porter, 2016). The model solves 3-D eikonal and transport equations and includes a bathymetry and varying sound speed profile that allows rays to refract in all three dimensions. This

beam tracing model can be used for high frequencies or for broadband applications with useful outputs including the complex pressure field and transmission loss, eigenrays, and ray arrival times (Porter, 2019). From the modelled pressure field, the vertical coherence may be directly computed using Eq. (3.8). At higher frequencies, the 3-D PE model becomes computationally more expensive as the model grid resolution scales as a function of wavelength. In these instances, a suitable choice was to use BELLHOP3D for the computation of complex pressure and vertical coherence.

3.4 Results and Discussions

From the thirteen observations of close-range ship passages, three typical patterns in the vertical coherence were identified. In a few instances, vessel loitering behavior was seen, where a ship spent several hours near and around the hydrophone array. However, the majority of observations had a parabolic pattern in the coherogram associated with a vessel with constant bearing and speed. Lastly, in select parabolic pattern observations, anomalous artefacts in the vertical coherence were observed and hypothesized to be produced by in-plane and 3-D propagation effects due to the receiver array's proximity to the Alvin canyon. The results discussed below are limited to the last two cases and a procedure for estimating both range and bearing from the vertical coherence is demonstrated. In the first case, AIS data was available to validate the results of the inversion.

3.4.1 Range Estimation

Figure 3.2(a) shows the spectrogram of a close-range ship passing by the receiver array where the striations due to image interference are faintly visible at frequencies below 1 kHz but

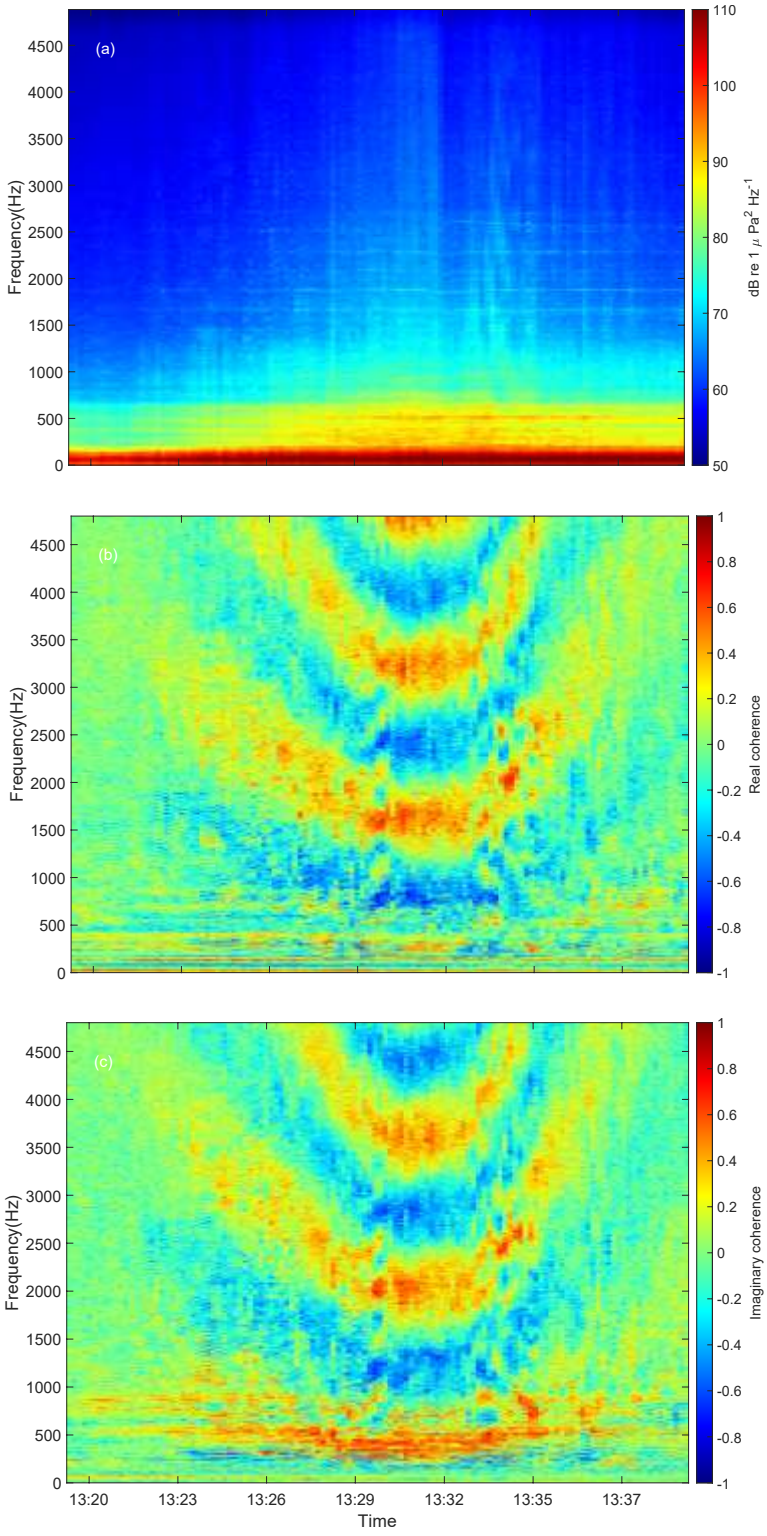

Figure 3.2: The (a) measured spectrogram, (b) the real and (c) imaginary coherogram for a close-range ship passing.

disappear at higher frequencies in the presence of wind-generated noise. Other than broadband signals, the spectrogram also shows the presence of strong tones at low frequencies that effectively mask any broadband interference pattern near the CPA. The coherence between the signals received at the hydrophones at 211 and 220.5 m depth (spacing 9.5 m) was calculated, and the real and imaginary parts are shown in Figures 3.2(b) and 3.2(c) respectively. As the ship passes by the receivers, a parabolic shaped phase interference pattern is formed in the spectrogram due to the interaction between direct waves and its reflection from the waveguide boundaries, suggesting that the ship was moving at a constant speed following a straight course. In the case of the coherogram, the interference pattern is created by path length differences between the source and the two hydrophones for all arrivals. Compared to the spectrogram in Figure 3.2a, the presence of phase interference at high-frequencies is easily detectable in the coherogram. An additional advantage of coherence is both broad and narrow band sources contribute to the fringing pattern equally due to the normalized nature of the coherence.

To estimate the vessel's range, a replica field was created for an axially symmetric, isovelocity water column over a fluid half-space using the Pekeris waveguide model. The water column sound speed ($c_w = 1494\ m/s$) and density ($\rho_w = 1024\ kg/m^3$) were obtained from temperature measurements at the receiver position. The compressional sound speed, attenuation, and density values of $c_b = 1620\frac{m}{s}$, $\alpha_b = 0.9\ dB/\lambda$ and $\rho_b = 1900\frac{kg}{m^3}$ were used to represent the half-space. The source depth was fixed at 10 m and the frequency range of the broadband source was given a bandwidth of 100 Hz to 3 kHz, with replicas computed in 20 Hz intervals. The pressure field and the CSD were computed for 20 m range increments over the domain from 0 to 5 km using Eqs. (3.9) and (3.10), and the replica field for the vertical coherence was computed using Eq. (3.8). A brute-force optimization method was used to find the range of the source based on the mismatch

between the measured coherence and the replica fields for all possible ranges. The best-fit between the model and data was determined by minimizing the value of root mean square (RMS) error over the bandwidth computed as

$$\xi(r) = \frac{1}{N}\sqrt{\sum_{i=1}^{N}[\Gamma_{12}^{data}(\omega_i) - \Gamma_{12}^{model}(\omega_i, r)]^2}\,, \tag{3.11}$$

where N is the total number of frequency intervals, and Γ_{12}^{model} and Γ_{12}^{data} are the simulated and measured coherence respectively.

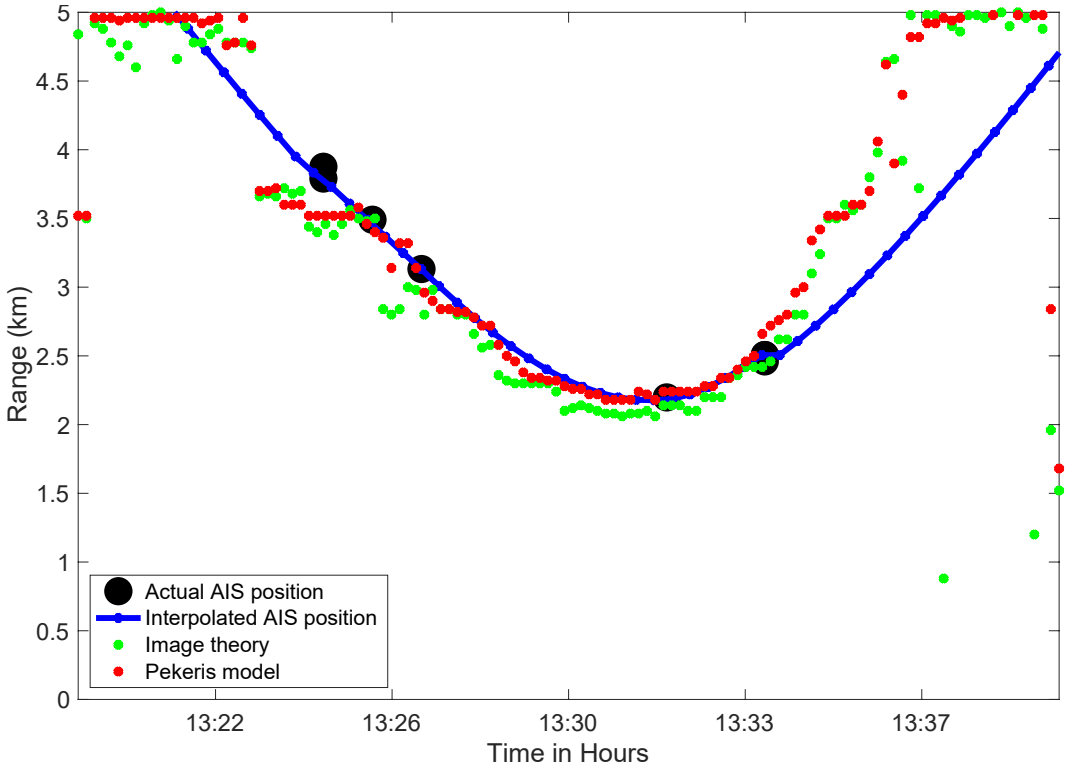

Figure 3.3: The estimated vessel range using image source model (green dots), Pekeris model (red dots), actual AIS position of the ship (black dots) and the interpolated AIS data (blue line).

The horizontal range of the ship estimated from the Pekeris model-data inversion is given in Figure 3.3 by the red dots. The inversion procedure was repeated for the image source model in the homogeneous half-space using Eqs. (3.5), (3.6), (3.8) and (3.11), where the green dots in

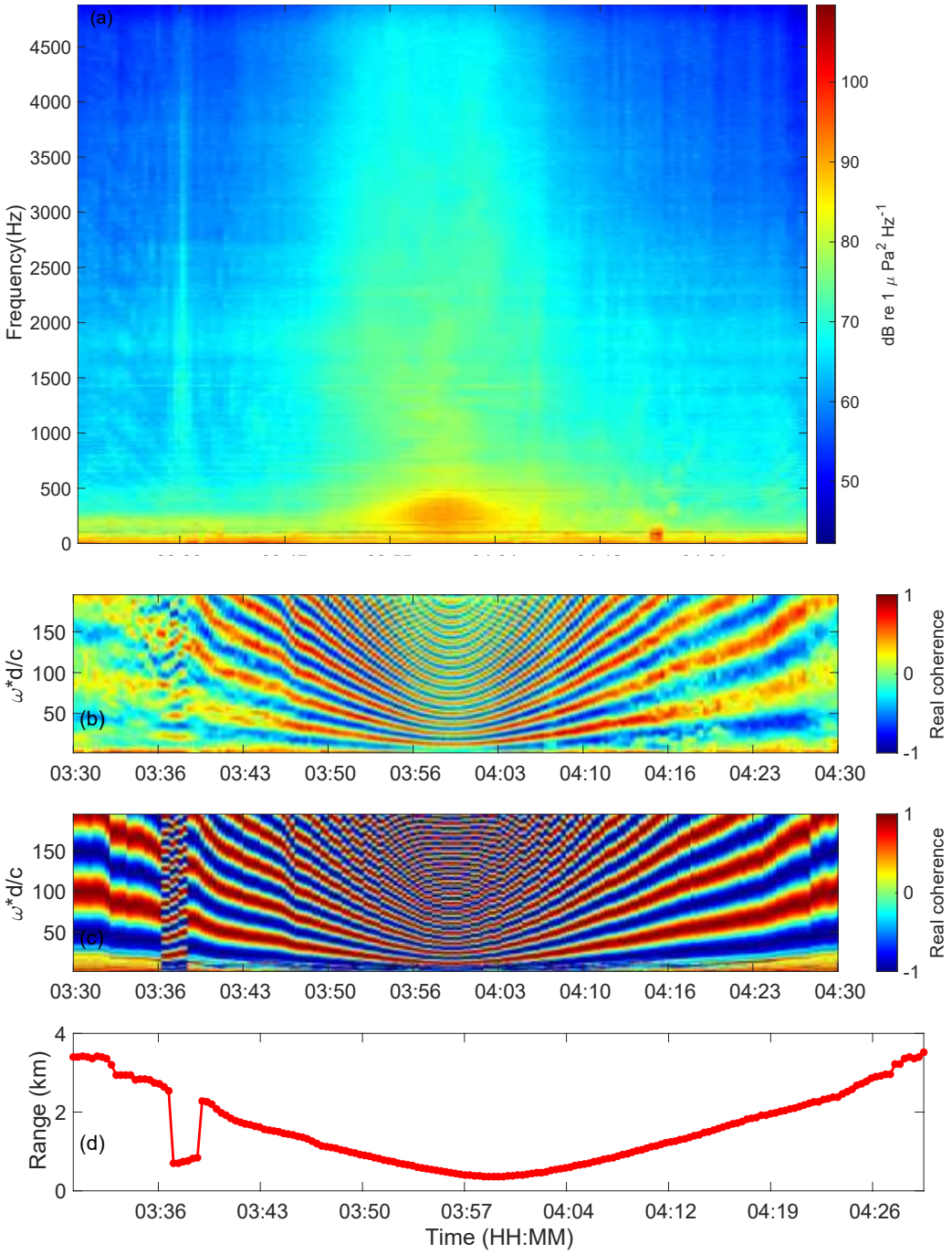

Figure 3.4: The (a) measured PSD, the real part of (b) measured and (c) best fit coherence, and (d) the estimated range for a second close-range ship passing.

Figure 3.3 are the estimated ranges. The Pekeris waveguide and homogeneous waveguides give similar range estimates and the CPA for the ship passing was found to be 2180 m. The inverted

range estimates indicate that the propagation conditions are such that the inversion is primarily sensitive to the direct and surface reflected arrivals and that, at least under the range independent model assumption, bottom reflected energy plays a secondary role. The black dots are the actual AIS position of the ship, and the blue line is the track generated by interpolating adjacent AIS points, assuming the vessel holds a constant bearing and speed. The agreement between the estimated range and AIS position is good, and the inversions begins to fail when the background noise masks the vessel's signature, at a range of 5 km. Some disagreement between the model and data occurs during the vessel's departure and is caused either by the coarse spatial resolution of the AIS data or by the lack of range-dependent bathymetry in the simple models.

Figure 3.4 shows the PSD, the real component of the measured and best fit vertical coherence, and the corresponding range estimated for a second close-range ship passing using the Pekeris model. Strikingly, Figure 3.4(d) shows a sudden drop in the horizontal range estimate at ~ 3.35 h, or at an approximate range of 2.5 km. The sudden change is causally impossible given the course and speed of the vessel. Similarly, an increase in intensity in the spectrogram in Figure 3.4(a) and a corresponding deviation in striation pattern in the coherogram are noticeable in Figure 3.4(b) and (c) at the time when the inversion algorithm fails. The broadband noise level of the ship passing data shows an increase of 5 dB during that period. The hypothesized explanation for this rapid vessel noise intensification is a combination of favorable in-plane bathymetric reflection geometry and 3-D sound focusing along the canyon axis by horizontal (out-of-plane) propagation.

The rapidly changing bathymetry near the submarine canyon can cause horizontal refraction and focus of sound along certain bearings. The horizontal refraction can cause a change in the arrival angle of signals received at the sensors, which results in a confounding interference pattern in the vertical coherence and a discontinuous striation pattern in the coherogram. The simplified

range-independent 2-D model used for source-receiver distance estimation is inadequate to represent both the in-plane and out-of-plane propagation effects caused by the canyon's bathymetry, resulting in the failure of the inversion algorithms.

A 3-D sound propagation model can be used to generate a realistic field in this type of environment. Furthermore, the azimuthal variability of the real bathymetry with respect to the receiver can be exploited to localize the vessel in both range and bearing, despite the sensor's omni-directional sensitivity. The idealized case of a ship passing over a Gaussian canyon will be first demonstrated. Then, the data presented in Figure 3.4 will be reinterpreted by replacing the simple analytical models used to compute the replica field of vertical coherence with a 3-D computational propagation model that incorporates a realistic estimate of the bathymetry.

3.4.2 Horizontal Refraction - Gaussian Canyon Case

In this section, the effect of horizontal sound focusing on coherence pattern is analyzed by generating a simulated pressure field for a moving source in an idealized Gaussian canyon bathymetry (Canyon bathymetry carry the shape of a Gaussian function). The 3-D PE model implemented in the cylindrical coordinate system was used for the simulation. Despite the computational expense of the cylindrical 3-D PE model, it provides the full azimuthal range compared to available cartesian 3-D PE models (Lin et al, 2013). Bathymetry was the only spatially-varying parameter considered in the simulation so as to isolate its influence on the vertical coherence pattern. In the Gaussian canyon model, the bathymetry is longitudinally invariant in the *x* direction and is dependent on across canyon range given by

$$H(y) = Ce^{-(y/C)^2} + B \tag{3.12}$$

where *C* is the maximum depth of the canyon and *B* is the asymptotic water depth away from the canyon.

The propagation environment considered a flat sea surface and an isovelocity water column over a homogeneous fluid half-space. The parameters used for the water column and seabed sediment properties in this 3-D simulation were the same as that used in the Pekeris waveguide described above. The ideal Gaussian canyon bathymetry was computed with B = 350 m and C = 450 m and is shown in Figure 3.5(a).

The principle of reciprocity is invoked to simplify the computation. The pressure field in this idealized 3-D environment is generated at a depth of 10 m out to a maximum range of 3.5 km in all directions from a point source placed at the origin, on the canyon's axis. The source depth is 211 m and the transmission frequency is 250 Hz. By the principle of reciprocity, the computed complex pressure field represents the received signal at the origin for all source positions in the horizontal plane, where the corresponding TL is shown in Figure 3.5(b). The increase in acoustic intensity along the axis of the canyon due to horizontal focusing of sound caused by the canyon's bathymetry is evident in Figure 3.5(b).

The computational cost of 3-D PE model at higher frequencies is large due to the zero-padding technique used to maintain the model resolution in cylindrical coordinates. Repeating the narrowband calculation of coherence for two vertical receivers in the frequency domain over the desired bandwidth can be prohibitively time-consuming, as the radial grid resolution increases with frequency. An alternative is to compute coherence as a function of dimensionless frequency ($\bar{\omega} = \omega d/c$) for a single frequency on an array of receivers, assuming the sound field is well described as a superposition of plane waves over the length of the array. For this simulation, an array of 60 sources with 1 m spacing spanning the water column from 211 m to 271 m were used to generate the acoustic fields at 250 Hz necessary to compute the wideband coherence. A

coherence map was generated in the horizontal plane by taking the first sensor at 211 m as the reference. The simulated coherence was a function of dimensionless frequency $(\bar{\omega})$, bearing (θ) and range (r).

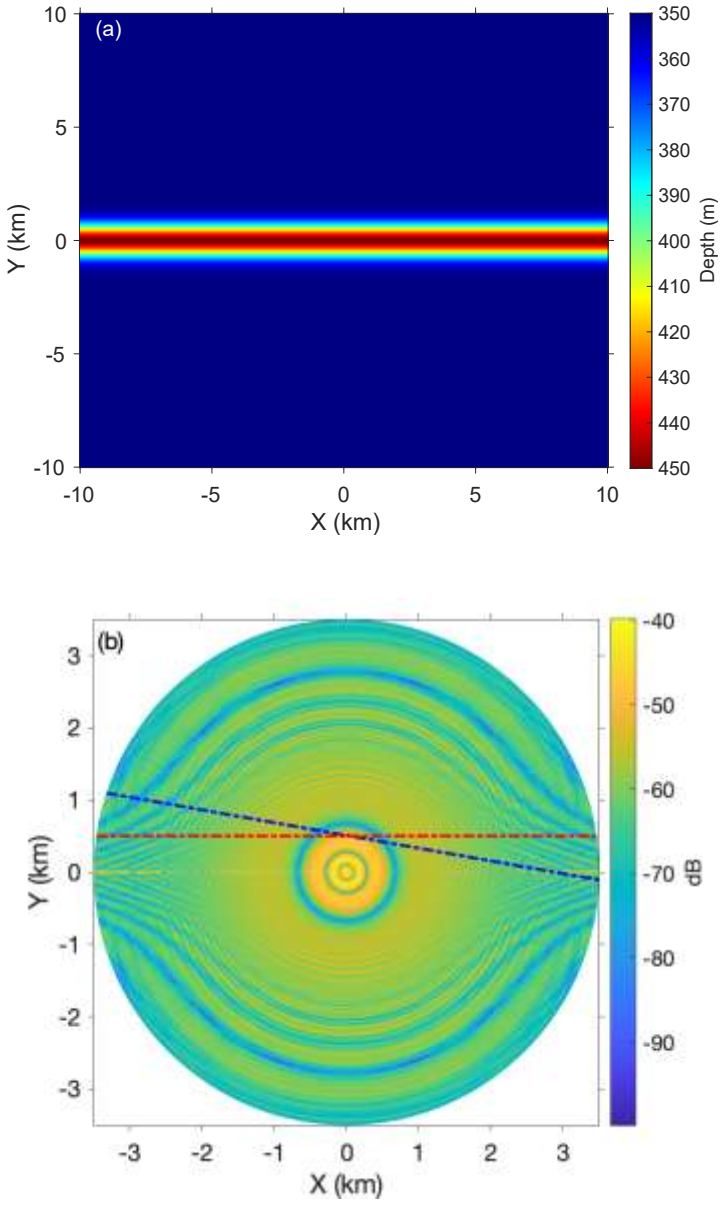

Figure 3.5: The (a) idealized Gaussian canyon bathymetry and (b) the TL at 10m for a receiver placed at 211m depth over the center of the canyon. Red and blue dashed lines are the parallel and oblique vessel tracks with respect to the canyon axis.

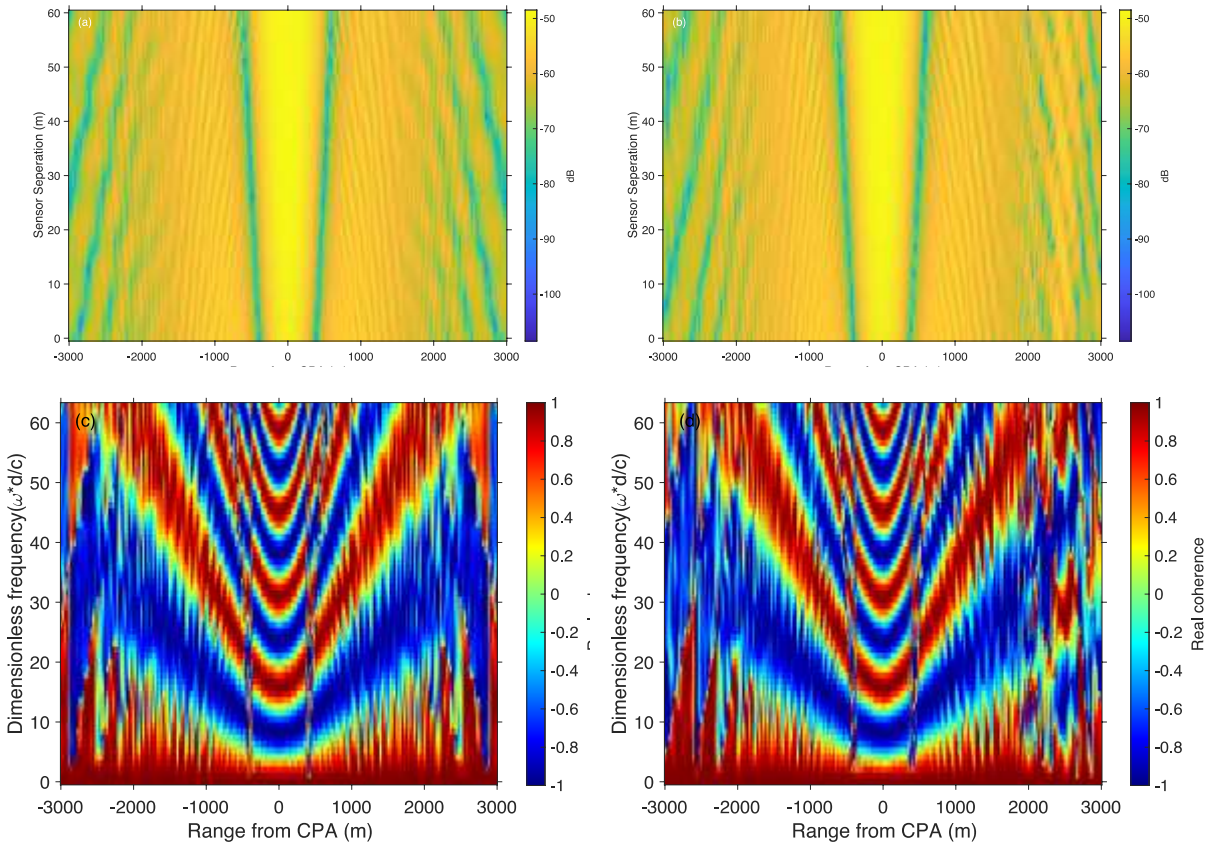

Figure 3.6: The TL as a function of range and sensor separation for the (a) parallel track and (b) oblique track, and the real part of simulated coherence as a function of range and dimensionless frequency for the (c) the parallel track and (d) the oblique track.

To study the effect of bathymetry on the vertical coherence, a pair of simulated vessels travelling along two bearing angles were chosen, each passing with the same closest point of approach (CPA). The first track was parallel to the canyon axis and passes through the CPA (300 m) along the 90° bearing (red dashed line in Figure 3.5(b) while the bearing of the second track was along the 80° bearing through the same CPA and passes the axis of the canyon obliquely (blue dashed line in Figure 3.5(b)).

The TL as a function of horizontal range and sensor separation for the two tracks are shown in Figures 3.6(a) and 3.6(b) respectively. The TL for the parallel track shows total symmetry on either

direction from the CPA, reflecting the symmetry of the bathymetry for the approach and departure paths, while the oblique track shows an increase in the intensity of around 10 dB at 2.5 km on departure, where the source crosses the axis of the canyon. The horizontal focusing of sound guided by the bathymetry of the canyon causes this increase in intensity. The real part of simulated coherograms for the parallel and oblique bearing angles are shown in Figures 3.6(c) and 3.6(d) respectively. Similar to the TL result, the parallel track generates perfect symmetry in the real part of coherence on either side from the CPA while a difference in the fringing pattern is observed on departure for the oblique track, beginning at a range of 2 km. The effect on the power and vertical coherence observed in this simulation is similar to the fringing pattern variation seen in the measured coherogram data collected near Alvin Canyon, suggesting that a careful data-model comparison made using a 3-D propagation model can exploit bathymetric features to estimate the bearing and range of passing vessels.

3.4.3 Bearing Estimation - Alvin Canyon

This section describes the method to estimate the range and bearing of the ship, passing the receive array shown in Figure 3.4 using the measured vertical coherence. First, the range of the vessel at the CPA was estimated using the 2-D Pekeris waveguide model described in Sec. 3.4.1 and the velocity (speed and heading) of the vessel was assumed to be constant. A library of model coherograms was computed for all possible vessel headings with a bearing resolution of 5°, each passing by the receive array tangent to the circle formed by the locus of possible CPAs. The model and data were compared by computing the mean RMS fit error, ξ for each possible vessel track, given by Eq (3.11).

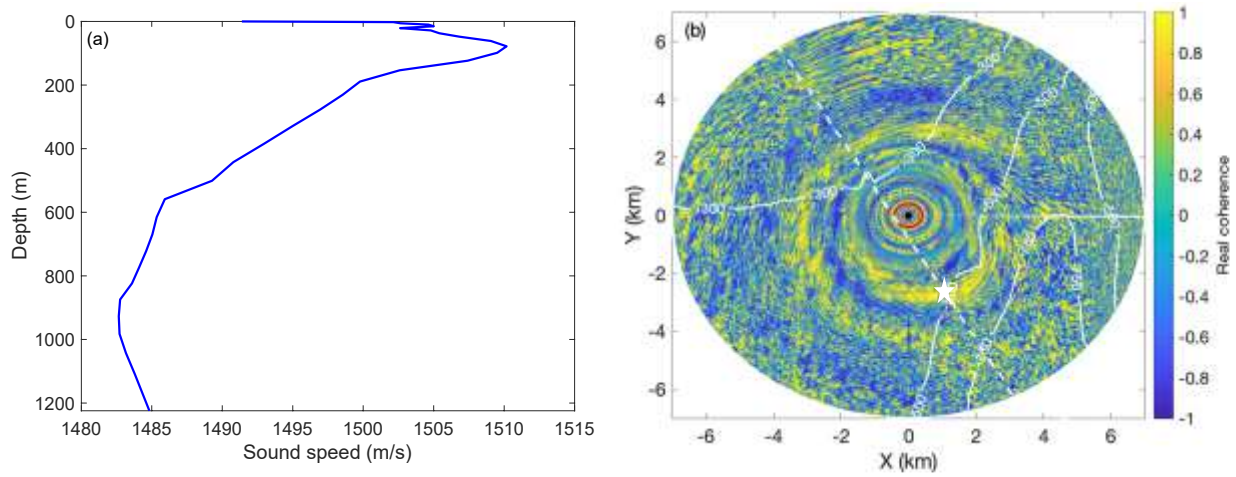

Figure 3.7: The (a) water column sound speed profile, (b) The simulated coherence map at 1200Hz using BELLHO3D, along with the vessel track (white dashed line) plotted over bathymetry at a bearing of 210°, where the white star indicates the position of the source track where the coherogram asymmetry occurs.

A sound speed profile from a data assimilated ocean circulation model output at a grid point near the SHRU location was used as input to the propagation model (Unidata, 2016) and is shown in Figure 3.7(a). The assumption of a flat sea surface and values of the seabed geoacoustic properties used in BELLHOP3D were the same as that used for the Pekeris waveguide described above. The acoustic field at 10 m depth in the horizontal plane was calculated by keeping the two acoustic sources at 211 m and 220.5 m respectively, representing the two depths of the SHRU receivers. The frequency range used in the simulation was from 100 Hz to 1.5 kHz at 30 Hz intervals and the maximum horizontal range was 7 km.

The vertical coherence map as function of frequency, range and bearing was created for Alvin Canyon. The coherence map, or acoustic fingerprint, at 1200 Hz is shown in Figure 3.7(b). The map shows the variation in the coherence pattern along the axis of the canyon relative to the flat bathymetric region, and the asymmetry in the real component of the vertical coherence reflecting the asymmetry of the bathymetry.

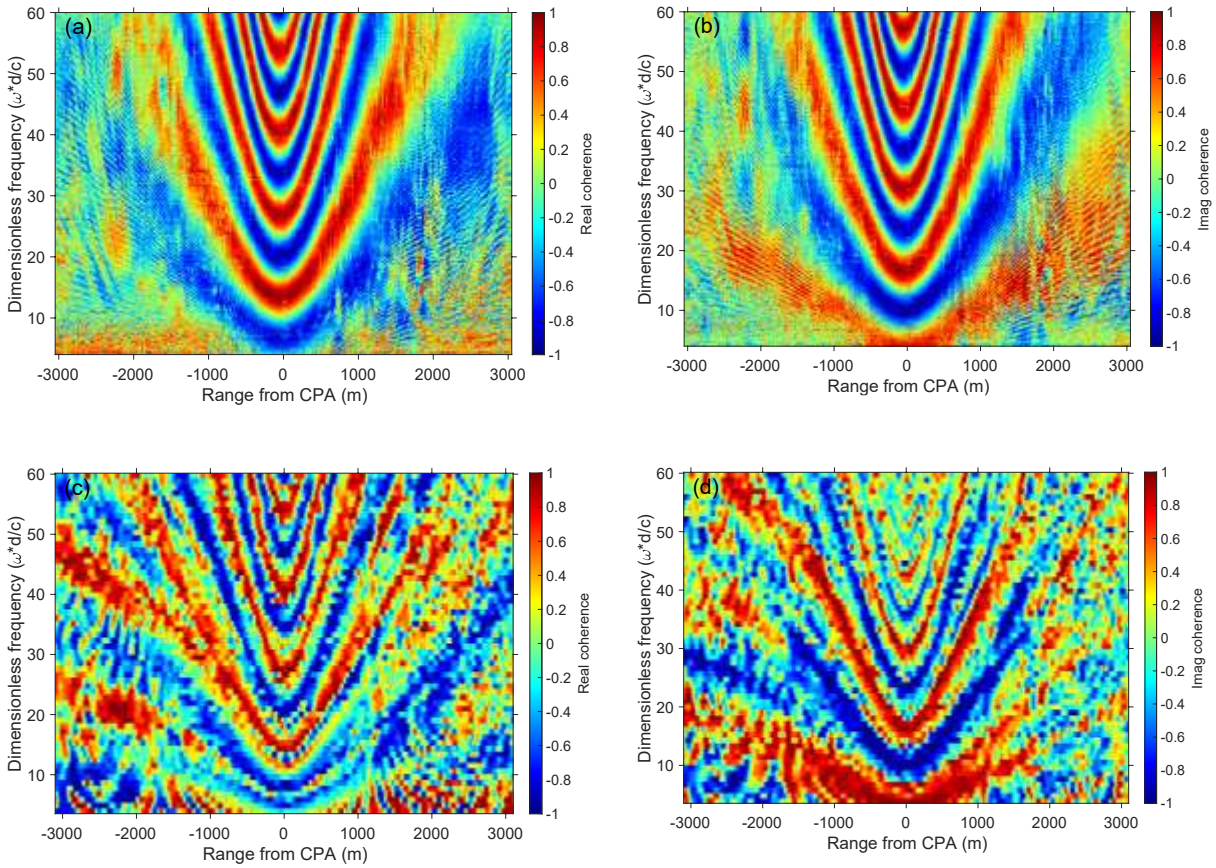

Figure 3.8: The (a) real and (b) imaginary part of the measured vertical coherence, and the (c) real and (d) imaginary part of simulated best fit at 210° bearing as a function of dimensionless frequency($\bar{\omega}$) and range.

The vessel track with a bearing angle of 210° provided the best match between the modelled result and observations as is shown in Figure 3.7(b). The real and imaginary parts of the field coherence and the model output at 210° as a function of dimensionless frequency and range are shown in Figures 3.8(a), 3.8(b) and 3.8(c), 3.8(d) respectively. The asymmetry in the fringing pattern due to bathymetry is visible in the model result at the dimensionless frequency of 20 and 45 at a range of -2.5 km (on approach). This feature in the coherogram corresponds to the moment indicated by the white star in Figure 3.7(b), where the acoustic fingerprint shows a region of strong constructive interference between the two receivers generated by the canyon's bathymetry.

In the idealized Gaussian canyon case, the horizontal focusing along the canyon's axis led to features in both the spectrogram and coherogram as a source passed over it. In the realistic Alvin Canyon case, the asymmetry in the received power and fringing coherence pattern is primarily due to the up and across slope 3-D propagation effect exemplified in similar idealized wedge-shaped environments (Buckingham, 1987). The realistic local bathymetry of the canyon plays a further effect in causing asymmetries in the constructive and destructive interference pattern between the receivers, as can be seen in the acoustic fingerprint shown in Fig 3.7(b).

3.5 Conclusions

This chapter has presented a method to determine the range and bearing of a moving broadband acoustic source using the coherence measured on two omni-directional, vertically-separated hydrophones. The theoretical results presented in this chapter establish a simple relationship for broadband signal coherence between frequency, source range, and receiver hydrophone vertical separation. Ambient noise data recorded near Alvin submarine canyon containing multiple ship passes by a vertical array were used for the analysis. Time series of PSD and coherence revealed the presence of Lloyd's mirror effect when ships passed the receivers at close-ranges. The measurements and the equations for the cross-spectrum in a homogeneous half-space and Pekeris waveguide were used to estimate the range of a vessel, which was verified against the AIS data.

In another ship pass measurement, the horizontal refraction of sound caused by the real bathymetry was hypothesized to cause an unexpected increase in intensity and a corresponding fringing pattern change in the coherogram. Simulation results in an idealized Gaussian canyon environment clearly showed the influence of bathymetry on the pressure field and coherence for a source with constant speed and heading. In the measurements, it was shown that similar asymmetries in spectrograms and coherograms could be explained using 3-D modelling. By

exploiting the rapidly varying Alvin Canyon bathymetry, the vessel bearing and range relative to the pair of vertically spaced omni-directional receivers were obtained. In the case discussed, an increase in received intensity and change in the coherence fringing pattern were primarily due to the sloped canyon walls which lead to steep upslope propagation on approach, and gentle downslope propagation on departure.

Some of the limitations associated with the present analysis are briefly addressed here. The 2-D model used to estimate the range of the vessel considered a constant water column sound speed. Refraction of sound caused by the water column sound speed profile will introduce variation in the coherence pattern especially at higher frequencies and farther ranges from the CPA. Future work will include investigating the influence of the refracting water column on coherence-based range estimates. In both the 2-D and 3-D model simulations the seabed was considered as a fluid half-space. The sub-bottom layering and geoacoustic properties is expected to influence the coherogram at low frequencies (Barclay *et al*, 2019). However, the direct and surface reflected arrivals are the main contributors to the sound field in the measured data. Thus, the representation of the bottom as a half-space was appropriate in modelling the coherence pattern for this particular environment.

Despite these limitations, a reliable technique has been introduced in this study to estimate the range and bearing of a moving vessel. In coherence-based range estimation, the entire frequency range, only limited by the sampling frequency of the hydrophones, can be used for processing. Coherogram results are insensitive to SNR and details of the ship's signature compared to PSD-based range estimates (Wilmut et al, 2007). The normalized cross-spectrum highlights broad and narrowband coherent signals and discards incoherent noise received at two points, which is especially observed at higher frequencies (shorter wavelengths relative to hydrophone spacing)

where the wind-wave generated noise coherence is low. Thus, successful inversion can be performed using a wider frequency range. Further, it is shown that 3-D localization using a pair of vertically-separated omni-directional sensors is possible by exploiting 3-D bathymetric effects in continental shelf and slope environments.

CHAPTER 4

MAPPING OF SURFACE-GENERATED NOISE COHERENCE FOR BETTER SIGNAL DETECTION

4.1 Introduction

Signal detection in a poorly characterized and noisy ocean environment is a challenging problem. Hydrophone arrays are commonly used to improve signal detection against background ambient noise. They are also commonly used in active and passive SONAR, TL experiments, seismic operations, and passive acoustic monitoring. The performance of an array is determined by its Array Gain (AG) which is the improvement in SNR of the array relative to a single sensor, or the difference between Signal Gain (SG) and Noise Gain (NG) in dB (Urick, 1967). The response of the array to noise is expressed in NG which depends on the spatial characteristics of ambient noise field (Buckingham, 1981). Thus, the spatial coherence of ambient noise is directly related to the AG.

Analysis of the space-time correlation property of ambient noise received on an array returns the spatial coherence of the noise field. It is a normalized quantity which depends on the sound speed profile, bathymetry, seabed acoustic properties and the type and physical extent of the noise source. The prediction of noise spatial coherence requires detailed knowledge of the properties of the sound propagation environment. Most of the measurement and modelling studies of spatial coherence are location specific and used as a tool for noise-based inversion of the ocean environment (Buckingham and Jones, 1987; Carbone *et al*, 1998; Muzi *et al*, 2016; Shajahan *et al*, 2020). Knowledge of the mesoscale spatial variation of vertical coherence and the relative

influence of environmental factors (seabed geoacoustic parameters, sound speed depth profile) is required for the design of element spacing of arrays in passive and active acoustic systems.

The two familiar models of spatial coherence are the isotropic model and the surface noise models developed by Cron and Sherman (1962). The isotropic model considers the noise field as statistically independent plane waves propagating in all directions uniformly while the surface noise model assumes noise sources to be distributed on an infinite plane just below the surface of the ocean. Although the surface noise model agrees well with deep-water measurements (Barclay and Buckingham, 2013a; Barclay and Buckingham, 2013b), the model does not include sound propagation characteristics such as refraction, attenuation, and boundary reflections to derive a simple analytical solution.

The isotropic and surface noise models have difficulty modelling the continental shelf and slope regions since the models do not consider environmental complexity. The sound speed profile, bathymetry and sediment type can affect noise propagation causing anisotropy in the noise field and change in spatial coherence. Previous studies reported the performance of a vertical line array in shallow water due to wind-induced ambient noise under varying environmental conditions (Buckingham,1979; Hamson, 1980). Kuperman and Ingenito (1980) introduced a normal mode noise model for spatial coherence in a stratified media based on wave theory by assuming noise sources as monopoles distributed at the ocean surface. Buckingham (1980) similarly presented an analytical solution for the vertical coherence of surface-generated noise applicable in shallow water. A simple closed-form solution for vertical coherence based on ray theory was developed by Harrison (1996) and found to be very effective in noise-based inversion applications.

In this chapter, a map of the vertical coherence of ambient noise is generated and its dependence on environmental factors is analyzed on spatial scales greater than 100 km^2. The study

region was around Alvin Canyon, south of Martha's Vineyard, Massachusetts. A PE sound propagation model based on reciprocity theory was used for the simulation of the noise field (Barclay and Lin, 2019). The simulation results provide a quantitative estimate of NG relative to different sound propagation conditions and model configurations. The chapter is organized as follows: Section 4.2 presents the basic theory of spatial coherence and AG. Section 4.3 shows the method for modelling ambient noise using a 3-D PE model and the description of the environmental inputs used in the simulation. In section 4.4, describes the simulation results of vertical coherence and noise gain for different test cases. Finally, section 4.5 presents the conclusions from the analysis.

4.2 Theory - Array Gain and Vertical Coherence

The array gain is determined using the following simple relationship,

$$AG = SG - NG \tag{4.1}$$

where SG, is the signal gain and NG, is the noise gain, measured in dB. The AG of a linear array with discrete hydrophones can be expressed in terms of cross-correlation coefficient as

$$AG = 10 \log \frac{\sum_m \sum_n (\Gamma_S)_{mn}}{\sum_m \sum_n (\Gamma_N)_{mn}} \tag{4.2}$$

where Γ_S is the correlation coefficient of the signal and Γ_N is the correlation coefficient of the noise field. The hydrophone positions in the array are given by the indices m and n. When the noise is incoherent and the signal has a unit correlation between array elements, the array performance increases logarithmically with the number of hydrophones. When the noise is partially coherent, the array performance may degrade depending on the coherence of noise signals. The overall array performance depends on the degree of coherence existing between noise signals received at different hydrophones across the array.

Two common reference models of spatial coherence are used to describe noise coherence with closed form expressions. The isotropic model considers plane waves uniformly distributed over all directions. The normalized correlation function for the isotropic noise model can be expressed as

$$\Gamma_{iso} = \frac{\sin kd}{kd}, \tag{4.3}$$

where k is the wavenumber and d is the spacing between array elements, independent of the orientation. The surface noise model developed by Cron-Sherman is more realistic compared to the isotropic noise model and primarily used for deep-water applications. The model assumes only downward travelling noise in a semi-infinite, non-attenuating, homogeneous ocean with azimuthal symmetry. Based on the above assumptions, the vertical noise coherence function can be expressed as

$$\Gamma_{CS} = 2\left[\frac{\sin kd}{kd} + \frac{\cos kd - 1}{(kd)^2}\right] + 2i\left[\frac{\cos kd}{kd} - \frac{\sin kd}{(kd)^2}\right]. \tag{4.4}$$

According to Cox (1973), in a homogeneous noise field, the real part of coherence for surface-generated noise represents the symmetry in the noise field about the horizontal while the imaginary part represents the asymmetry. The real and imaginary components of coherence for an isotropic noise field as a function of the ratio between hydrophone spacing and wavelength (d/λ) is given as a dashed line in Figure 4.1. The real part of coherence falls to zero at half-wavelength spacings ($\lambda/2$). If we use isotropic assumption in Eq. 4.2 with $\lambda/2$ spacing for an array, AG increases logarithmically with the number of hydrophones. The imaginary part of the isotropic noise model is zero due to the symmetry in the noise field.

The real and imaginary component of coherence for the Cron-Sherman model are also shown in Figure 4.1 as solid line. The complex coherence function given in Eq. 4.4 shows the

anisotropic nature of noise directionality. In general, the coherence is higher for Cron-Sherman model, especially at the first $\lambda/2$ spacing. This increase in coherence may cause a degradation in the AG compared to prediction made using isotropic noise field model. Thus, the position of the first zero-crossing of the real part of coherence is a critical parameter in designing the spacing between sensors for sonar applications.

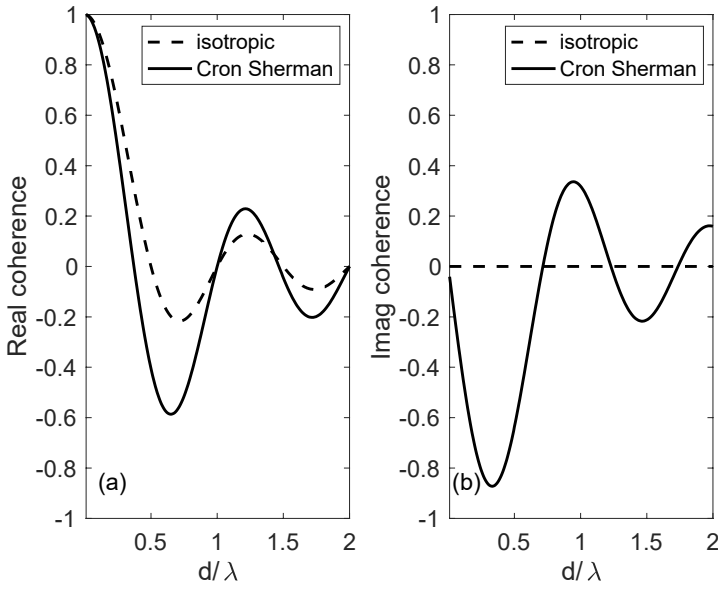

Figure 4.1: The real and imaginary coherence of isotropic (dashed line) and Cron-Sherman model (solid line)

The position of the first zero-crossing can vary depending on the sound speed profile, sediment type, bathymetry, and horizontally propagating distant sound in the measurement location (Buckingham and Jones, 1987; Carbone *et al*, 1998; Shajahan *et al*, 2020). The environmental influence on noise coherence can be analyzed by mapping the first zero-crossing on a spatial scale. The zero-crossing frequencies of spatial coherence is important in the design of hydrophone spacing in passive and active acoustic experiments. The zero- crossings also depends on the ocean environment, especially the first zero-crossing. In this work, the position of the first

zero-crossing of the Cron-Sherman model was used as a reference and the relative change from it for different cases are investigated.

4.3 Mapping Ambient Noise Vertical Coherence

4.3.1 3-D Ambient Noise Field Modelling

The ambient noise field can be considered as a superposition of pressure fields due to individual sources. Normally, for wind-generated noise, the sources are assumed to be distributed just below the surface with a specific source intensity per unit area. The analytical noise model described in chapter 2 considered a statistical distribution of individual sources and the cross-spectral density for a range-independent environment was obtained by integrating over range and azimuth. An alternate approach adapted here is to use a sound propagation model to calculate the pressure field from surface distributed sources. Parabolic approximation of the wave equation (PE model) is a convenient way to determine the acoustic field due to distant sources in a range-dependent environment (Tappert, 1974). A PE sound propagation model can include variable bathymetry, sediment type, and sound speed profile. In this case, the PE model exploits the principle of reciprocity which keeps the pressure field same even if we interchange the position of the source and receiver. The complex pressure field computed at z_s for an arbitrary source at z_1 gives the surface sensitivity for a receiver placed at z_1. Thus, in the case of wind-generated noise, the total field can be calculated by summing over all the contributions from individual sources in the horizontal plane. Based on this assumption, the noise power due to a quasi-infinite sheet of noise sources placed just below the surface at depth z_s in a cylindrical grid (r, β) can be obtained as,

$$S_{11}(\omega) = \sum_{p=-\infty}^{+\infty} \sum_{q=-\infty}^{+\infty} \langle \left| \sigma\left(r_q, \beta_p\right)^2 \right| \rangle \left| P\left(\omega, z_1, z_s, r_q, \beta_p\right) \right|^2 \Delta\beta \Delta r r_q, \qquad (4.5)$$

where $P(\omega, z_1, z_s, r_q, \beta_p)$ is the complex acoustic pressure field in the model domain. z_s is the source depth and ω is the angular frequency. $r_q = r_0 + q\Delta r_q$, is the range of the noise source and $\beta_p = p\Delta\beta$, is the bearing. $\langle\left|\sigma(r_q, \beta_p)^2\right|\rangle$ is the ensemble average of the noise source strength. $\Delta\beta\Delta r r_q$ is the cylindrical coordinate element area over which the noise sources have been averaged. The CSD can be computed by placing a second source at depth z_2 and computing

$$S_{12}(\omega) = \sum_{p=-\infty}^{+\infty}\sum_{q=-\infty}^{+\infty}\langle\left|\sigma(r_q, \beta_p)^2\right|\rangle P_1(\omega, z_1, z_s, r_q, \beta_p)P_2{}^*(\omega, z_2, z_s, r_q, \beta_p)\Delta\beta\Delta r r_q, \quad (4.6)$$

where the * denotes the complex conjugate.

A detailed description of the reciprocal PE noise model can be found in (Barclay and Lin, 2019). By keeping the sources at positions z_1 and z_2, the complex pressure field can be calculated for the model domain. The power spectrum and cross-spectrum for surface distributed noise sources can be calculated using Eqs. 4.5 and 4.6. Once the power spectrum and cross-spectrum are computed, the normalized cross-spectral density, or coherence, can be determined by

$$\Gamma_{12}(\omega) = \frac{\langle S_{12}(\omega)\rangle}{\sqrt{S_{11}(\omega)S_{22}(\omega)}}. \quad (4.7)$$

An Nx2-D and a 3-D PE model using the split-step Fourier algorithm with a wide-angle PE approximation was used to calculate the pressure field in this study (Lin *et al*, 2013; Lin *et al*, 2015). The 3-D model solves the forward propagating PE equation reduced from the Helmholtz wave equation in a cylindrical coordinate system with a one-way marching algorithm originating from the source position, allowing horizontal propagation between radial marching directions.

4.3.2 Environmental Input Parameters

The main input parameters required for the 3-D PE model are spatially varying bathymetry, vertically varying sound speed profile, and seabed sediment properties. The model domain was selected near Alvin Canyon to highlight the importance of the rapidly changing bathymetry. The

study region includes continental shelf, continental slope, and deep-water regions, and is characterized by spatial variation in sediment composition (it comprises the New England Mud

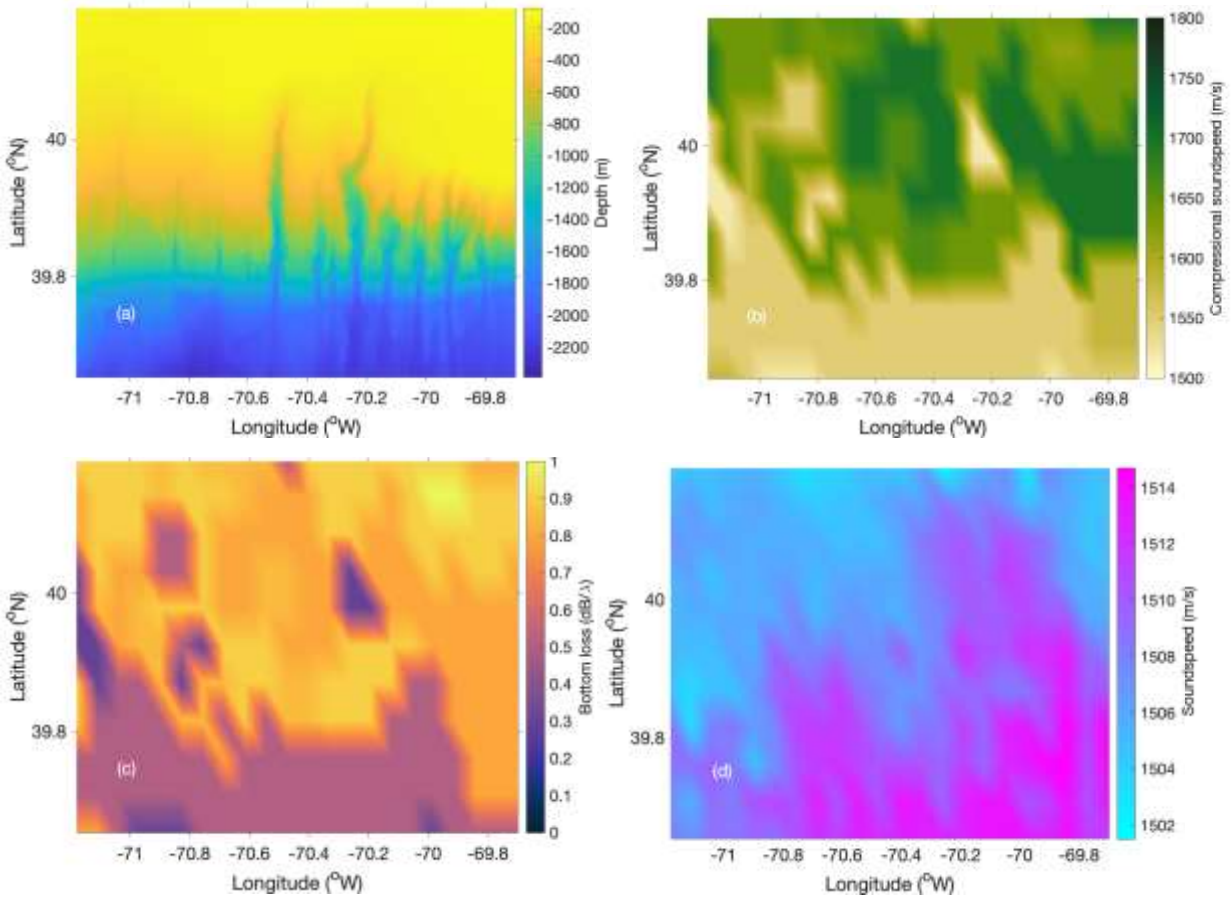

Figure 4.2: The environmental properties of the model domain (a) bathymetry (b) compressional sound speed (c) bottom loss and (d) the sound speed at 50 m depth.

Patch), and sound speed profiles. Bathymetric data were drawn from the Global Multi Resolution Topography (GMRT) database with 45 m resolution in latitude and 70 m resolution in longitude (Ryan *et al*, 2009). The bathymetry of the region is given in Figure 4.2a. The sediment type of the region was obtained from the US geological survey data base (Reid *et al*, 2005). Hamilton's (1980) sediment model for the continental slope environment was used to estimate the geoacoustic properties of each sediment sample from the database (Jensen *et al*, 2011). Compressional sound speed, density, and bottom loss were estimated and the map of compressional sound speed and

bottom loss for the study region is given in Figures 4.2b and 4.2c respectively. The environmental model assumed a planar sea surface with total internal reflection. The data assimilated Regional Ocean Modeling System (ROMS) Experimental System for Predicting Shelf and Slope Optics (ESPreSSO) model output was used to extract water temperature and salinity covering the study region (Rutgers Ocean Modeling Group). Sound speed profiles are derived from temperature and salinity using Mackenzie equation (Mackenzie, 1981). The sound speed map at 50m depth for the model domain is shown in Figure 4.2d. Below the mixed-layer, most of the grid points followed a downward refracting sound speed profile which is the characteristics of a typical winter profile of the study region.

4.3.3 Numerical Simulations

The numerical simulations were performed to understand the relative effect of various levels of environmental variability on noise coherence and array gain. Two submarine canyons were present in the study region (Alvin and Atlantis). The bathymetric variations in the model domain were significant to study the effect of horizontal refraction on noise coherence. At higher frequencies, the 3-D PE model becomes more computationally expensive as the model grid resolution scales as a function of wavelength. Thus, the simulations were performed for a single frequency of 50 Hz and a grid resolution of 6×6 km and assuming a homogeneous surface generated ambient noise field (Kuperman and Ingenito, 1980). A vertical array of 40 sources with 1 m spacing spanning the water column from 40 to 79 m were used to generate the acoustic field at each grid point for a horizontal range of 10 km and the model source level was set to be 0 dB. By invoking the principle of reciprocity, the power spectrum, cross-spectrum and coherence were computed at each grid point using Equations 4.5, 4.6, and 4.7 respectively.

The numerical simulations were carried out for four test cases with different environmental variations. These cases were chosen to study the individual effects of environmental inputs on noise coherence separately. In case 1, a 2-D PE model was used to simulate noise coherence at every one degree of bearing to generate an N×2-D noise field at each grid point. The N×2-D environment considers only the bathymetric variation in the radial direction and neglects the transverse variation of the seafloor and any resulting out-of-plane sound propagation between radials. The water column sound speed at each grid point was taken as constant for this case. The dominant component of surficial sediment in the study region was fine sand. Thus, the same geoacoustic properties were used for the seabed at each grid point with a compressional sound speed C_b =1650m/s, density ρ_b =1900kg/m^3 and attenuation α_b =0.8 dB/λ, where λ is the wavelength.

Table 1: Test cases and corresponding environmental input parameters

Case	Bathymetry	Sound speed	Geoacoustics
1	Nx2-D	constant	constant
2	3-D	constant	constant
3	3-D	SSP	constant
4	3-D	SSP	variable

Case 2 examined the bathymetry induced horizontal refraction by replacing the N×2-D model with a 3-D model with the environmental inputs being the same as in case 1. Case 3 studied the effects caused by the sound speed profile by replacing the constant sound speed in the water column with a range independent sound speed $c(z)$. In case 4, the combined effect of bathymetry, sound speed profile and sediment properties on ambient noise vertical coherence was examined. The four test cases and their respective environmental inputs are summarized in Table 1.

4.4 Results and Discussions

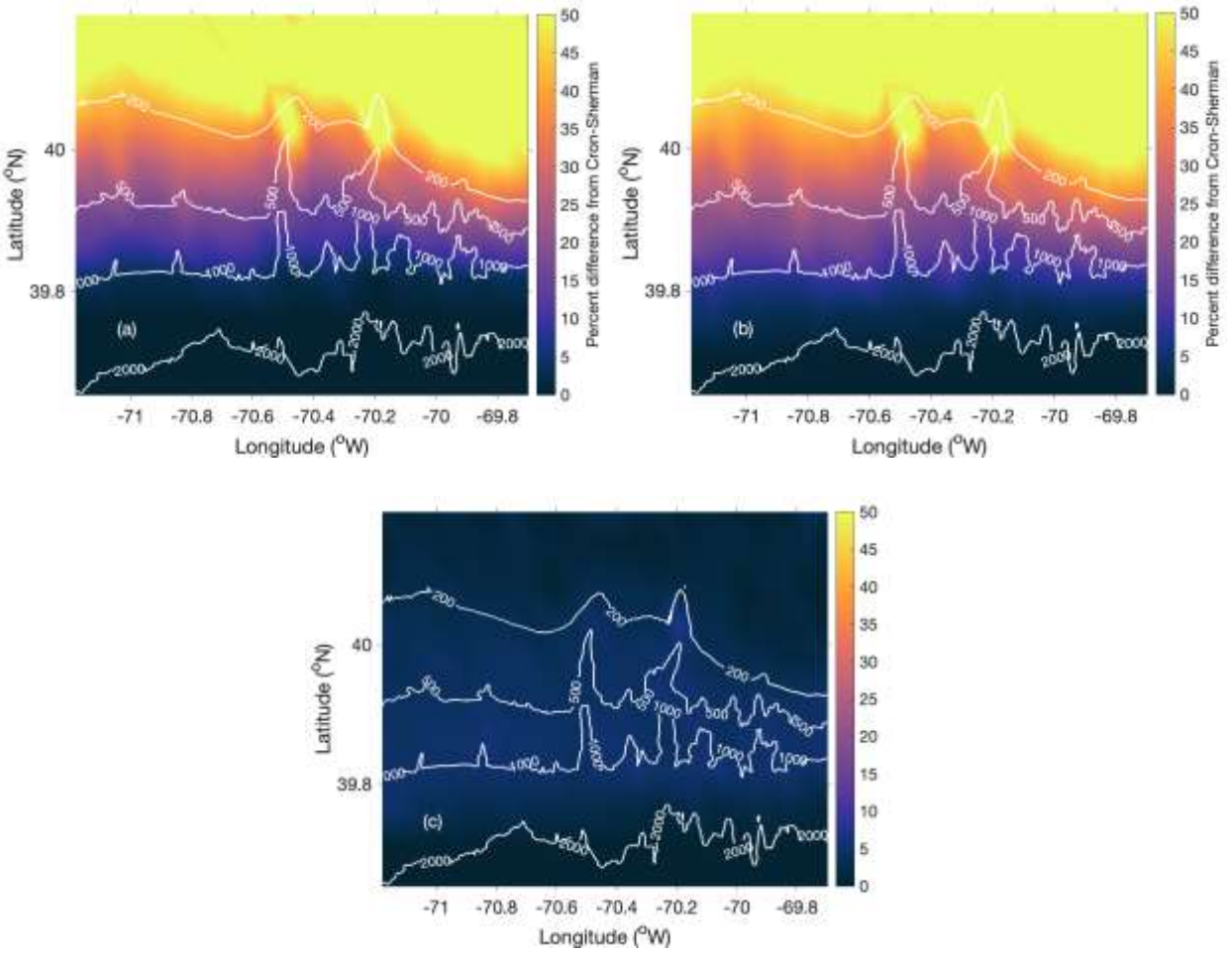

Figure 4.3: The percentage difference between the Cron-Sherman and computational vertical noise coherence model's first zero-crossing frequency for (a) case 1, (b) case 2 and (c) the difference between case 1 and 2.

The relative change in the first zero-crossing frequency from the Cron-Sherman model for cases 1 and 2 and their difference are shown in Figures 4.3a, 4.3b and 4.3c respectively. The bathymetric data of the study domain are shown as isobath contours in each coherence map. Both cases considered constant sound speed in the water column and identical sediment properties at each grid point in the model domain. Thus, this comparison solely focuses on the effect of range-dependent topography. The N×2-D simulation does not include transverse coupling of sound

energy across the vertical plane. On the other hand, the 3-D PE model incorporates sound focusing due to horizontal refraction. Examination of Figures 4.3a and 4.3b shows that the relative change for cases 1 and 2 is higher than 50 % in shallow water (< 200 m) for both cases 1 and 2. This result clearly suggests the inaccuracy of the Cron-Sherman model in representing the noise field in shallow waters. The proximity of the seabed can introduce interaction of sound with the ocean boundaries resulting in bottom reflected arrivals at the sensors. Moreover, the sandy bottom type used for the simulation may cause horizontal propagation of noise below the critical angle as a result of total internal reflection. Both these factors can contribute to the symmetry in the noise field resulting in an increase in the first zero-crossing frequency compared to the Cron-Sherman model.

The relative change approaches 0% for case 1 in regions with depth greater than 1000 m. This shows the agreement between the N×2-D simulation and the Cron-Sherman model in deep water regions. However, case 2 shows a 10 - 15% increase in zero-crossing frequency between 1000 and 2000 m while above 2000 m the coherence map agrees well with the surface noise model. The difference between case 1 and case 2, shown in Figure 4.3c, shows the importance of 3-D propagation effects in regions of variable bathymetry, especially between the 200 and 2000 m isobaths. The rapidly changing bathymetry in the continental slope regions can induce horizontal refraction and sound focusing resulting in a 10-15% difference between 2-D and 3-D modelling. The comparison revealed that the 3-D effect of bathymetry on noise coherence is only marginally significant in the study region.

The relative change in percentage from the Cron-Sherman model for case 2 and case 3 are shown in Figures 4.4a and 4.4b respectively. The constant sound speed is replaced by a sound

speed profile at each grid point in case 3. In comparison with case 2, the shallow water regions of case 3 showed a decrease in the relative change up to 30%. The first zero-crossing frequency of the deep-water regions for case 3 matches with the Cron-Sherman model result. The interaction of sound with the seabed is larger for a downward refracting sound speed profile when compared to a constant sound speed water column. As sound interacts more with the seabed, the increased bottom loss may cause asymmetry in the noise field and most of the energy remains at the surface. As a result, the relative change in shallow waters for case 3 is less compared to case 2. The difference between case 2 and case 3 is shown in Figure 4.4c. This analysis clearly shows the importance of an accurate sound speed profile in the simulation of the spatial characteristics of ambient noise (Barclay and Buckingham, 2013a; Barclay and Buckingham, 2014).

In case 4, all the three spatially varying properties (bathymetry, sound speed profile and sediment properties) were used to simulate the spatial coherence at each grid point and the noise coherence map was generated using the 3-D propagation model. The noise coherence map of case 4 is similar to that of case 3 except for some regions in shallow water where the relative change in case 4 falls to zero as shown in Figure 4.5b. The map of the sediment compressional sound speed given in Figure 4.2b indicates that the sediment composition in those regions was clayey silt. Bottom reflection loss mainly depends on the type of sediment. Clayey silt more effectively absorbs the sound energy compared to larger grained sediments. The negative gradient in sound speed profile in shallow water also enhances the interaction with the bottom. As a result, the noise field is dominated by downward travelling sound similar to the assumption of the Cron-Sherman model. Figure 4.5c shows that the bottom type can cause a difference of up to 40 % in the noise coherence map. Identical to the other cases, the noise map for case 4 mostly follows the Cron-Sherman model and the sediment type does not affect the zero-crossing frequency in deep water.

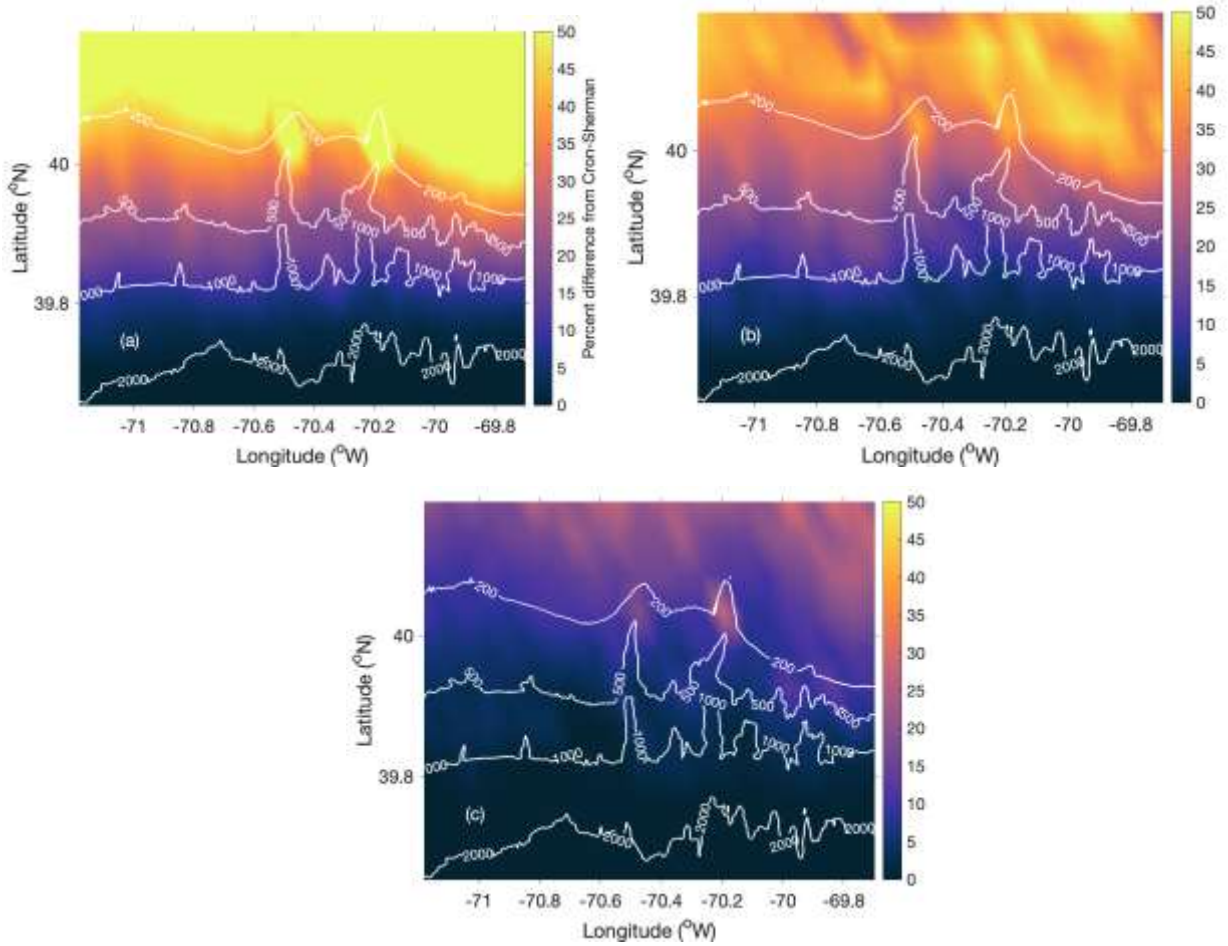

Figure 4.4: The percentage difference between the Cron-Sherman and computational vertical noise coherence model's first zero-crossing frequency for (a) case 2, (b) case 3 and (c) the difference between case 2 and 3.

The analysis shows that sediment type is the critical shallow water parameter for an accurate model of the noise field and spatial coherence (Yang and Yoo, 1997; Jensen et al, 2011).

To demonstrate the influence of spatial variation in environmental properties on signal detection, a map of NG was generated for a 10-element hydrophone array with $\lambda/8$ spacing coherently summed (with the beam steered broadside). According to Eq 4.1, a decrease in NG enhances the overall array performance, while an increase degrades the performance. NG maps were generated using the simulated vertical coherence. Two transects along the latitude as shown in Figure 4.6 were chosen to study the variation in NG from shallow water to deep-water. The first

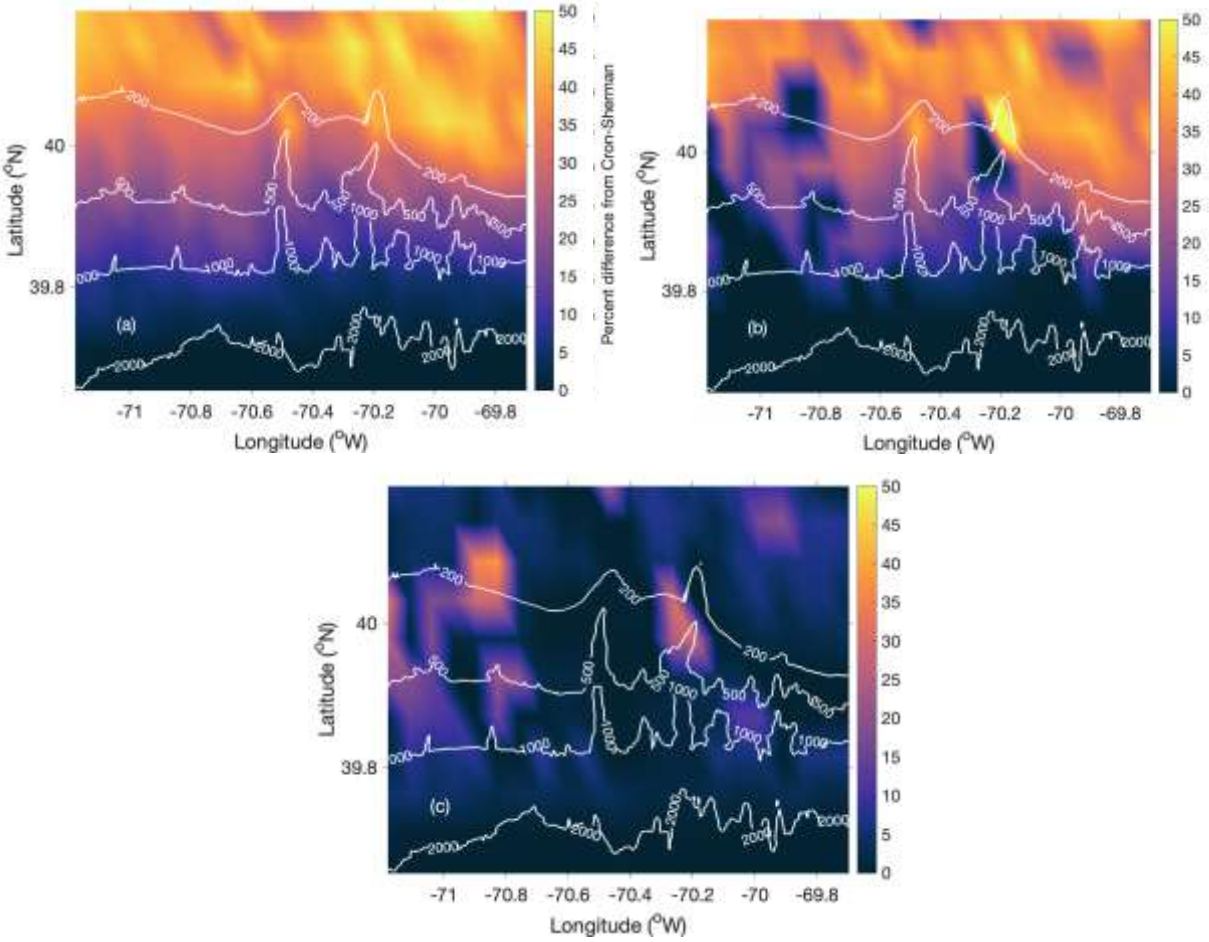

Figure 4.5: The percentage difference in the first zero-crossing frequency for (a) case 3, (b) case 4 and (c) the difference between case 3 and 4.

transect (transect A) was away from the canyon axis with a gradually decreasing bathymetry from the continental shelf to deep water. A second transect (transect B) close to the axis of the Alvin canyon was chosen to study the influence of bathymetric variation. The estimated NG of both transects and corresponding bathymetry are shown in Figures 4.7a and 4.7b respectively. NG estimates using the isotropic (black dashed line) and the Cron-Sherman (black dashed line) model are also plotted to compare with the test cases.

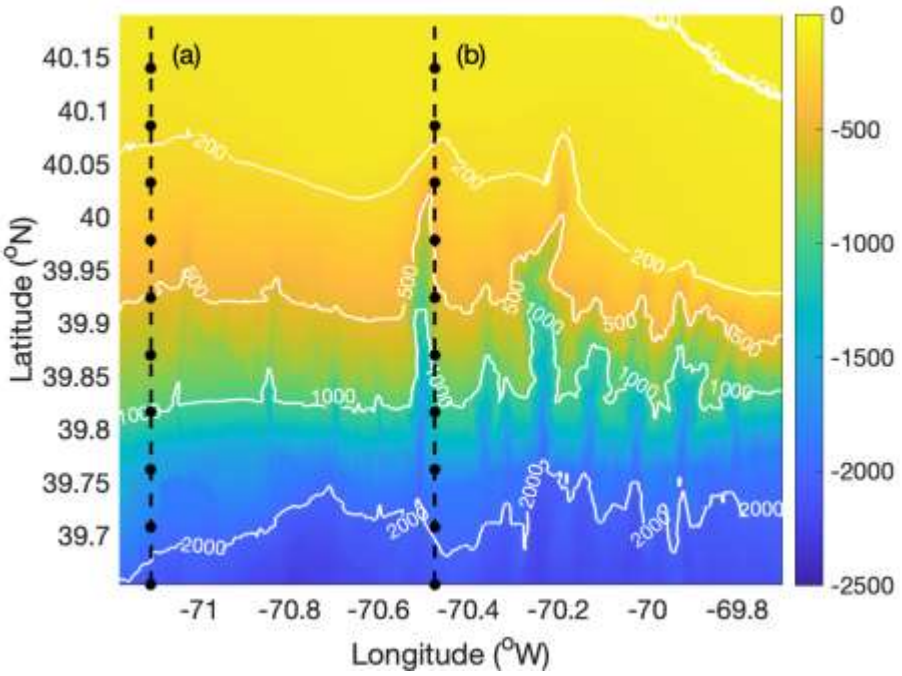

Figure 4.6: The two transects along latitude (a & b) and the bathymetry of the study region.

In Figure 4.7a, the NG increases from shallow to deep water in all four test cases. Most of the estimates for transect lie between the isotropic and the Cron-Sherman model with case 4 showing the largest variation in gain. It can be observed that the NG estimate for test cases in deep water matches with the Cron-Sherman model and the gain mostly follows the isotropic model in shallow water. The second transect is shown in Figure 4.7b also followed a similar trend as transect A, except for a slight increase in NG at the head of the canyon. This could be due to the sound focusing caused by rapid change in bathymetry at the head. The NG analysis can be used for choosing the ideal spacing of hydrophone arrays for better signal detection in active and passive acoustic experiments. Based on the above analysis it can be inferred that the ideal spacing for a hydrophone array is $\lambda/2$ in shallow water and $5\lambda/8$ in deep water. However, in regions with varying bathymetry such as continental slope and shelf-break the ideal spacing lies between $5\lambda/8$ and $\lambda/2$.

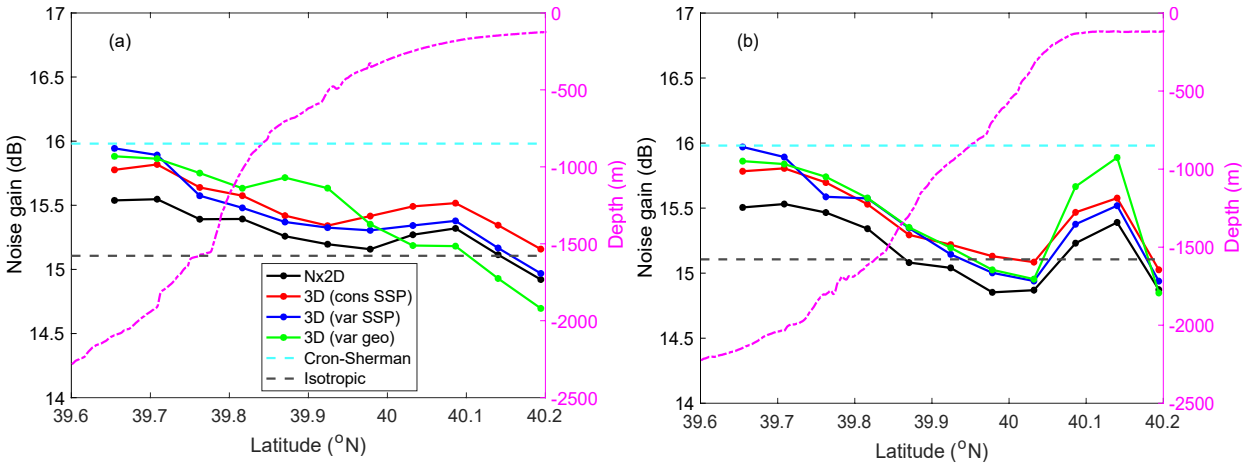

Figure 4.7: The Noise Gain estimate for a 10-element hydrophone array for (a) transect a and (b) transect b.

4.5 Conclusions

In sonar performance analysis, AG is a significant factor in determining the signal detection capability. AG not only depends on the coherence of the signal but also on the spatial coherence of ambient noise received between different array elements. Thus, an accurate representation of the ambient noise field is necessary for better signal detection. The simple analytical models of surface-generated noise coherence may not be applicable in complex environments with spatial variation in sound speed and bathymetric properties. Therefore, numerical models can be used in these environments for the accurate representation of the noise field for sonar performance analysis.

In this work, the influence of environment on surface generated ambient noise coherence on a spatial scale has been analyzed using a Nx2-D and a 3-D PE model. Range dependent bathymetry, sound speed profile and sediment type were the environmental parameters used for the simulation of the noise field. The four test cases subject to different environmental variability and realism were considered to study the relative influence of waveguide properties on noise coherence. The

comparison of noise maps for Nx2-D and 3-D environments showed that the effect of bathymetry induced horizontal refraction is minimal compared to the other factors. In shallow water, the sound speed profile is an important factor for accurately representing the noise field. Noise spatial coherence is also found to be more sensitive to seabed acoustic properties in shallow water compared to deep-water regions. Deep water regions are the least affected by the variations in environmental properties. Thus, the Cron-Sherman surface noise model is good enough to represent the spatial coherence in deep water. Furthermore, the analysis of NG estimates revealed the ideal spacing for hydrophone arrays in the continental shelf, slope, and deep-water regions.

Measurement of ambient noise coherence on a spatial scale is important for sonar performance analysis and can be used to extract information about the ocean environment. This chapter has introduced a method for mapping ambient noise coherence. Noise coherence maps are a useful tool to visualize the influence of spatially varying environmental properties on noise coherence and array performance. Although the model domain was restricted to a region near Alvin canyon, the methods and conclusions drawn from this study could be used for designing hydrophone arrays in areas with little or no environmental information. The analysis also supports the application of noise coherence modelling in the continental shelf and slope regions before conducting any transmission loss or passive acoustic experiments.

CHAPTER 5

DEPTH-DEPENDENT AMBIENT NOISE MODELLING IN CHALLENGER DEEP

5.1 Introduction

In chapters 2 and 3, methods using the vertical noise coherence for partitioning the noise field into ship-generated and wind-wave generated noise components were described, along with a technique for localizing the ships themselves. These tasks were performed using a moored set of sensors. In chapter 4, the mesoscale spatial variability of the vertical noise coherence was computed, along with its sensitivity to key physical parameters: out-of-plane (3D) propagation, and spatially varying sound speed profile and seabed sediment properties. In this chapter we use vertical coherence to investigate the depth variability of the noise field in the deep ocean using a profiling acoustic recorder.

The noise coherence model developed by Cron and Sherman (1962) has been widely used to represent the noise field in deep water environments. Assuming azimuthal uniformity, they derived an expression for vertical coherence in a semi-infinite, non-attenuating, homogenous ocean with an infinite sheet of near-surface distributed noise sources. Under these assumptions, the PSD and directional density of ambient noise are independent of position in the ocean. However, azimuthally non-uniform sources such as local shipping, rainstorms, squalls, and bathymetric focusing or shadowing can cause variation in the coherence function from the Cron-Sherman model (Barclay and Buckingham, 2013b; Barclay and Buckingham, 2014).

Besides source characteristics, the refraction of sound also affects the spatial statistics of deep water noise with respect to depth. Noise generated by ships and wind far away from the

measurement location can travel through the SOFAR channel and influence the spatial coherence (Barclay *et al*, 2017). Below the critical depth (the depth at which the sound speed is equal or greater to the surface sound speed), also known as the reciprocal or conjugate depth, the contribution of surface-generated sources with any lateral displacement from the receiver is expected to fall away (Gaul et al, 2007). Therefore, the structure of the noise power and vertical noise coherence must exhibit a depth dependence which reflects the mixture of these different effects through refraction by the sound speed profile.

The purpose of this chapter is to develop a three-component noise coherence model in deep water by incorporating different types of sources and the effects of depth dependent sound refraction. Locally generated wind, close-range ship passing, and a combination of distant wind and shipping are the three types of noise sources considered in this model. This is an extension of the noise coherence model developed to quantify the contribution of ship noise in shallow water from the long-term passive acoustic dataset discussed in chapter 2 (Shajahan *et al*, 2020). The theoretical model developed in this study can be used to identify and partition the contribution of different sources to the total noise field as a function of depth. The model may also serve as a tool to inform hardware configuration, at-sea deployment plans, and signal processing techniques for active and passive SONAR systems since it incorporates the source types, propagation physics and frequency characteristics of the sound sources.

Two sets of ambient noise and environmental data were collected using the autonomous acoustic profilers 'Deep Sound' (Barclay *et al*, 2009) and the Deep Acoustic Lander (DAL) in the Challenger Deep at the southern end of Mariana Trench in 2014 and 2021. The depth dependent ambient noise coherence was collected down to a depth of 9 km in 2014 and 10.95 km in 2021.

Deep Sound and DAL are free-falling instrument platforms designed to descent under gravity to a preassigned depth and then release a drop weight which allows them to return to the surface under buoyancy. The on-board noise recording system consists of four hydrophones, in an L shaped array with three elements aligned in the vertical and two in the horizontal. More details about the Deep Sound instrument can be found in previous publications (Barclay and Buckingham, 2013a; Barclay and Buckingham, 2014; Barclay *et al*,2009) along with details of the 2014 expedition (Barclay *et al*, 2017; Loranger *et al*, 2021). The DAL and the 2021 expedition will be briefly described here.

The remaining content of this chapter is organized as follows: The details of the instrument platforms and the two expeditions to the Challenger Deep are given in section 5.2. The derivation of the three-component noise model, and basic theory of coherence and directionality are presented in section 5.3. The experimental results and the method of noise partitioning using theoretical models is given in section 5.4. Finally, the application of the developed technique in deep water acoustic measurements is discussed in section 5.5.

5.2 Ambient Noise Measurement- Challenger Deep

5.2.1 Deep Sound and the Deep Acoustic Lander

Deep Sound is a family of free-falling (untethered) acoustic recorders designed to descend from the ocean's surface to a pre-assigned depth where it drops an iron weight and returns to the surface under its own buoyancy with a speed of ~0.5 m/s in either direction. Three variants of the instrument have been built, the Mk I, II and III. The data recorded during the Challenger Deep 2014 expedition was done by the Mk. II, while the Mk. III was lost during the same expedition. The instrument comprises of a 3.6 cm thick Vitrovex glass sphere containing the data acquisition and control hardware with a 43.2 cm outer diameter that has a depth rating of 9 km, four external

hydrophones, a conductivity-depth-temperature (CTD) sensor, and recovery beacons: a strobe, radio beacon, and satellite beacon.

Pressure time series are recorded on four High Tech Inc. HTI-99-DY hydrophones arranged in an 'L' shaped array with three elements aligned in the vertical and two in the horizontal. The hydrophones are mounted on arms that places them outside the motion-induced turbulence layer of the main instrument package. The acoustic bandwidth of this hydrophone is 5 Hz – 30 kHz, and all four channels are simultaneously sampled by the data acquisition board at a sampling rate of 204.8 kHz and a dynamic range of 24 bits. The sensors have a sea state zero sensitivity of -157 dB re: 1V / μ Pa. The CTD, a Falmouth Scientific Instruments MicroCat, provides real time depth and vertical speed data, and is used to measure temperature, salinity, density, and sound speed depth profiles.

For this deployment the instrument was configured to descend to 9 km, at which point the drop weight was triggered to release so that the platform could ascended to the surface for recovery.

The DAL is an updated version of the Deep Sound family landers, built at Dalhousie University, with an upgraded pressure rating of 11 km, or full ocean depth. The platform hardware is similar with a Vitrovex glass sphere serving as the instrument housing as well as the primary source of buoyancy. It carries the same HTI-99-DY hydrophones arranged with a bandwidth of 5 Hz – 30 kHz, a sampling rate of 128 kHz and a dynamic range of 16 bits. The CTD, manufactured by AML Oceanographic, is complemented by a sound velocity meter (SVX) which measures the in-situ sound speed using a sing-around method.

Thanks to an update in data acquisition and control hardware over its predecessor, the DAL has a longer deployment lifetime (~ 40 hours) during which it can continuously record underwater

sound on four channels. It descends and ascends more slowly through the water column, at a nominal speed of 0.4 m/s, reducing the effect of flow noise. For the 2021 expedition, DAL was configured to descend to and land on the bottom of the Challenger Deep where it remained for several hours before dropping its ballast weight and returning to the surface.

5.2.2 The 2014 Expedition

In December 2014, a multi-disciplinary expedition to the Mariana Trench on-board the Schmidt Ocean Institute's R/V Falkor departed from the island of Guam in the Western Pacific. Several autonomous, deep-diving instrument platforms were deployed in the Challenger Deep with different scientific objectives, including water-sampling and CTD profiling throughout the water column, the collection and video recording of hadal amphipods and recording the broadband ambient sound over the full ocean depth. Some of the findings from the expedition have been previously reported in popular (Nestor, 2014) and scientific literature (Barclay et al., 2017; Lan et al.,2017).

Deep Sound Mk. II was deployed at 11◦21.60' N, 142◦27.25' E in a region of the Challenger Deep known as the Central Basin, or Central Pool. Eight hours after it entered the water, the Mk. II was recovered at 11◦21.67' N, 142◦26.46' E. The local wind speed during the deployment was recorded by a meteorological station mounted on the mast of the R/V Falkor with a sample rate of 1 Hz. The mean windspeed during the deployment period was 3.2 m/s. During the deployment, the sister platform, Mk. III imploded at a nominal depth of 8600 m, generating a shock wave that was recorded on the Mk. II and discussed in detail by Loranger (Loranger *et al*, 2021).

5.2.3 The 2021 Expedition

In May of 2021, an expedition to the Challenger Deep was mounted aboard the Deep Submersible Support Vessel (DSSV) Pressure Drop, a surface vessel operated to facilitate the deployment, recovery, and maintenance of the full ocean depth rated manned submersible Limiting Factor. Along with a series of manned submarine dives that saw the collection of biological samples and video footage, DAL was deployed to collect acoustic data during its descent and ascent, and while sitting on the bottom.

DAL was deployed at 11° 19.42' N, 142° 10.23' E, and descended to the bottom of the Eastern Pool. It reached the bottom 5.5 hours after deployment and began its ascent to the surface after sitting on the bottom for 4 hours. The lander was recovered 11 hours later approximately 25 km from the drop location. The local wind speed during the deployment was recorded from a handheld anemometer on the external bridge of the DSSV Pressure Drop. The anemometer had a sample rate of 1 Hz, and computed 30 second averages, measured once every 30 minutes. The mean windspeed over the descent time was 7.7 m/s.

5.3 Theory

5.3.1 Three-Component Noise Coherence Model

Ambient noise in the ocean can be represented by the superposition of randomly generated plane waves propagating in all directions. The theoretical model of noise coherence presented in this work considers three types of sources: wind-generated, close-range (local) shipping, and distant noise (propagating in the SOFAR channel) from wind and shipping. The time series of acoustic data received at two vertically separated hydrophones can be expressed as a superposition of these three sources and are given by

$$x_1(t) = w_1(t) + v_1(t) + d_1(t) \tag{5.1}$$

and

$$x_2(t) = w_2(t) + v_2(t) + d_2(t), \tag{5.2}$$

where $w_i(t)$ is caused by locally generated wind, $v_i(t)$ is due to local shipping and $d_i(t)$ is the contribution from distant noise sources, which can be either wind, biological or shipping, on the *i*-th hydrophone. It is assumed that there exists no correlation between the noise sources, but each individual source shows some correlation across the two sensors. The PSD, CSD and the normalized CSD or coherence between two sensors are given by

$$\langle S_{ii}(\omega)\rangle = \frac{|\langle X_{ii}(\omega)\rangle|^2}{T}, \tag{5.3}$$

$$\langle S_{ij}(\omega)\rangle = \frac{\langle X_i \cdot X_j^*\rangle}{T}, \tag{5.4}$$

and

$$\Gamma_{12}(\omega) = \frac{\langle S_{12}\rangle}{\sqrt{\langle S_{11}\rangle \cdot \langle S_{22}\rangle}}, \tag{5.5}$$

where X_i is the Fourier transform of x_i, ω is the angular frequency, * denotes the complex conjugate, the angle brackets $\langle\ \rangle$ indicate an ensemble average, and T is the duration of the observation.

Combining Eqs. (5.1), (5.2) and (5.4), the uncorrelated terms go to zero and the cross spectral density becomes

$$\langle S_{ij}(\omega)\rangle = \frac{\langle W_i \cdot W_j^*\rangle + \langle V_i \cdot V_j^*\rangle + \langle D_i \cdot D_j^*\rangle}{T}, \tag{5.6}$$

where W_i, V_i and D_i are the Fourier Transforms of w_i, v_i and d_i respectively. Their dependence on the angular frequency, ω, is implied.

Assuming spatial homogeneity of noise field generated by independent sources at short distances apart, the PSD of total received signal as well as its components are independent of receiver position as given by

$$\langle S_{11}\rangle = \langle S_{22}\rangle, \tag{5.7}$$

$$\langle W_1 \cdot W_1^* \rangle = \langle W_2 \cdot W_2^* \rangle, \tag{5.8}$$

$$\langle V_1 \cdot V_1^* \rangle = \langle V_2 \cdot V_2^* \rangle, \tag{5.9}$$

and

$$\langle D_1 \cdot D_1^* \rangle = \langle D_2 \cdot D_2^* \rangle. \tag{5.10}$$

By substituting Eq. (5.6) in (5.7) and using Eqs. (5.7-5.10), the vertical coherence can be expressed as

$$\Gamma_{12}(\omega) = \frac{\langle W_1 \cdot W_2^* \rangle}{\langle W_1 \cdot W_1^* \rangle + \langle V_1 \cdot V_1^* \rangle + \langle D_1 \cdot D_1^* \rangle} + \frac{\langle V_1 \cdot V_2^* \rangle}{\langle W_1 \cdot W_1^* \rangle + \langle V_1 \cdot V_1^* \rangle + \langle D_1 \cdot D_1^* \rangle} + \frac{\langle D_1 \cdot D_2^* \rangle}{\langle W_1 \cdot W_1^* \rangle + \langle V_1 \cdot V_1^* \rangle + \langle D_1 \cdot D_1^* \rangle} \tag{5.11}$$

The denominator in each term on the R.H.S is the total received noise level on both sensors. The numerators are the CSD of wind generated noise in the first term, local vessel noise in the second term and distant noise in the third. By introducing two frequency dependent terms, the above equations can be simplified. $\beta_v(\omega)$ is the fraction of noise power due to vessels and $\beta_d(\omega)$ is the fraction of noise power due to distant sources, given as

$$\beta_v(\omega) = \frac{\langle V_1 \cdot V_1^* \rangle}{\langle S_{11} \rangle}, \tag{5.12}$$

and

$$\beta_d(\omega) = \frac{\langle D_1 \cdot D_1^* \rangle}{\langle S_{11} \rangle}, \tag{5.13}$$

Implying that the fraction of the noise field caused by locally generated wind is given by $1 - (\beta_v(\omega) + \beta_d(\omega))$. Using (5.12) and (5.13), the total received noise level at each sensor can be expressed as

$$\langle S_{11} \rangle(\omega) = \frac{\langle W_1 \cdot W_1^* \rangle}{1 - (\beta_v + \beta_d)}, \tag{5.14}$$

By substituting (5.12), (5.13) and (5.14) into (5.11), the vertical coherence of the total noise field is given by

$$\Gamma_{12}(\omega) = \big(1 - \ (\beta_v + \beta_d)\big)\frac{\langle W_1 \cdot W_2^* \rangle}{\langle W_1 \cdot W_1^* \rangle} + \beta_v \frac{\langle V_1 \cdot V_2^* \rangle}{\langle V_1 \cdot V_1^* \rangle} + \beta_d \frac{\langle D \cdot D_2^* \rangle}{\langle D_1 \cdot D_1^* \rangle}, \tag{5.15}$$

or

$$\Gamma_{12}(\omega) = \big(1 - \ (\beta_v + \beta_d)\big)\Gamma_{12}^{w}(\omega) + \beta_v \Gamma_{12}^{v}(\omega) + \beta_d \Gamma_{12}^{d}(\omega). \tag{5.16}$$

Like the two-component noise coherence model developed for shallow water in chapter 2, the total ambient noise field coherence is a weighted linear combination of three independent fields, where the weights must sum to unity. Using Cox's formula (Cox, 1973), the noise coherence can be expressed in terms of vertical directionality through a finite Fourier Transform

$$\Gamma_{12}(\omega) = \frac{1}{2}\int_0^{\pi} F(\theta)\, e^{-i\omega\tau_d \cos\theta} \sin\theta \, d\theta, \tag{5.17}$$

where $F(\theta)$ is the directional density function (normalized noise power per unit solid angle), θ is the polar angle measured from zenith, $i = \sqrt{-1}$, and τ_d is the acoustic travel time between sensors separated by a distance *d* in a medium of sound speed *c.* Based on Eqs. (5.16) and (5.17), the vertical directional density function can also be expressed as a weighed sum of uncorrelated noise field directionalities given as

$$F(\theta) = [1 - \ (\beta_v + \beta_d)]F_w(\theta) + \beta_v F_v(\theta) + \beta_d F_d(\theta), \tag{5.18}$$

where $F_w(\theta)$, $F_v(\theta)$ and $F_d(\theta)$ are the directionalities of the noise from breaking waves, local vessels and distant sources respectively.

When locally generated wind dominates the noise field, the vertical coherence in deep-water is independent of the position of hydrophones in the water column, the source spectrum level and frequency dependence of surface noise but depends only on the local sound speed between the sensors. However, the vertical directionality of ambient noise may change either due to a second sound source at close-range or refracted sound from distant sources arriving at the sensors through the sound channel axis. These contributions are represented in terms of $\beta_v(\omega)$ and $\beta_d(\omega)$ in Eq.

(5.16). When $\beta_v(\omega)$ and $\beta_d(\omega)$ are equal to zero, the resultant directionality depends only on the noise generated by breaking waves and is a complex function representing the asymmetry of the noise field. For close-range shipping, the interference effect discussed in chapter 3 can be seen as a fringing pattern in the coherogram, depending on the frequency, sensor separation, and range to ship. These fringing patterns can be seen both in the real and imaginary coherence. Sound arriving at the sensors from distant sources primarily contributes to the real part of the coherence which, as previously discussed in chapter 2, captures the symmetric component of the noise field about the horizontal. Distantly generated noise trapped in the SOFAR channel is well described by near-horizontal propagation angles (Barclay, 2017).

Analytical models of ambient noise and sound propagation can be used for modelling the total noise field coherence. Using these models of noise coherence, β_v and β_d can be inverted by replacing the L.H.S of Eq. (5.16) with noise coherence data collected using the acoustic profilers. Solving for β_v and β_d gives the absolute contribution of local shipping and distant noise in dB re 1 μPa^2/Hz

$$SN(\omega) = 10 * log\{\langle S_{11}(\omega)\rangle \cdot \beta_v(\omega)\}, \tag{5.19}$$

and

$$DN(\omega) = 10 * log\{\langle S_{11}(\omega)\rangle \cdot \beta_d(\omega)\}, \tag{5.20}$$

The above Eqs. can be used to partition and quantify the contribution of depth-dependent ship noise against the natural ambient soundscape. Additionally, the model provides appropriate framework to determine the depth-dependent mixing of local and distantly generated noise as a function of local wind speed.

The depth profile of the cross-correlation function (CCF) can also be extracted using an inverse Fourier Transform relationship between the CCF and coherence as given below

$$\psi_{12}(\zeta) = \frac{S_{11}}{2\pi}\int_{-\infty}^{\infty}\Gamma_{12}(\omega)e^{i\omega\zeta}d\omega, \tag{5.21}$$

where $\psi_{12}(\zeta)$ is the CCF between the sensors 1 and 2, and ζ is the time delay of the correlation between the time series of both sensors. The knowledge about the depth dependence of the CCF can be used to understand the range dependence of various spatial scales in the ocean. The analytical models used to process the data from Deep Sound and DAL are briefly discussed in the next section.

5.3.2 Ambient Noise and Sound Propagation Modelling

The Cron-Sherman model of ambient noise coherence has a closed-form expression for the complex coherence function given by

$$\Gamma_{12}(\omega) = 2\left[\frac{\sin kd}{kd} + \frac{\cos kd - 1}{(kd)^2}\right] + 2i\left[\frac{\cos kd}{kd} - \frac{\sin kd}{(kd)^2}\right] \tag{5.22}$$

Previous measurements of depth dependent noise coherence agree well with the Cron-Sherman model for up to 6 km (Barclay and Buckingham, 2013a). This function can be used to represent the local wind noise coherence.

Analytical or numerical model of sound propagation can be used to determine the coherence due to local shipping. Distant wind and ship noise propagating through the sound channel axis can be assumed as a plane-wave propagating horizontally with perfect symmetry in directionality between the mixed-layer depth and the conjugate depth. The frequency dependence of β_v and β_d can be written as

$$\beta_{v,d}(\omega) = \frac{2\widetilde{\beta}_{v,d}}{(\omega/\omega_0)^n + (\omega_0/\omega)^n}, \tag{5.23}$$

where n determines the roll-off in dB per octave and $\tilde{\beta}$ is the relative weight of each source. ω_0 is the reference peak frequency of the source and is chosen to be 100 Hz. When the data at low frequencies is corrupted by flow noise, a higher peak frequency can be chosen for the inversion.

The ambient noise measurement platform used in this study may introduce turbulence during ascent and descent. The effect of turbulence on noise coherence can be included by adding a scaling factor (Barclay and Buckingham, 2013b). Thus, the observed coherence can be expressed as

$$\Gamma_{12}^{s}(\omega) = \mathrm{G}_{12}(\omega)\Gamma_{12}(\omega), \tag{5.24}$$

where

$$\mathrm{G}_{12}(\omega) = \frac{1}{1+\varepsilon(\omega)}, \tag{5.25}$$

where $\varepsilon(\omega)$ is a frequency dependent signal-to-noise co-efficient and depends on the speed of the flow past the sensor, and the sensor size and geometry (Bassett *et al*, 2014). Larger values of ε indicate an increased effect of turbulence in the measured coherence, which reduces the magnitude of the coherence, as flow noise is locally generated, thus entirely incoherent between sensors. The frequency dependent scaling introduced by $\mathrm{G}_{12}(\omega)$ does not alter the zero crossing frequencies of the real or imaginary coherence curves.

5.4 Results and Discussions

5.4.1 Acoustic Data Processing

The continuous acoustic recordings from the descents of the 2014 and 2021 Challenger Deep deployments are analyzed here. The sound speed profiles measured from both deployments are shown in Figure 5.1. The conjugate depth of both measurements are just over 5 km deep. The depth of the sound channel axis in 2021 was 1140 m and was 300 m deeper than the 2014 measurement.

In the 2014 Expedition to Challenger Deep, noise data were recorded up to 8.9 km using a four-element hydrophone array. Noise data collected on the first and third sensors with a vertical separation of 0.768 m were used for processing in this study. Eqs. (5.3), (5.4) and (5.5) were used

to determine the depth-dependent PSD, cross-spectrum and coherence, respectively. Ambient noise data from each sensor were separated into 20 s segments. Each of the 20 s segments of noise data was subdivided into a further 250 segments with a duration of 0.08 s. A 2^14-point FFT was applied to process each of the subsections which were then ensemble-averaged to get a power spectrum and cross-spectrum for each 20 seconds. This time resolution corresponds to a depth resolution of ~11 m as the average speed of descending was 0.55 m/s.

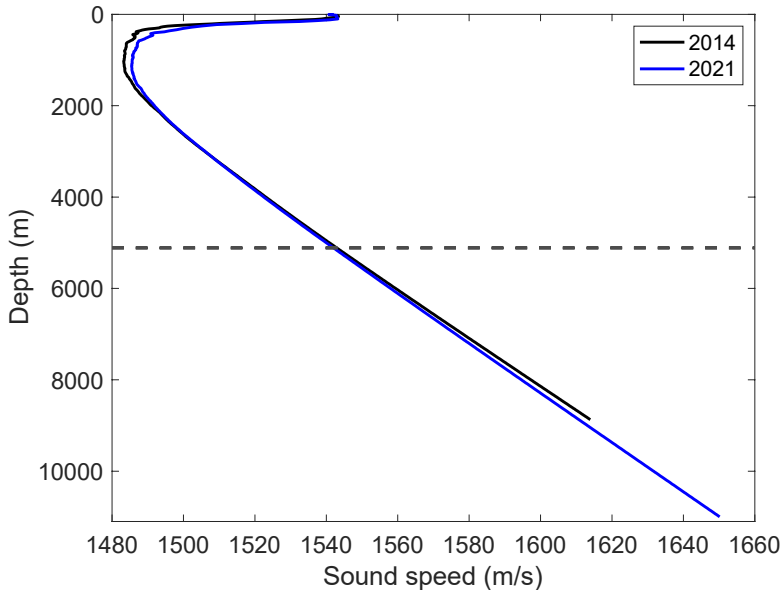

Figure 5.1: The sound speed profile of the Challenger Deep measured in 2014 (solid black line) and 2021 (solid blue line), with the conjugate depth shown by the grey dashed line.

Figs. 5.2 (a) and (b) shows the real and imaginary part of coherence as a function of normalized frequency and depth/time. The presence of a nearby ship can be identified from the coherogram between depths of 0 - 500 m. Below this, the real part of coherence shows a remarkable increase in the sound channel due to the strong presence of horizontally propagating noise, seen up to the conjugate depth. From there onwards, locally generated wind dominates the noise field. Local winds during the deployment were light, with an average speed of 3.6 m/s at 10

meters above the sea surface. The decrease in the levels of coherence from unity indicate the presence of uncorrelated turbulent noise.

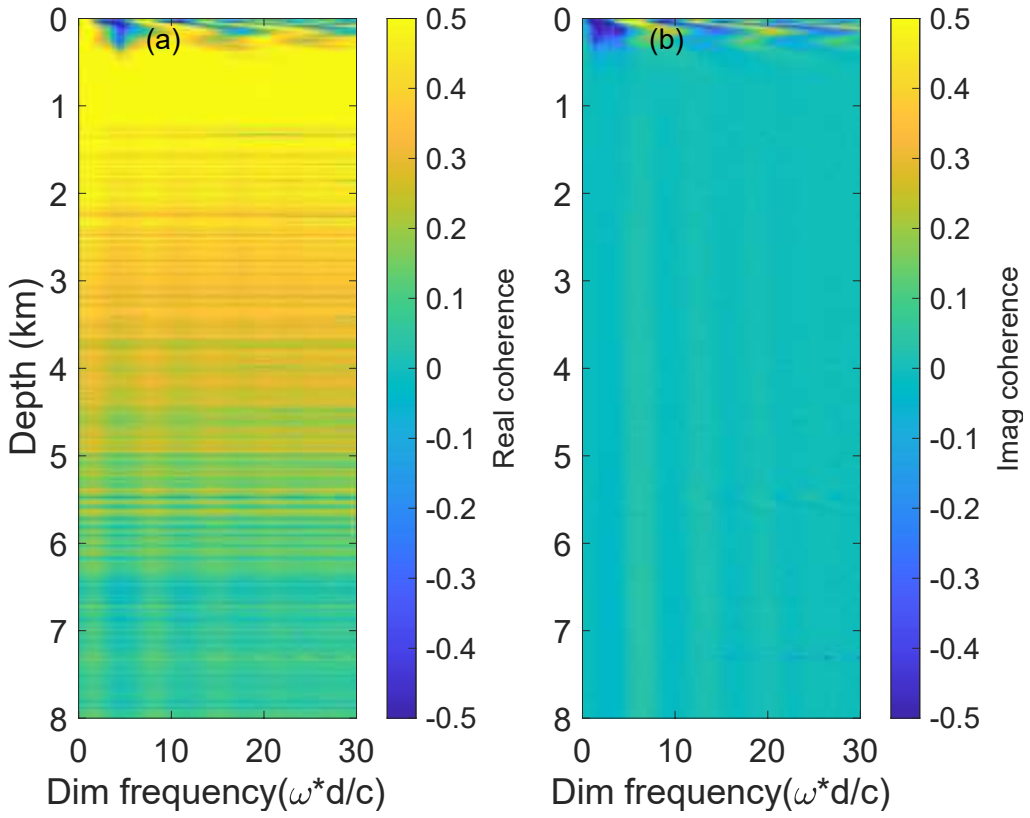

Figure 5.2. The (a) real and (b) imaginary part of vertical coherence in the Challenger Deep measured during the descent of Deep Sound in 2014

The coherogram shown in Figure 5.2 can also be interpreted in terms of the vertical directionality of the noise field. The complex coherence function indicates the asymmetry in noise directionality. For a perfectly symmetric noise field, only the real part exists and the imaginary component is zero. The real (solid blue) and imaginary (dashed blue) coherence at the sound channel axis are shown in Figure 5.3 (a) and (b), respectively. Below the conjugate depth in Figure 5.2, uniform vertical bands start to appear in both the real and imaginary coherogram, which is a characteristic of local wind-generated noise. The real (solid red) and imaginary (dashed red)

coherence curve at 7 km depth is shown in Figure 5.3. This shows the faint oscillatory nature of wind-induced coherence below the conjugate depth, with zero-crossings which align with the Cron-Sherman model.

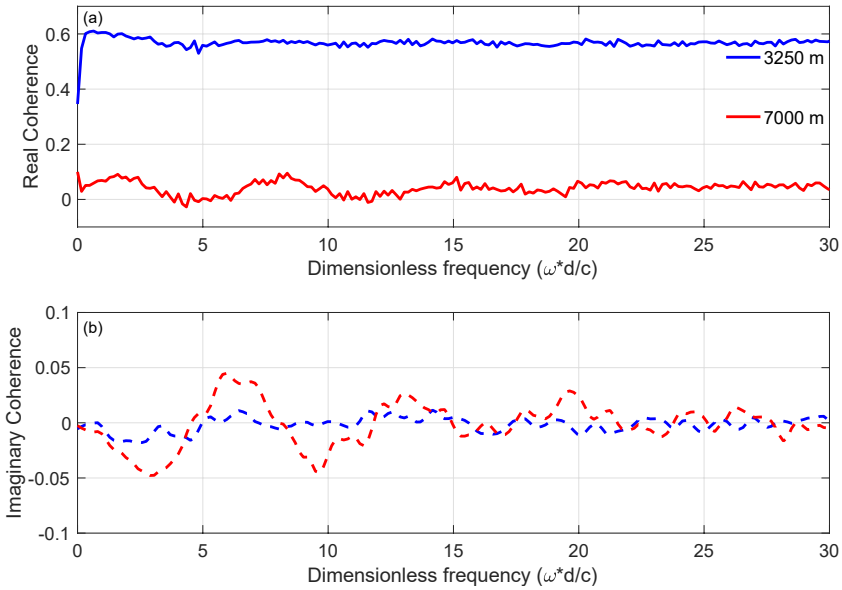

Figure 5.3: The (a) real and (b) imaginary part of vertical coherence at the sound channel axis and below the conjugate depth from the 2014 measurement.

Ambient noise measured up to 10.95 km from the 2021 expedition was used to analyze the change in its depth dependence under different environmental conditions and source characteristics. The time-series data was split into 30 s segments to compute the PSD and cross-spectrum with a corresponding depth resolution of ~ 12 m. Figure 5.4 (a) and (b) shows the real and imaginary part of coherence from the 2021 measurement. As discussed in chapter 3, the parabolic shaped pattern observed in the coherogram is a characteristic of interference effect due to a ship passing near the receiver. This effect can be seen twice; once when DAL was near the surface and again when it was at a depth of 3.5 km. The influence of the strong locally generated wind in the noise field is visible in the coherogram as uniform vertical bands in the real and imaginary coherence. These bands also indicate the homogeneous nature of wind-

generated ambient noise below the conjugate depth. The mean wind speed at 10 m above the sea surface during the deployment time was 7.7 m/s. Unlike the 2014 measurement, here the local wind conditions are strong enough such that wind-wave noise generated above the sensor dominates the noise field in the SOFAR channel and below the critical depth.

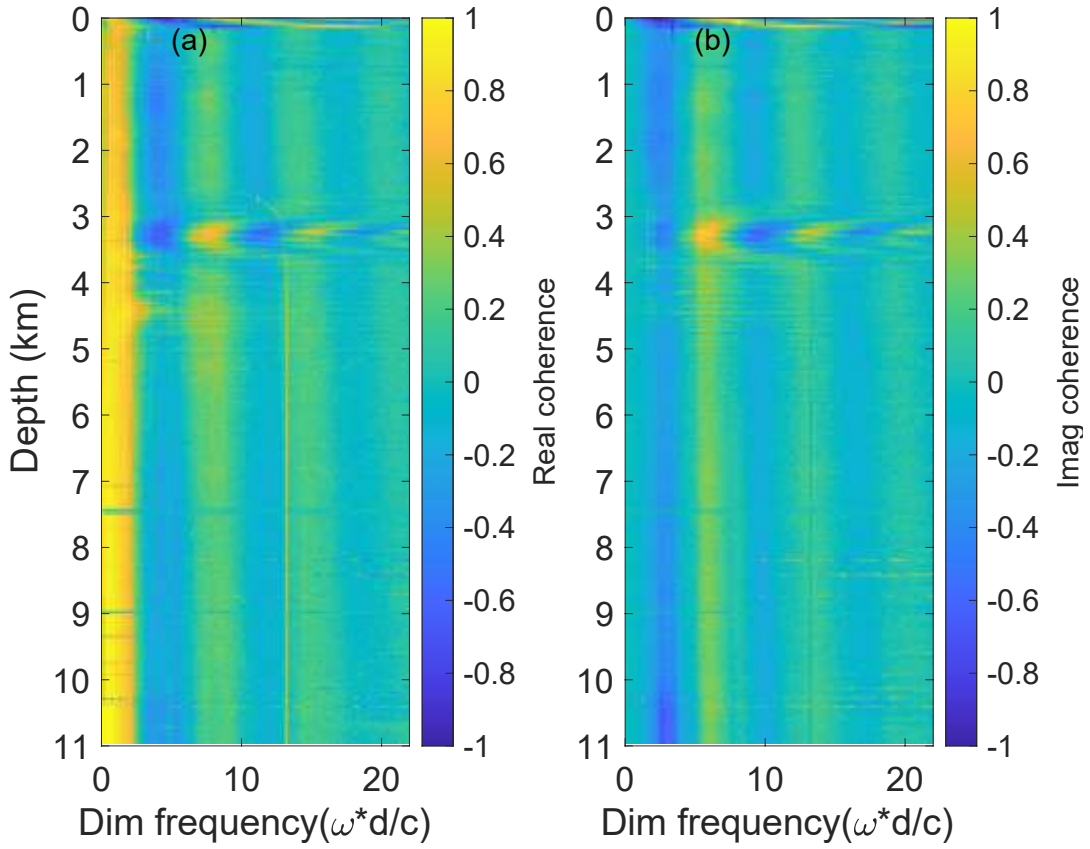

Figure 5.4: The (a) real and (b) imaginary part of vertical coherence in the Challenger Deep measured during the descent of DAL in 2021.

The significant amplitude of imaginary coherence corresponds to the asymmetry in the noise field. It shows how most of the energy is travelling downwards, even when the platform has landed on the seafloor. The lack of energy travelling upwards suggests that the sediment composition at these depths acts as a fluid with acoustic impedance similar to the water column above it and absorbs most impinging sound energy with very little reflection.

The two measurements of ambient noise from Challenger Deep show the depth-dependence of vertical coherence due to changing contributions from the various types of sources present in the environment. The noise characteristics, reflecting the composition and relative influence of contributing sources, in deep water is a time-varying property. By fitting the three-component noise coherence model, the depth-dependent power spectrum can be partitioned, and the relative and absolute contributions of each source can be determined from the measured vertical noise coherence.

5.4.2 Noise Partitioning in Deep Water

The contribution of each noise source to the total noise field can be determined by estimating β_v, β_d and thus $\left(1-(\beta_v+\beta_d)\right)$, respectively. An inversion scheme has been developed based on Eq. (5.16) to compute the absolute contribution of local wind, close-range shipping and distant wind and shipping. $\Gamma_{12}^{w}(\omega)$ in Eq. (5.16) can be represented using the Cron-Sherman model of noise coherence given in (5.22).

Close-range shipping can be modelled using a sound propagation model which depends on the sound speed profile, sediment acoustic properties and horizontal range between the ship and receiver. Local shipping can be computed using available sound propagation models and in this work, $\Gamma_{12}^{v}(\omega)$ is computed using KRAKEN, which uses the method of normal modes (Porter, 1992). The measured sound speed profile from the Challenger Deep and sediment acoustic properties of very fine-grained silty clay were used as input parameters to compute $\Gamma_{12}^{v}(\omega)$.

Distant noise, $\Gamma_{12}^{d}(\omega)$,propagating through the sound channel axis can be integrated into Eq. (5.16) as a frequency-dependent constant with perfect symmetry about the horizontal. The closed-form model given in Eq. (5.23) can be used to obtain the frequency dependence of β_v and

β_d. To account for turbulence, the model can be modified to fit the data by introducing the scaling factor,$G_{12}(\omega)$, given in Eq. 24 with a characteristic frequency slope of $f^{-5/3}$.

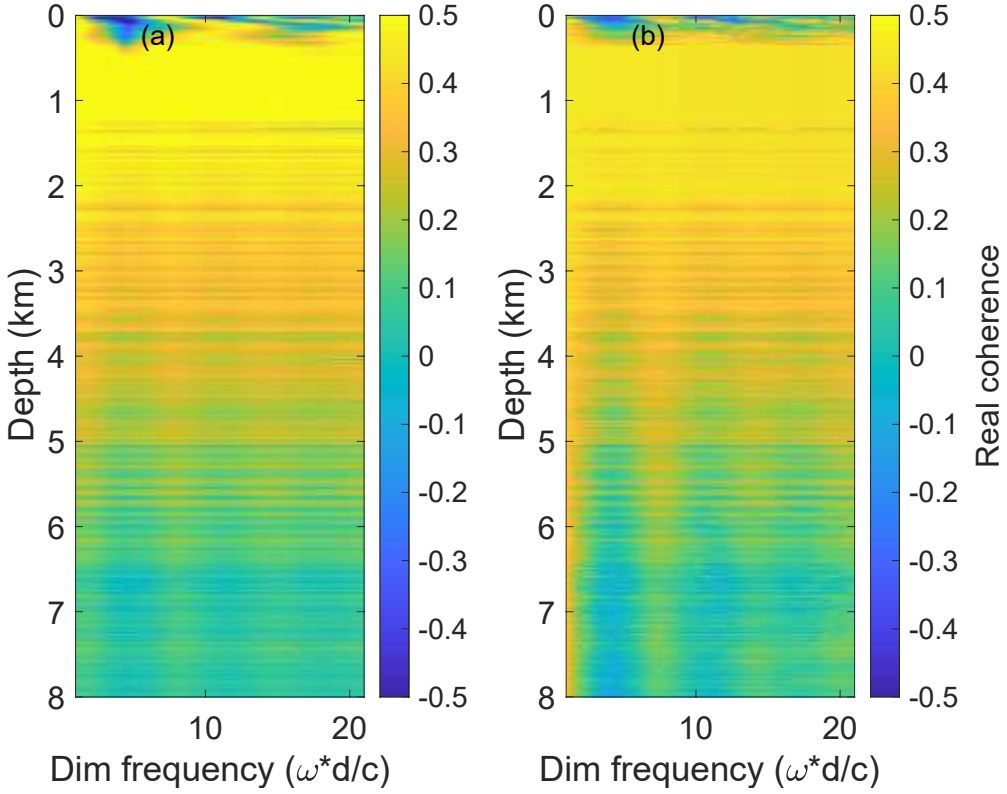

Figure 5.5: The real part of (a) measured and (b) best fit modelled vertical noise coherence from the 2014 Challenger Deep measurement.

The inversion in Eq. (5.16) depends on five free parameters: range between a local ship and the receiver $(R = 0.1 - 25\ km)$, roll-off $(n_v = 2 - 6\ dB/octave)$ of the ship's source spectrum, relative weighting $(\widetilde{\beta_v} = 0 - 1)$ of close-range shipping, relative weighting $(\widetilde{\beta_d} = 0 - 1)$ of distant wind and shipping noise and roll-off $(n_d = 2 - 6\ dB/octave)$ of the distant noise source spectrum, where the values in the parentheses are the search domains for each variable. A brute-force search over the relevant parameter space was conducted to minimize the error between simulated coherence and measured coherence at each depth. The best-fit between model and data was determined by minimizing the value of root mean square (RMS) error computed as

$$\xi\left(R,\widetilde{\beta_v},n_v,\widetilde{\beta_d},n_d\right)=\frac{1}{N}\sqrt{\sum_{i=1}^{N}\left[\Gamma_{12}^{data}(\omega_i)-\Gamma_{12}^{model}\left(\omega_i,R,\widetilde{\beta_v},n_v,\widetilde{\beta_d},n_d\right)\right]^2}\,, \tag{5.26}$$

where N is the total number of frequency points in the band 100 Hz - 6 kHz, and Γ_{12}^{model} and Γ_{12}^{data} are the simulated and measured coherence respectively. The value of signal-to-noise co-efficient (ε) used for scaling depends on the speed of the instrument platform and the strength of radiated noise field. A higher value of ε is applied to better match the measurement from 2014 due to the speed of Deep Sound and light local winds in comparison to the 2021 measurement.

The real part of measured coherence and the best fit after inversion from 2014 data are shown in Figs 5.5 (a) and (b) respectively. The simulated coherence matches well with the observations. The noise coherence model reproduced the influence of close-range shipping and distant noise propagating through the SOFAR channel. The relative weight of three main source components: local shipping (β_v), distant noise (β_d) and local wind $\left(1-\ (\beta_v+\beta_d)\right)$, are shown in Figures 5.6 (a), (b) and (c), respectively. Both local shipping and local wind contribute almost equally to the total noise field in the first 400 m, where the local ship noise is from the research vessel that deployed the lander. The sound produced by distant sources refracted towards the sound channel axis share a major portion of the total noise field between 400 m and the conjugate depth.

Below the conjugate depth, the influence of the locally generated wind noise is evident. The inversion results show the smooth mixing of the local and distant fields as a function of depth, where the distantly generated noise field dominates in the sound channel, and the locally generated noise field dominates below the critical depth. Presence of some local ship noise is found below the critical depth, though this is most likely an artefact of a noisy model-data fit or a imperfectly estimated scaling factor, $\mathrm{G}_{12}(\omega)$, in Eq. (5.24).

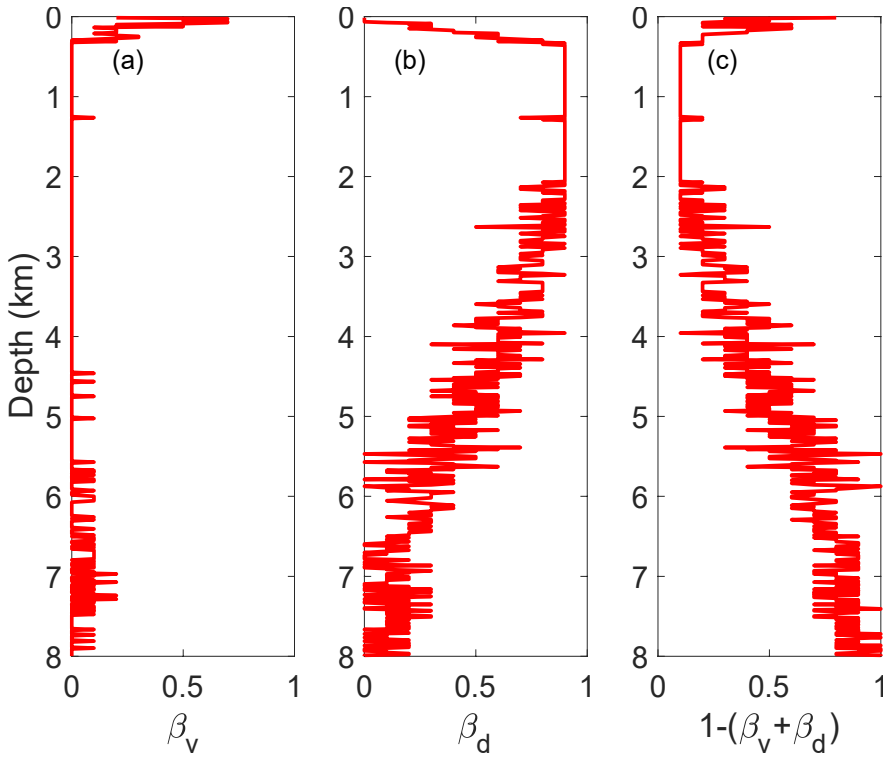

Figure 5.6: The inverted relative weight of (a) local ship, (b) distant wind and shipping, and (c) local wind generated noise during the 2014 measurement at the Challenger Deep.

The absolute contribution due to local ship noise and distant noise can be estimated from the inversion result of β_v, β_d and total received noise by Eqs. (5.19) and (5.20). The total noise power, contribution of local ship noise, distant wind and shipping, and locally generated wind at the sensor in dB re 1 mPa^2/Hz are shown in Figures 5.7(a), 5.7(b), 5.7(c) and 5.7(d) respectively.

The inversion procedure was repeated with the 2021 noise coherence measurement from Challenger Deep spanning the whole water column to a depth of 10.95 km. The measured noise coherence from 2021 data is presented in Figure 5.8 (a) and the simulated coherence after inversion is shown in Figure 5.8 (b). The three-component noise coherence model result matches remarkably well with the observation. The homogenous nature of ambient noise coherence below the conjugate depth due to the strong local wind was also reproduced in the simulation.

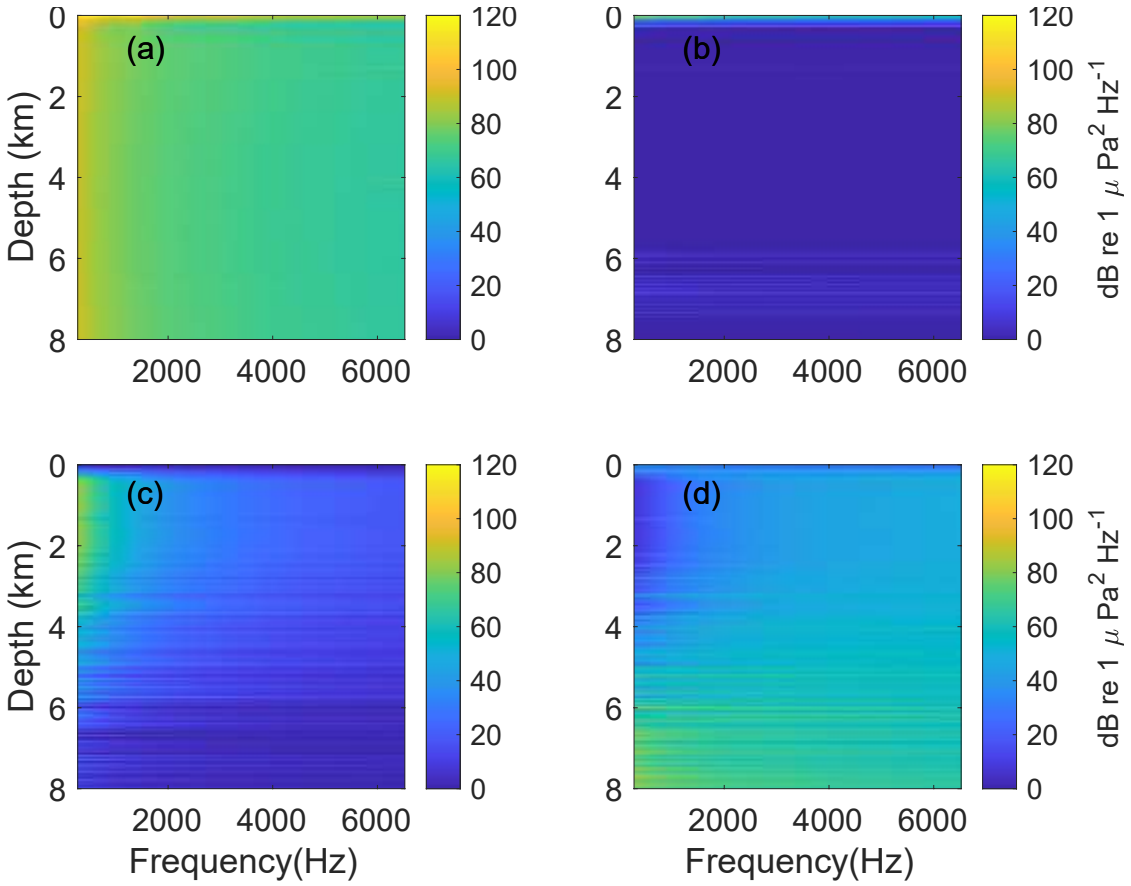

Figure 5.7: The depth-dependent (a) total received noise level, (b) absolute contribution of local shipping, (c) absolute contribution of distant noise and (d), absolute contribution of local wind generated noise from the 2014 measurement in the Challenger Deep, where color bar units are in dB re 1 μPa^2/Hz.

The inverted result of the depth-dependent relative weight of the sources considered in the simulation are given in Figures 5.9 (a), (b) and (c), respectively. Local shipping contributes more than half of the relative weight at the surface and 3.5 km depth. Compared to 2014 data, the influence of distantly generated noise was negligibly small in 2021 while the contribution of locally generated wind noise was present in the whole water column and dominates both at the sound channel axis and below the conjugate depth.

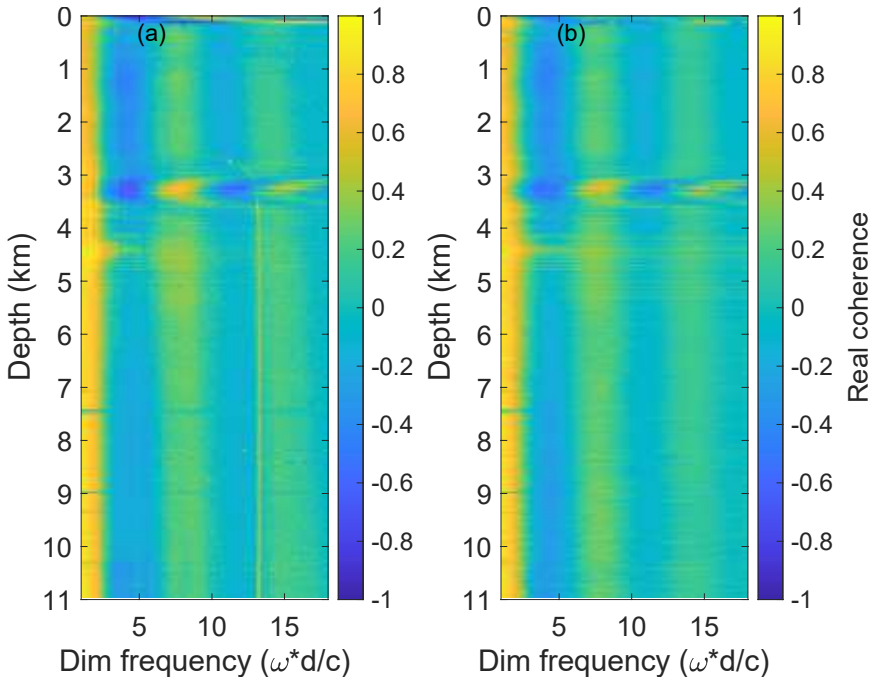

Figure 5.8: The real part of (a) measured and (b) best fit modelled vertical noise coherence from the 2021 Challenger Deep measurement.

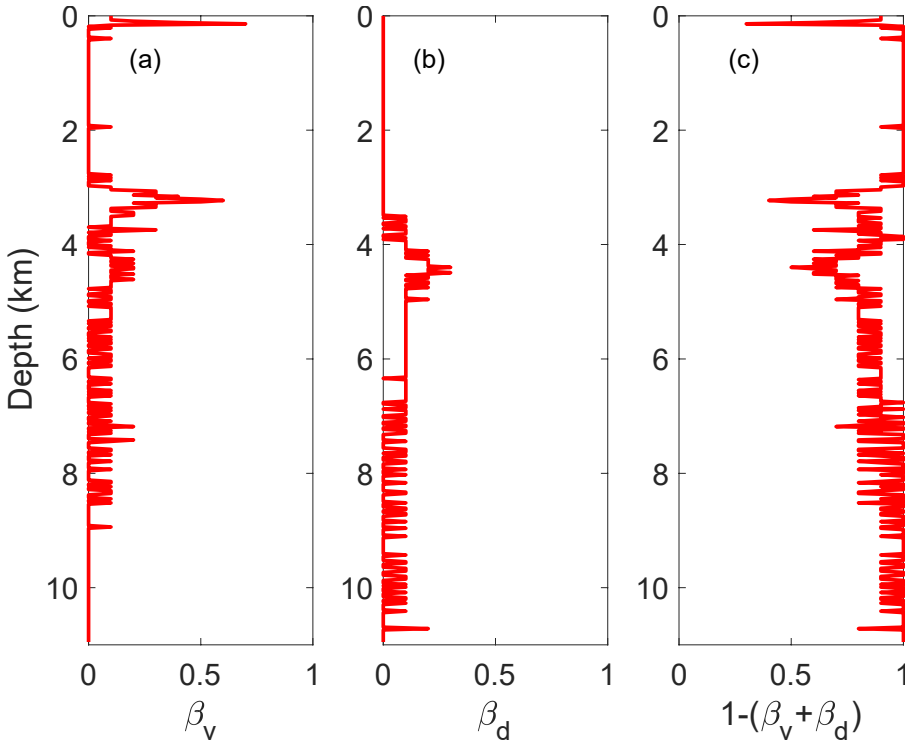

Figure 5.9: The inverted relative weight of (a) local ship, (b) distant wind and shipping, and (c) local wind generated noise in the 2021 Challenger Deep measurement.

The total received noise level and respective contribution of each source: local ship noise, distant wind and shipping, and locally generated wind in dB re 1 mPa^2/Hz from 2021 data are presented in Figures 5.10(a),5.10(b),5.10(c) and 5.10(d). The present analysis can be used to separate and quantify the influence of anthropogonic noise sources in deep water and partition the distantly and locally generated noise contributions to the PSD. The method provides the absolute contribution of each contributing source considered in the coherence model and its depth dependence without prior information, such as meteorological conditions or AIS data.

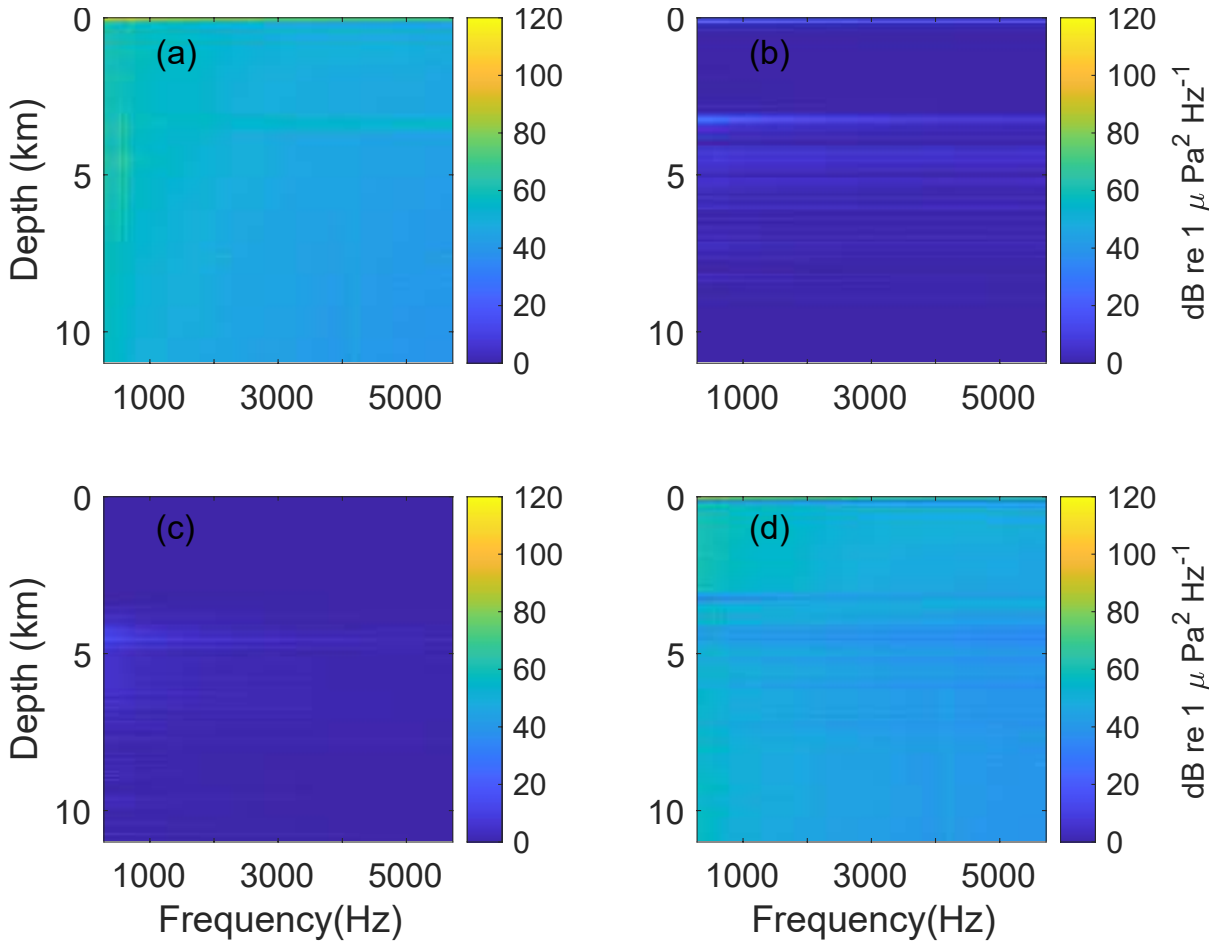

Figure 5.10: The depth-dependence of (a) total received noise level, (b) absolute contribution of local shipping, (c) absolute contribution of distant noise and (d), absolute contribution of local wind generated noise from the 2021 Challenger Deep measurement, where the color bars are in units of dB re 1 $\mu Pa^2/Hz$.

5.5 Conclusions

This chapter presents a model and inversion scheme for partitioning deep water ambient noise. A three-component noise coherence model with three major sources contributing to the noise field has been developed (local wind, local shipping and distant noise). Other sources of sound such as pile driving, dredging and sound produced by aquatic animals are not considered in the model. An analytical model of wind-generated ambient noise and a computational propagation model of vessel-generated noise were used to simulate the noise field for surface distributed wind-wave sources and local shipping. Noise propagating though the sound channel axis was modeled as a frequency-independent plane wave with total symmetry about the horizontal. Depth-dependent ambient noise coherence measured from Challenger Deep in 2014 and 2021 were used to validate the theory. The differences in depth-dependence of the vertical coherence of ambient noise was due to the difference in local wind forcing. The brute-force best-fit results match the measurements from both years, showing two states of deep ocean noise. When local winds are light, the noise field is composed of a horizontally propagating distantly generated noise at the sound channel axis and a purely locally generated wind noise at and below the critical depth. When local winds are stronger (15 knots), locally generated wind-wave noise dominates the noise field at all depths, showing the validity of the analytical Cron and Sherman model in and out of the SOFAR channel. Additionally, the method identifies and quantifies the depth-dependent ambient noise contribution from anthropogenic sources in deep water. The advantage of the present processing technique is that it needs no prior information about environmental factors such as windspeed and AIS data.

New methods need to be developed for the analysis of long-term ambient noise data to better understand the impact of anthropogenic noise. Coherence based processing method can be implemented with noise measurement from either a fixed hydrophone array or from a moving

platform. The depth-dependent noise coherence model can not only be used to predict noise levels over the entire water column, but also provides useful information for the signal processing over large arrays in TL and tomographic experiments. The inclusion of the location of noise sources and range dependent environmental parameters may aid in the extraction of the cross-correlation function for acoustic tomography. At low frequencies and long ranges, internal waves and mesoscale eddies cause variation in the vertical directivity of the noise field. With the help of a 3-D sound propagation model, the present technique may be extended to study such large-scale spatial variability.

CHAPTER 6

CONCLUSIONS

Ambient noise in the ocean depends on the type of sound sources present and the propagation environment. Thus, measurements of ambient noise can provide not only information about the soundscape, but also on the ocean environment and its boundaries. Recent developments in technology increasingly facilitate the use of multi-hydrophone systems for ambient noise monitoring. This demands the development of new processing techniques for analyzing ambient noise data. The methods introduced in this thesis discusses the benefits of using two vertically-separated sensors in noise data analysis and passive acoustic monitoring. The advantage of normalized cross-spectrum or coherence as a metric for analyzing and understanding the characteristics and composition of the noise field has been presented. A summary of results presented in this thesis followed by contributions and future possibilities are discussed below.

6.1 Summary

In chapter 2, a two-component noise model of coherence was developed, considering wind and shipping as major sources. The stability of wind noise coherence and the change in coherence pattern under all wind-strengths and wave conditions is exploited to reveal the presence of a second source in the development of the processing method. The theoretical model of wind and ship noise was validated using 29 days of continuous ambient noise data collected from Alvin Canyon. Data-model fitting of coherence allow the PSD to be partitioned and provided the absolute contribution of shipping to the total noise field as a function of space, time and frequency. The effectiveness of the method further demonstrated that wind generated noise levels could be better estimated through

partitioning based on correlation coefficient comparison of total received noise and the inversion derived wind-generated noise against measured wind speed.

A technique for source localization using vertical coherence was described in chapter 3. Coherence-based range estimations using an image theory model and the Pekeris waveguide model were found to agree well with available AIS data. The influence of bathymetry on coherence was examined using a 3-D sound propagation model in a Gaussian canyon environment. The same model was used along with the realistic bathymetry of the Alvin canyon to estimate the bearing of a close-range ship passing by the array using no received azimuthal information.

In chapter 4, a tool for visualizing the spatial variation in wind-generated noise coherence was introduced. An ambient noise model which included spatially varying sound speed profiles, sediment properties, and bathymetry, was used for the simulation with different levels of input complexity. The influence of each input was studied separately by creating maps of noise coherence and comparing modeled zero-crossings against the Cron and Sherman model as a reference. A map of NG for a nominal vertical array was also created and compared with the analytical formulas of the isotropic and Cron-Sherman noise model.

Finally, in chapter 5, the theory of a three-component noise model, which can be used to identify the depth-dependence of various noise sources under two different local wind conditions was presented. Locally generated wind noise, close-range ship noise, and distant wind and shipping noise were the three contributing sources to the theoretical model. The developed theory was compared against ambient noise profiles recorded in the Challenger Deep, Mariana Trench in 2014 and 2021, under two contrasting environmental conditions. The simulated results matched very well with the observation and the model-data fitting could retrieve the contribution of each source with respect to depth. The absolute depth-dependent power of the individual contribution

of each source was extracted from the total received noise level. For relatively high local windspeeds, it was found that the local wind noise dominated the depth-dependence, with equal power at all depths including at the sound channel axis and below the critical depth. At low local windspeeds, the influence of distantly generated noise is seen in the deep sound channel but is absent below the critical depth, where the local wind noise dominates.

6.2 Major Contributions

The processing techniques based on vertical coherence introduced in this thesis provides significant improvement in the understanding of the ocean sound field. The major advantages of these methods and their usefulness in passive acoustic data processing are elaborated in this section.

The increase in anthropogenic noise, especially shipping, and its impact on marine animals is a growing area of concern in bioacoustics and marine ecology (Duarte *et al*, 2021; Chen *et al*, 2021). To assess the potential impact of anthropogenic noise on marine life, the excess contribution of shipping above the natural background noise must be determined. Some of the recent research in this regard uses passive acoustic data along with ship distribution to identify regions of high impact (Merchant *et al*, 2014; Farcas *et al*, 2020; Erbe *et al*, 2021). Empirical models of wind noise level were used in these studies to separate the ship noise contribution above the natural soundscape. However, the soundscape contribution of wind-induced noise depends on the acoustic environment and varies geographically.

The second chapter of this thesis presented a novel method to quantify the relative and absolute contribution of ship noise in shallow water based on vertical coherence. The two-component noise model (locally generated wind and shipping) includes the propagation physics and exploits the stability of wind-generated noise directionality for ship noise quantification. In

addition to that, the processing technique doesn't require prior information about the AIS vessel track and wind speed. Thus, the use of two-sensor measurement for long-term monitoring is a viable and effective approach for passive acoustic data processing in both exactly estimating the human contribution to the soundscape which can be used to frame mitigation strategies, as well as improving estimates of the relationship between windspeed and underwater noise.

Ambient noise data have been widely used for ocean remote sensing and source localization. Some Matched Field Processing methods used for source localization explore the time delay of arrival at the hydrophones, the intensity striations observed in the spectrogram, or the narrowband matching of predicted and received acoustic fields. Typically, this involves the measurement using a large aperture VLA in deep water and multi-sensor distributed networks in shallow water (Liu *et al*, 2019; Verlinden *et al*, 2015). For a broadband acoustic source, a single sensor measurement from deep water can be used for source localization by examining the time delay information (Duan *et al*, 2014). On the other hand, the analysis of single hydrophone spectrograms for source localization in shallow water is relatively challenging due to the complexity of the environment and multipath interference.

The development of a theory and methodology for the range estimation of a broadband acoustic source using the vertical coherence between two hydrophones is given in the third chapter of this thesis. The demonstration of bearing estimation by exploiting the horizontal refraction and bathymetric asymmetry near Alvin Canyon, is shown. This method may more generally be applied to any environment with rapidly changing bathymetry. Normally, the bearing to a source is estimated using horizontal line arrays, volume arrays, or vector sensors in both shallow water and continental shelf environments (Byun *et al*, 2018; Ballard *et al*, 2013). Despite the lack of AIS data to validate the bearing estimate, the evidence of the 3-D effect caused by bathymetry

contributes to the observational evidence of this active research area (Lin *et al*, 2019). The uniqueness, reliability, and significant improvement in SNR of this technique widens the application of PAM systems in not only for soundscape monitoring but also to localize broadband acoustic sources. Moreover, the functionality of using vertical coherence for range and bearing estimation by exploiting the bathymetric variation is demonstrated for the first time.

The spatial coherence (directionality) of ambient noise is a key factor in the design of hydrophone arrays for signal detection. In sonar performance modelling, either measurements of ambient noise from a single location or simple analytical models of vertical coherence (most commonly the isotropic noise model) are typically used. However, the information regarding the environmental dependence of vertical coherence and its spatiotemporal variation is important to optimize the signal detection capability since coherence influence the performance of hydrophone arrays. Existing methods use sound pressure levels to represent the spatial dependence of ambient noise and find application in identifying regions of anthropogenic noise impact (Erbe *et al*, 2012; Miksis-Olds *et al*, 2018; Farcas *et al*, 2020). The reliability of these maps depends on the accuracy of the source spectrum level for wind-generated noise. The use of vertical coherence for mapping is an appropriate alternative since it is independent of source strength and spectral shape. A new tool to visualize the spatial variation in vertical coherence, as well as its deviation from simple model predictions is presented in the fourth chapter. The analysis quantified the relative contributions of out-of-plane propagation, seabed geoacoustic properties, and sound speed profile towards computing the vertical noise coherence. This provides some information on the geospatial sensitivity of a computational noise model to each factor. For example, it was shown that 3D models are only required near shelf break and submarine canyons. Also, the ideal spacing of sensors in the continental shelf, slope, and deep waters were shown and compared against the

isotropic and Cron and Sherman noise models. Thus, the information derived from noise coherence maps can be used to find the ideal position and spacing of hydrophone arrays for active and passive acoustic experiments.

The performance of large arrays in deep water for long-range acoustic propagation depends on the depth dependence of noise spatial coherence. Presently available analytical models of deep-water vertical coherence mainly consider wind induced noise source and do not consider the presence of a sound speed profile to derive a closed-form solution (Buckingham, 2012; Buckingham, 2013). These major sources can be broadly classified into locally generated wind noise, close-range shipping noise and distant wind and shipping noise in the sound channel. The coherence function at a specific location in deep water may change depending on the relative contribution of each of these sources. The knowledge about the depth dependence of spatial coherence is essential for noise-based inversion methods. In the fifth chapter, the development of a depth-dependent noise model which can accurately represent the noise field throughout the deep sound channel and below the critical depth is presented. The main application of the three-component noise model is to identify and partition the depth-dependent contributions of sound sources and this information is important in Green's function extraction experiments which depends on source types, spatial distribution and frequency characteristics of noise sources. The model could reproduce the profile of vertical coherence measured from Challenger Deep under different environmental conditions with substantial accuracy and may be used to inform the design and deployment of PAM, surveillance, or other acoustic receiving systems in the deep ocean to optimize their performance. Furthermore, the measurement of vertical coherence profile up to the deepest point in the ocean is presented for the first time.

6.3 Future Research Prospects

Long-term passive acoustic monitoring can be used to invert ocean environmental properties. As sound travels through the ocean, it interacts with the ocean boundaries and water column. Thus, a PAM system deployed at a specific location may not only be used to monitor the acoustic habitat but also for environmental information extraction. Moreover, monitoring the ocean through passive measurements do not cause any environmental damage. Processing techniques to understand the ocean sound field based on vertical coherence is presented in this thesis. These methods explored the advantage of two-sensor measurements in PAM systems. High-resolution oceanographic data is required for the understanding of physical oceanographic processes and climate ocean interaction. Monitoring the ocean environment using acoustics is a potential choice in regions such as the Arctic where direct profiling is difficult. Two element arrays can be easily attached to profilers and gliders for long-term monitoring. Coherence based processing could provide results comparable to multi element hydrophone arrays to retrieve complex environmental information. This demands further research in using vertical coherence as a tool for ocean observation.

Modelling evidence shows that ambient noise coherence may be used to monitor water column properties such as sound speed profile structure and ocean mixed-layer depth. Temporal variations in water column properties can be inverted using an appropriate noise coherence model and experimental data. The source localization technique based on vertical coherence can also be used for the detection and tracking of marine mammals. However, the presence of a refracting environment may introduce uncertainty in range estimates at high frequencies and long ranges. Thus, an interesting possibility is the expansion of the image theory used for source range estimation from vertical coherence to a refracting environment with a realistic sound speed profile.

The feasibility of the range localization of ships from coherence for real-time applications is an interesting future topic due to the robustness, ease of deployment and cost-effectiveness.

More at sea source localization experiments are required near rapidly changing bathymetry to further demonstrate the method of range and bearing estimation using vertical coherence. A better understanding of this 3-D effect may aid in detecting and tracking covert or sub-surface sources in the continental shelf and slope environments for defense or surveillance interests using minimal resources.

Another interesting future work would be to produce a noise coherence map that identifies regions of anthropogenic noise influence by combining an ambient noise model, a 3-D sound propagation model and AIS data, further informing sonar system design. This information can also be used to frame mitigation strategies to identify regions where anthropogenic noise has a high impact on the natural soundscape.

Lastly, the three-component noise coherence model could be combined with methods for extracting the cross-correlation function in long-term ambient noise data sets for carrying out acoustic tomography with improved fidelity. The cross-correlation function can later be used to determine the deep ocean temperature structure and to study large scale ocean variability.

REFERENCES

Aulanier, F., Simard, Y., Roy, N., Gervaise, C., and Bandet, M. (**2017**). "Effects of shipping on marine acoustic habitats in Canadian Arctic estimated via probabilistic modeling and mapping," Mar. pol. bul. **125**, 115-131.

Badiey, M., Katnelson, B. G., Lynch, J. F., Pereselkov, S., and Seigmann, W .L. (**2005**). "Measurement and modeling of three-dimensional sound intensity variations due to shallow-water internal waves," J. Acoust. Soc. Am. **117**, 613-625.

Baggeroer, A. B., Kuperman, W., and Schmidt, H. (**1988**). "Matched field processing: Source localization in correlated noise as an optimum parameter estimation problem," J. Acous. Soc. Am. **83**, 571-587.

Ballard, M. S. (**2013**). "Estimation of source range using horizontal multipath in continental shel;f environments," J. Acoust. Soc. Am. EL **134**, EL340-EL344.

Ballard, M. S., Lin, Y.-T., and Lynch, J. F. (**2012**). "Horizontal refraction of propagating sound due to seafloor scours over a range-dependent layered bottom on the New Jersey shelf," J. Acoust. Soc. Am.**131**, 2587-2598.

Barclay, D. R., Bevans, D. A., and Buckingham, M. J. (**2019**). "Estimation of the Geoacoustic Properties of the New England Mud Patch From the Vertical Coherence of the Ambient Noise in the Water Column," IEEE J. Ocea. Eng. **45**, 51-59.

Barclay, D. R., and Buckingham, M. J. (**2013a**). "Depth dependence of wind-driven, broadband ambient noise in the Philippine Sea," J. Acoust. Soc. Am. **133**, 62-71.

Barclay, D. R., and Buckingham, M. J. (**2014**). " On the spatial properties of ambient noise in the Tonga Trench, including effects of bathymetric shadowing," J. Acoust. Soc. Am. **136**, 2497-2511.

Barclay, D. R., and Buckingham, M. J. (**2013b**). "The depth-dependence of rain noise in the Philippine Sea," J. Acoust. Soc. Am. **133**, 2576-2585.

Barclay, D. R., Buckingham, M. J., and Bevans, D. A. (**2017**). "The depth-dependence of ambient noise coherence in the Challenger Deep," Acoust. Bullet. **42(4)**, 36-40.

Barclay, D. R., and Lin, Y.-T. (**2019**). "Three-dimensional noise modeling in a submarine canyon," J. Acous. Soc. Am. **146**, 1956-1967.

Barclay, D. R., Simonet, F., and Buckingham, M. J. (**2009**). "Deep Sound: A freefalling senosr platformfor depth profiling ambient noise in the deep," Mar. Technol. Soc. J. **43**, 144-150.

Bassett, C., Thomson, J., Dahl, P. H., and Buckingham, M. J. (**2014**). "Flow-noise and turbulence in two tidal channelsDepth dependence of wind-driven, broadband ambient noise in the Philippine Sea," J. Acoust. Soc. Am. **135**, 1764-1774.

Bermant, P. C., Bronstein, M. M., Wood, R. J., Gero, S., and Gruber, D. F. (**2019**). "Deep machine learning techniques for the detection and classification of sperm whale bioacoustics," Sci. Reports. **9**, 12588.

Bianco, M. J., and others (**2019**). "Machine learning in acoustics: theory and applications," J. Acous. Soc. Am. **146**, 3590-3628.

Brienzo, R. K., and Hodgkiss, W. S. (**1993**). "Broadband matched-field processing," J. Acous. Soc. Am. **94**, 2821-2831.

Buckingham, M. J. (**1979**). " Array gain of a broadside vertical line array in shallow water " J. Acoust. Soc. Am. **65**, 148-161.

Buckingham, M. J. (**1980**). "A theoretical model of ambient noise in a low-loss, shallow water channel," J. Acoust. Soc. Am. **67**, 1186-1192.

Buckingham, M. J. (**1981**). "Spatial coherence of wind-generated noise in a shallow ocean channel," J. Acoust. Soc. Am. **70**, 1412-1420.

Buckingham, M. J. (**1987**). "Theory of three-dimensional acoustic propagation in a wedgelike ocean with a penetrable bottom," J. Acoust. Soc. Am. **82**, 198-210.

Buckingham, M. J. (**2011**). "On the two-point cross-correlation function of anisotropic, spatially homogeneous ambient noise in the ocean and its relationship to the Green's function," J. Acoust. Soc. Am. **129**, 3562-3576.

Buckingham, M. J. (**2012**). "Cross correlation in band limited ocean ambient noise fields," J. Acous. Soc. Am. **131**, 2643-2657.

Buckingham, M. J. (**2013**). "Theory of the directionality and spatial coherence of wind-driven ambient noise in a deep ocean with attenuation," J. Acous. Soc. Am. **134**, 950-958.

Buckingham, M. J., and Jones, S. A. (**1987**). "A new shallow-ocean technique for determining the critical angle of the seabed from the vertical directionality of the ambient noise in the water column," J. Acous. Soc. Am. **81**, 938-946.

Byun, G., Song, H. C., Kim, J. S., and Park, J. S. (**2018**). "Real time tracking of a surface ship using a bottom-mounted horizontal array," J. Acous. Soc. Am. **144**, 2375-2382.

Carbone, N. M., Deane, G. B., and Buckingham, M. J. (**1998**). "Estimating the compressional and shear wave speeds of a shallow water seabed from the vertical coherence of ambient noise in the water column," J. Acous. Soc. Am. **103**, 801-813.

Carey, W. M. (**2009**). "Lloyd's mirror-image interference effects," Acoustics Today **5**, 14-20.

Carey, W. M., and Evans, R. B. (**2011**). "Ocean Ambient Noise: Measurement and Theory," (Springer, NewYork).

Carey, W. M., Evans, R. B., Davis, J. A., and Botseas, G(**1990**). "Deep-ocean vertical noise directionality," IEEE J. Ocean. Eng. **15**, 324-334.

Caruso, F., Dong, L, Lin, M., Liu M., Gong, Z., Xu, W., Alonge, G., and Li, S. (**2020**). "Monitoring of a nearshore small dolphin species using passive acoustic platforms and supervised machine learning techniques," Front. Mar. Sci. **7**: 267.

Chapman, D. M., Ward, P. D., and Ellis, D. D. (**1989**). "The effective depth of a Pekeris ocean waveguide, including shear wave effects," J. Acous. Soc. Am. **85**, 648-653.

Chapman, N. R., and Price, A. (**2011**). "Low frequency deep ocean ambient noise trend in the Northeast Pacific Ocean," J. Acous. Soc. Am. **129**, EL161-EL165.

Chen, C., Lin, T. H., Watanabe, H. K., Akamatsu, T., and Kawagucci, S. (**2021**). "Baseline soundscapes of deep sea habitats reveal heterogeniety among ecosystems and sensitivity to anthropogenic impacts," Limnol. Oceanogr. **66**, 3714-3727.

Chiu, L. Y. S., Lin, Y.-T., Chen, C. F., Duda, T. F., and Calder, B. (**2011**). " Focused sound from three-dimensional sound propagation effects over a submarine canyon," J. Acoust. Soc. Am. EL **129**, EL 260-266.

Colosi, J. A., and others (**1999**). "Comparisons of measured and predicted acoustic fluctuations for a 3250 km propagation experiment in the eastern North Pacific Ocean," J. Acous. Soc. Am. **105**, 3202-3218.

Cox, H. (**1962**). "Spatial correlation in arbitrary noise fields with application to ambient noise," J. Acoust. Soc. Am. **54**, 1289-1301.

Cron, B. F., and Sherman, C. H. (**1962**). "Spatial correlation functions for various noise models," J. Acoust. Soc. Am. **34**, 1732-1736.

Deane, G. B., Buckingham, M. J., and Tindle, C. T. (**1997**). "Vertical coherence of ambient noise in shallow water overlying a fluid seabed," J. Acoust. Soc. Am. **102**, 3413.

Duan, R., Yang, K., Ma, Y., Yang, Q., and Li, H. (**2014**). "Moving source localization with a single hydrophone using multipath time delays in the deep ocean," J. Acoust. Soc. Am. EL **136**, EL 159-165.

Duan, R., Yang, K., Li, H., and Ma, Y. (**2017**). "Acoustic-intensity striations below the critical depth: Interpretation and modeling," J. Acoust. Soc. Am. **142**, EL 245-250.

Duarte, C. M., and others (**2021**). "The soundscape of the Anthropocene ocean," Science **371**, eaba4658.

Erbe, C., MacGillivray, A., and Williams, R. (**2012**). "Mapping cumulative noise from shipping to inform marine spatial planning," J. Acoust. Soc. Am. EL **132**, EL423-EL428.

Erbe, C., Schoeman, R. P., Peel, D., and Smith, J. N. (**2021**). "It often howls more than it chugs: wind versus ship noise underwater in Australia's maritime regions," J. Mar. Sci. Eng. **9**, 472.

Farcas, A., Powell, C. F., Brookes, K. L., and Merchant, N. D. (**2020**). "Validated shipping noise maps of the Northeast Atlantic," Sci. Total Environ. **735**, 139509.

Farmer, D. M., and Vagle, S. (**1988**). "On the determination of breaking wave distributions using ambient sound," J. Geophy. Res. **93**, 3591-3600.

Fialkowski, L. T., Collins, M. D., Kuperman, W., Perkins, J. S., Kelly, L. J., Larsson, A., Fawcett, J. A., and Hall, L. H. (**2000**). "Matched-field processing using measured replica fields," J. Acoust. Soc. Am. **107**, 739-746.

Frisk, G. V. (**2012**). "Noiseonomics: The relationship between ambient noise levels in the sea and global economic trends," Sci. rep. **2**, 437.

Gassmann, M., Wiggins, S. M., and Hildebrand, A. (**2017**). "Deep-water measurements of container ship radiated noise signatures and directionality," J. Acous. Soc. Am. **142**, 1563-1574.

Gaul, R. D., Knobles, D. P., Shooter, J. A., and Wittenborn, A. F. (**2007**). "Ambient noise analysis of deep ocean measurements in the Northeast Pacific," IEEE J. Ocea. Eng. **32**, 497-512.

Gervaise, C., Aulanier, F., Simard, Y., and Roy, N. (**2015**). "Mapping probability of shipping sound exposure level," J. Acoust. Soc. Am. **137**, EL429-EL435.

Gibb, R., Browning, E., Kapfer, P. G., and Jones, K. E. (**2019**). "Emerging oppertunities and challenges for passive acoustics in ecological assessment and monitoring," Methods. Ecol. Evol. **10**, 169-185.

Godin, O. A., Brown, M. G., Zabotin, N. A, Zabotina, L, and Williams, N. J. (**2014**). "Passive acoustic measurement of flow velocity in the Straits of Florida," Geosci. Lett. **1(6)**, 1-7.

Hamilton, E. L. (**1980**). "Geoacoustic modeling of the sea floor," J. Acoust. Soc. Am. **68**, 1313-1340.

Hamson, R. M. (**1980**). " The theoretical gain limitations of a passive vertical line array in shallow water," J. Acoust. Soc. Am. **68**, 156-164.

Harris, P., Sotirakopoulos, K., Robinson, S., Wang, L., and Livina, V. (**2019**). "A statistical method for the evaluation of long term trends in underwater noise measurements," J. Acous. Soc. Am. **145**, 228-242.

Harrison, C. H. (**1996**). "Formulas for ambient noise level and coherence," J. Acoust. Soc. Am. **99**, 2055-2066.

Harrison, C. H. (**1997**). "Noise directionality for surface generated source sin range dependent environments," J. Acoust. Soc. Am. **102**, 2655-2662.

Harrison, C. H, and Simons, D. G. (**2002**). "Geoacoustic inversion of ambient noise: a simple method," J. Acoust. Soc. Am. **112**, 1377-1389.

Heaney, K. D., and Murray, J. D. (**2009**). "Measurements of three-dimensional propagation in a continental shelf environment," J. Acoust. Soc. Am. **125**, 1394-1402.

Heaney, K. D., and Campbell, R. L. (**2016**). " Three-dimensional equation modeling of mesoscale eddy deflection," J. Acoust. Soc. Am. **139**, 918-926.

Ingenito, F., and Wolf, S. N. (**1989**). "Site dependence of wind-dominated ambient noise in shallow water," J. Acous. Soc. Am. **85**, 141-145.

Jensen, F. B. (**1994**). *Computational ocean acoustics* (Amer Inst of Physics).

Jensen, F. B., Kuperman, W. A., Porter, M. B., and Schmidt, H. (**2011**). *Computational ocean acoustics* (Springer Science & Business Media).

Kline, L. R., and others (**2020**). "Sleuthing with sound: Understanding vessel activity in marine protected areas using passive acoustic monitoring," Marine. Policy. **120**, 104138.

Kuperman, W. A., and Ingenito, F. (**1980**). "Spatial correlation of surface generated noise in a stratified ocean," J. Acoust. Soc. Am. **67**, 1988.

Lan, Y., Sun, J., Tian, R., Bartlett, D. H., Li, R., Wong, Y. H., Zhang, W., Qui, J. W., Xu, T., He, L. S., and others. (**2017**). "Molecular adaptation in the world's deepest living animal: Insights from transcriptome sequencing of the hadal amphipod Hirondellea gigas," Molec. Ecol. **26(14)**, 732-743.

Lei, Z., Yang, K., and Ma, Y. (**2016**). "Passive localization in the deep ocean based on cross-correlation function matching," J. Acoust. Soc. Am. **139**, EL 196-201.

Lin, Y.-T., Duda, T. F., Emerson, C., Gawarkiewicz, G., Newhall, A. E., Calder, B., Lynch, J. F., Abbot, P., Yang, Y.-J., and Jan, S. (**2015**). "Experimental and numerical studies of sound propagation over a submarine canyon northeast of Taiwan," IEEE J. O. E. **40**, 237-249.

Lin, Y. T., Duda, T. F., and Newhall, A. E. (**2013**). "Three-dimensional sound propagation models using the parabolic-equationapproximatin and the splt-step Fourier method," J. Comput. Acoust. **21**, 1250018.

Lin, Y.-T., McMahon, K. G., Lynch, J. F., and Siegmann, W. L. (**2013**). "Horizontal ducting of sound by curved nonlinear internal gravity waves in the continental shelf areas," J. Acoust. Soc. Am. **133**, 37.

Lin, Y.-T., Newhall, A. E., Miller, J. H., Potty, G. R., and Raposa, J. V. (**2019**). "A Three-dimensional underwater sound propagation model for offshore wind farm noise prediction," J. Acoust. Soc. Am. **145**, EL 335-340.

Lin, Y. T., Porter, M. B., Sturm, F., Isakson, M. J., and Chiu, C. S. (**2019**). "Introduction to the special issue on three-dimensional underwater acoustics," J. Acous. Soc. Am. **146**, 1855-1857.

Liu, W., Yang, Y., Lu, L., Shi, Y., and Liu, Z. (**2019**). "Source localization by matching sound intesity with a vertical array in the deep ocean," J. Acoust. Soc. Am. EL **132**, EL423-EL428.

Loranger, S., Barclay, D., and Buckingham, M. J. (**2021**). "Implosion in the Challenger Deep: echo sounding with the shock wave," Oceanography. **34(2)**, 51-59.

Lynch, J. F., Lin, Y. T., Duda, T. F., and Newhall, A .E. (**2010**). "Acoustic ducting, reflection, refraction and dispersion by curved non-linear internal waves in shallow water," IEEE J.O.E. **35**, 12-27.

Mackenzie, K. V. (**1981**). "Discussion of sea-water sound speed determinations," J. Acoust. Soc. Am. **70**, 801-806.

Martin, S. B., Morris, C., Bröker, K., and O'Neill, C. (**2019**). "Sound exposure level as a metric for analyzing and managing underwater soundscapes," J. Acous. Soc. Am. **146**, 135-149.

McDonald, M. A., Hildebrand, J. A., and Wiggins, S. M. (**2006**). "Increases in deep ocean ambient noise in the Northeast Pacific west of San Nicolas Island, California," J. Acous. Soc. Am. **120**, 711-718.

Mckenna, M. F., Ross, D., Wiggins, S. M., and Hilderbrand, J. A. (**2012**). "Underwater radiated noise from modern commercial ships," J. Acoust. Soc. Am. **131**, 92-103

Merchant, N. D., Pirotta, E., Barton, T. R., and Thompson, P. M. (**2014**). "Monitoring ship noise to assess the impact of coastal developments on marine mammlas," Mar. pol. bull. **78**, 85-95.

Merchant, N. D., Witt, M. J., Blondel, P., Godley, B. J., and Smith, G. H. (**2012**). "Assessing sound exposure from shipping in coastal waters using a single hydrophone and Automatic Identification System (AIS) data," Mar. pol. bull. **64**, 1320-1329.

Michalopoulou, Z.-H., and Porter, M. B. (**1996**). "Matched-field processing for broad-band source localization," IEEE J.O.E. **21**, 384-392.

Miksis-Olds, J. L., Martin, B., and Tyack, P. L. (**2018**). "Exploring the ocean through soundscapes," Acoustics Today **14**, 26-34.

Miksis-Olds, J. L., and Nichols, S. M. (**2016**). "Is low frequency ocean sound increasing globally?," J. Acous. Soc. Am. **139**, 501-511.

Munk, W., Worcester, P., and Wunsch, C. Ocean Acoustic Tomography. (Cambridge U. P., Cambridge, 1995)

Muzi, L., Siderius, M., Quijano, J. E., and Dosso, S. E. (**2015**). "High-resolution bottom-loss estimation using the ambient-noise vertical coherence function," J. Acous. Soc. Am. **137**, 481-491.

Muzi, L., Siderius, M., and Nielsen, P. L. (**2016**). "Frequency based noise coherence-function extension and application to passive bottom-loss estimation," J. Acous. Soc. Am. **140**, 1513-1524.

Muzi, L., Siderius, M., and Gebbie, J. (**2018**). "An alalysis of beamforming algorithms for passive bottom reflection-loss estimation," J. Acous. Soc. Am. **144**, 3046-3054.

Nestor, J. (**2014**). "Deep: Freediving, Renegade science, and what the ocean tells us about ourselves," Eamon Dolan/Houghton Mifflin Harcourt, 290.

NSF Ocean Observatories Initiative Data Portal. "Mean wind speed (CP04 OSSM-SBD11-06-METBKA000) data from 05 April 2016 to 05 May 2016," (Downloaded on 15 March 2017, https://oceanobservatories.org).

Nystuen, J. A., McGlothin, C. C., and Cook, M. S. (**1993**). "The underwater sound generated by heavy rainfall," J. Acoust. Soc. Am. **93**, 3169-3177.

Pereira, A., Harris, D., Tyack, P., and Matias, L. (**2016**). "Lloyd's mirror effect in fin whale calls and its use to infer the depth of vocalizing animals," in *Proceedings of Meetings on Acoustics 4ENAL* (Acoustical Society of America), p. 070002.

Perkins, J. S., and Kuperman, W. A. (**1990**). "Environmental signal processing: Three-dimensional matched-field processing with a vertical array," J. Acoust. Soc. Am. **87**, 1553-1556.

Popper, A. N., and Hawkins, A. (**2016**). *The effects of noise on aquatic life II* (Springer).

Porter, M. B. (**1992**). "The kraken normal model program," Naval Research Lab, Washington, DC.

Porter, M. B. (**2011**). "The bellhop manual and user's guide: Preliminary draft," Heat, Light, and Sound Research, Inc., La Jolla, CA, USA, Tech. Rep **260**.

Porter, M. B. (**2016**). "Bellhop3d user guide," Techical report, Heat, Light, and Sound Research Inc.

Porter, M. B. (**2019**). "Beam tracing for two-and three-dimensional problems in ocean acoustics," J. Acoust. Soc. Am. **146**, 2016-2029.

Putland, R. L., Merchant, N. D., Farcas, A., and Radford, C. A. (**2018**). "Vessel noise cuts down communication space for vocalizing fish and marine mammals," Glo. Change Bio. **24**, 1708-1721.

Reid, J. M., Reid, J. A., Jenkins, C. J., Hastings, M. E., Williams, S. J., and Poppe, L. J. (**2005**). "usSEABED: Atlantic coast offshore surficial sediment data release," US Geological Survey Data Series **118**.

Rolland, R. M., Parks, S. E., Hunt, K. E., Castellote, M., Corkeron, P. J., Nowacek, D. P., Wasser, S. K., and Kraus, S. D. (**2012**). "Evidence that ship noise increases stress in right whales," Proc. Roy. Soc. B: Bio. Sci. **279**, 2363-2368.

Rutgers Ocean Modelling Group"ESPRESSO ocean modelling from Rutgers ROMS group," available at http://www.myroms.org/espresso/

Ryan, W., Carbotte, S., Coplan, J., O'Hara, S., Melkonian, A., Arko, R., Weissel, R., Ferrini, V., Goodwillie, A., and Nitsche, F. (**2009**). "Global Multi-Resolution Topography (GMRT) synthesis data set. G-cubed 10 (3), Q03014."

Sabra, K. G., Roux, P., and Kuperman, W. A. (**2005**). "Emergence rate of the time domain Green's function from the ambient noise cross-correlation function," J. Acoust. Soc. Am. **118**, 3524-3530.

Sagers, J. D., Ballard, M. S., and Knobles, D. P. (**2014**). "Evidence of three-dimensional acoustic propagation in the Catoche tongue," J. Acoust. Soc. Am. **136**, 2453-2462.

Sanguineti, M., Guidi, C., Kulikovskiey, V., and Taiuti, M. G. (**2021**). "Real-time continuous monitoring of marine mammals in the Mediterranean Sea" J. Mar. Sci. Eng. **9**, 1389

Seger, K. D., Al-badrawi, M. H., Miksis-Olds, J. L., Kirsch, N. J., and Lyons, A. P. (**2018**). "An emperical mode decomposition based detection and classification approach for marine mammal vocal signals," J. Acous. Soc. Am. **144**, 3181-3190.

Shajahan, N., and Barclay, D. R. (**2019**). "The effect of submarine canyon bathymetry on range estimation using cross-correlated noise field," J. Acoust. Soc. Am. 146, 2858.

Shajahan, N., Barclay, D. R., and Lin, Y.-T. (**2020**). "Quantifying the contribution of ship noise to the underwater sound field," J. Acoust. Soc. Am. **148**, 3863-3872.

Siderius, M., Harrison, C. H., and Porter, M. B. (**2006**). "A passive fathometer technique for imaging seabed layering using ambient noise," J. Acoust. Soc. Am. **120**, 1315-1323.

Siderius, M., Muzi, L., Harrison, C. H., and Nielsen, P. L. (**2013**). "Synthetic array processing of ocean ambient noise for higher resolution seabed bottom loss estimation," J. Acous. Soc. Am. **133**, EL149-EL155.

Stephen, R. A., Bolmer, S. T., Worcester, P. F., Dzieciuch, M. A., and Udovydchenkov, I. A. (**2019**). "Three-dimensional bottom diffraction in north Pacific," J. Acoust. Soc. Am. **146**, 1913-1922.

Tappert, F. D. (**1974**). "Parabolic equation method in underwater acoustics," J. Acoust. Soc. Am. **55**, S34.

Thode, A. (**2004**). "Tracking sperm whale (Physeter macrocephalus) dive profiles using a towed passive acoustic array," J. Acoust. Soc. Am. **116**, 245-253.

Thode, A. (**2005**). "Three-dimensional passive acoustic tracking of sperm whales (Physeter macrocephalus) in ray-refracting environments," J. Acoust. Soc. Am. **118**, 3575-3584.

Tiemann, C. O., Thode, A. M., Straley, J., O'Connell, V., and Folkert, K. (**2006**). "Three-dimensional localization of sperm whales using a single hydrophone," J. Acoust. Soc. Am. **120**, 2355-2365.

Unidata. (**2016**) : THREDDS Data Server (TDS) version 4.6.2 [software] Boulder, CO:UCAR/Unidata (http://doi.org/10.5065/D6N014KG).

Urick, R. **(1967)**. Principles of underwater sound for Engineers (Peninsula publishing, CA).

Vagle, S., Large, W. G., and Farmer, D. M. (**1990**). "An Evaluation of the WOTAN Technique of Inferring Oceanic Winds from Underwater Ambient Sound," J. Atmos. Ocean. Tech. **7**, 576-595.

Verlinden, C. M., Sarkar, J., Hodgkiss, W., Kuperman, W., and Sabra, K. (**2015**). "Passive acoustic source localization using sources of opportunity," J. Acoust. Soc. Am. **138**, EL54-EL59.

Wales, S. C., and Heitmeyer, R. M. (**2002**). "An ensemble source spectra model for merchant ship-radiated noise," J. Acous. Soc. Am. **111**, 1211-1231.

Wenz, G. M. (**1962**). "Acoustic Ambient Noise in the Ocean: Spectra and Sources," J. Acoust. Soc. Am. **34**, 1936-1956.

Westwood, E. K. (**1992**). "Broadband matched-field source localization," J. Acoust. Soc. Am. **91**, 2777-2789.

Wilmut, M. J., Chapman, N. R., Heard , G. J., and Ebbeson, R (**2007**). "Inversion of Lloyd mirror field for determining a source's track," IEEE J. Ocea. Eng**. 32**, 940-947.

Woolfe, K., Lani, S., Sabra, K. G, and Kuperman, W. A. (**2015**). "Monitoring deep ocean temeratures using acoustic ambient noise," J. Acoust. Soc. Am. **118**, 3524-3530.

Worcester, P. F., and others (**1999**). "A test of basin scale acoustic thermometry using a large aperture vertical array at 3250 km range in the eastern North Pacific Ocean," J. Acous. Soc. Am. **105**, 3185-3201.

Worzel, J. L., Pekeris, C. L., and Ewing, W. M. (**1948**). *Propagation of Sound in the Ocean: Explosion Sounds in Shallow Water* (Geological Society of America).

Yang, K., Xu, L., Yang, Q., and Duan, R. (**2018**). "Striation-based source depth estimation with a vertical line array in the deep ocean," J. Acoust. Soc. Am. **143**, EL8-EL12.

Yang, Q., Yang, K., Cao, R., and Duan, S. (**2018**). "Spatial verticl directionlity and correlation of low frewuency ambeint noise in deep ocean direct arrival zonesValidated shipping noise maps of the Northeast Atlantic," Sensors. **18**, 319.

Yang, T. C., and Yoo, K. (**1997**). "Modeling the environmental influence on the evrtical coherence of ambient noise in shallow water," J. Acous. Soc. Am. **101**, 2541-2554.

Young, R. W. (**1947**). "Image interference in the presence of refraction," J. Acoust. Soc. Am. **19**, 1-7.

Zala, C. A., and Ozard, J. M. (**1990**). "Matched-field processing in a range-dependent environment," J. Acoust. Soc. Am. **88**, 1011-1019.

Zhang, Z., and Tindle, C. (**1993**). "Complex effective depth of the ocean bottom," J. Acous. Soc. Am. **93**, 205-213.

Zhou, J.-X., Zhang, X.-Z., Rogers, P. H., Simmen, J. A., Dahl, P. H., Jin, G., and Peng, Z. (**2004**). "Reverberation vertical coherence and sea-bottom geoacoustic inversion in shallow water," IEEE J.O.E. **29**, 988-999.

APPENDIX A. Copyright Permissions

06 April 2022
Journal of the Acoustical Society of America
1305 Walt Whitman Road
Meliville, NY 11747, acousticalsociety.org

I am preparing my PhD thesis for submission to the Faculty of Graduate Studies at Dalhousie University, Halifax, Nova Scotia, Canada. I am seeking your permission to include a manuscript version of the following paper(s) as a chapter in the thesis:

> N Shajahan, DR Barclay & YT Lin "Quantifying the contribution of ship noise to the underwater sound field". *J. Acoust. Soc. Am*. 148,2020,3863-3872.
> https://asa.scitation.org/doi/10.1121/10.0002922

Canadian graduate theses are collected and stored online by the Library and Archives of Canada. I am also seeking your permission for the material described above to be stored online with the LAC. Further details about the LAC thesis program are available on the LAC website (www.bac-lac.gc.ca).

Full publication details and a copy of this permission letter will be included in the thesis.

Yours sincerely,

Najeem Shajahan
Department of Oceanography
Dalhousie University

Permission is granted for:

a) the inclusion of the material described above in your thesis.

b) for the material described above to be included in the copy of your thesis that is sent to the Library and Archives of Canada (formerly National Library of Canada) for online storage.

Name:	Joseph Castellano	Title:	Assistant Journal Manager, AIP Publishing
Signature:		Date:	04/08/2022